FERNANDA HILLE

ON THE CHALLENGES OF PREDICTING WAVE-INDUCED SLOW-DRIFT MOTIONS OF SEMI-SUBMERSIBLE PLATFORMS

São Paulo
2023

FERNANDA HILLE

ON THE CHALLENGES OF PREDICTING WAVE-INDUCED SLOW-DRIFT MOTIONS OF SEMI-SUBMERSIBLE PLATFORMS

Revised Version

Thesis submitted to the Escola Politécnica da Universidade de São Paulo for the partial fulfillment of the requirements for the degree of Doctor of Science.

Supervisor:
Prof. Alexandre Nicolaos Simos

Co-supervisor:
André Luís Condino Fujarra

São Paulo
2023

Este exemplar foi revisado e corrigido em relação à versão original, sob responsabilidade única do autor e com a anuência de seu orientador.

São Paulo, _______de_______________________de_________

Assinatura do autor: ____________________________________

Assinatura do orientador: ________________________________

Ficha Catalográfica

HILLE, FERNANDA

On the challenges of predicting wave-induced slow-drift motions of semi-submersible platforms. São Paulo, 2023. 142 p.

Tese (Doutorado) — Escola Politécnica da Universidade de São Paulo. Departamento de Engenharia Naval e Oceânica.

1. Forças de deriva média 2. Movimento de deriva lenta 3. Semi-submersível 4. Boundary Element Method I.Universidade de São Paulo. Escola Politécnica. Departamento de Engenharia Naval e Oceânica II. t.

This thesis is dedicated to my mom who always
gave me support, love and high hopes for a living.
Dolores Hille
(1960 - 2021)

Acknowledgements

Possibly, this is going to be one of the longest acknowledgements sections ever seen in a thesis, but I am more than thankful for everyone who supported me on this journey and also for those who were with me in the hardest time of my life.

I will start by thanking the most important person in my life, who is not physically here anymore, but I am sure and I can feel that is taking care of me: my mom, Dolores Hille. My mom was an example for me since I was born by taking care of me, of my grandmother who was sick for many years, of the house tiding, cooking, etc, all by herself and still she had to work to sustain us. The money was not enough, but she NEVER gave up on anything, including my education. While some family members tried to induce her to make me work to help her to pay the bills, instead of going to college, she always supported me to study. And it worked well! Thanks to her I was able to study a lot and get scholarships at all periods, in this way, I could help her with the expenses. When I was accepted at the PhD program at USP, she was the most proud person I have ever seen, and now Mom, I hope you are seeing this! Love you for eternity! Dear God, thank you for taking care of her and thank you for giving me strength in everything.

Regarding the academic field, I could not ask for a supervisor who could fit better to my personality and my way of working than Alexandre Nicolaos Simos. He knows exactly when he should be demanding and sharp, but he also knows when he needs to say a smart, funny thing or do anything else to support me and make me feel well. He is one of the most intelligent people I know, and kept up with our work during the whole time of these five years. It was great to work with you professor, I am so thankful for everything that you helped me in all these years.

Also, I would like to thank the person who supported me to start all of this, my co-supervisor: André Luís Condino Fujarra. Professor Fujarra was one of the greatest professors I have ever had, and he is one of the people responsible for raising my passion in hydrodynamics. Thank you professor for believing in my potential more than myself, and with his help the dream of becoming a doctor is coming true.

How could I achieve this without the support of my boyfriend, Henrique Dela Giustina, and his family, Albertina Salvador Marcelo and Franquelino Dela Giustina? You have supported me in so many ways I cannot describe since the beginning, even knowing I would have to move to São Paulo. I am so glad to have you all in my life.

I would also like to thank to the members of my thesis committee, Prof. Dr. Ruben Alvarado, Dr. Marcos Donato, Prof. Dr. Cláudio Rodriguez and Prof. Dr. Celso Pesce for their great and significant corrections and suggestions to improve this work. I really appreciate your time and contribution on this. A special thanks to Prof. Dr. Celso Pesce for being a valuable and inspiring professor and human being. I am glad I took four courses with you (I think this is a record), so I had a lot of time for learning from you.

Another very special thanks to my academic brothers, Lucas Henrique Souza do Carmo and Lariuss Zago who became great friends of mine and have shared their huge expertise with me every time I need. I am always proud of you and I am so happy to have shared these years with you. I also would like to thank my TPN friends, Yu Kang Kam, Cristiana Pirpiris, Jordi Soler, Raiza da Silva, Guilherme Vernizzi and Giovanni Amaral for all the good moments, bandejões, coffees and laughs.

I have no words to express how grateful I am for having Pedro Mello and Edgar Malta for helping me confabulate about all the hydrodynamics phenomena that could be happening on the platform. Pedro was also responsible along with Izabela Frazão and Yu kang Kam for helping on the experiments of this thesis. I cannot thank you all enough for that. Ah, also, a special thanks to Pedro who had to dive in the tank in very cold water! Also, I would like to thanks João Sparano for his great contribution on the WAMIT set up.

Thanks to Petrobras SA for providing data on the semi-submersible platform. Without them, the conclusion of this thesis would not be possible. An additional thanks for this company having financed the Dynasim R&D project that sponsored my scholarship in the first two years.

Also a huge thanks to ESSS, Rodrigo Peralta and Gabriel Faria for all the support in Fluent and AQWA. With their help, the simulations and analysis were more robust.

I could not miss the chance to thank the best University of Latin America, the University of São Paulo (USP), which is full of great professors, students and staff. USP gave me a new perspective not only of the academic world, but also of life. It is a dream to be part of this community.

I am also so lucky to have such good flatmates as Mayra Costa and Terezinha Ayres. You are both great friends who I will take with me for eternity. In addition, thanks to all the friends who I made in São Paulo Amanda Oliveira, André Luís Zanella, Letícia Madi, Izabella Nunes and Monalisa Franscisco, and all from the Hera and Zeus teams (Olympus Cheerleading).

I cannot forget of my family, my aunts Dorita Hoering and Leda Lopes, my uncles Renato Hoering and Waldir Hille, my cousins Alessandra Hoering, Fabiana Hoering, Valcemar Justino da Silva, Daniela Hille and Douglas Hille who are always proud of me and have not measured any efforts when me and my mom most needed to.

A big thanks to NAVSHIP - EDISON CHOUEST OFFSHORE which also always has supported me pursuing my PhD degree. I would like to thank Mr. Gary Rook, Jacob Cheramie, Richard Allinson, Murray Hughes and the Chouest Family for all the support and for every work we have already done together. I wish that all our projects become true. I am so lucky to have such great people around me every day like Marlon Batistella, Yuki Girardi, Christian Cardoso, Ronan Michels, Atilio Scussel, Jéssica Schneider, Hugo Vidal, Janaína Celestino, Gabriel Barros, Diego Francisco, Barbara Cardoso, Kamylla Santos, Francisca Leite, José Augusto Silva, Bruno Haluszczak, Pedro César, Felipe Teixeira, Luís Galdino and all the engineering team. A special thanks to David Munaretto who is one of the people responsible for me being in this company. Thank you for believing in me.

A special thanks to the good people who took a little of their time to help me with my thesis: Flávia Witt, Henrique Dela Giustina, Lariuss Zago, Atílio Scussel and Lucas do Carmo.

Talking about friends, things are never so scary when you have good friends as mine. Even in the middle of the pandemic these friends were with me in presence when I most needed to, so I would like to thank them: Júlia Vilela de Abreu,Yuki Girardi, Marlon Batistella, Hugo Vidal, Juliana Elias, Virginia Santos, Lucas Rodrigues, Patrícia Franco, Ana Paula Storto, João Paulo Nicolodi, Débora Motta, Rhavi Gonçalves, Andressa Gottardo, Flávia Witt, Jan Oliveira, Nayana Eccel, Nicole Eccel, Patrícia Eccel, Jean Haerbele, Felipe Tontini,

Amanda Anton, Lucas Silvano, André Herbst, Alessandra Franco, Isabelly Perin, Lewton Litwinski and Gabriel Oliveira, André Luís Zanella, Cristina Butzke. My family presence was fundamental as well, Daniela Andrade, Laura Andrade, Giane Andrade, João Batista de Andrade, João Carlos de Andrade, Viviane Andrade, Simone Andrade, Mauricio Klober, Maria Beatriz besides the ones mentioned previously. Some people were not able to join presently but they figured out a way to make me feel their feelings: Elisa Mobini, Manuela Sabatke, Ruan de Paula, Emmanuel Schlickmann, Thais Consiglio, Mariana Boneli, Juliana Midori, Terezinha Ayres, Tales Souza and Christian Cardoso, besides all the ones mentioned before.

All of you mentioned here are special to me and have contributed not only to this journey, but to my life as well. I sincerely thank you all from the bottom of my heart.

Abstract

Semi-submersible type platforms are important not only for oil and gas offshore exploration, but also for the floating offshore wind turbines field. In both type of operations, the platforms are moored at the bottom of the ocean and, at the moment that external stiffness is added to the system, the second-order wave forces become worrisome. Part of these forces act at low-frequencies and are responsible for inducing slow-drift motions in surge, sway and yaw.

Softwares based on the potential theory are important allies to the low-frequency forces and slow-drift motions calculation. However, their results may be less accurate for semi-submersible vessels, as it is stated in the literature. In general, the works in this field deal with seas that may be too high and steep for the Boundary Element Method (BEM) codes, but the present thesis, on the other hand, focuses on common seas within the operational limitations of the software.

In the last two decades, researchers noticed that the wave fields of a certain four-column large displacement platform were not well captured by the radiation/diffraction programs in some circumstances, but later works could not go further on this problem. Aiming at verifying the mean and slow-drift motions computed by the potential codes, free-floating and captive tests under regular and bichromatic waves with the scaled-model of one of such platforms were executed at the Numerical Offshore Tank of USP (TPN-USP).

Results showed that BEM code considerably underestimated the slow-drift motions for a certain range of periods in regular and bichromatic waves, while for the other periods, the results were considered satisfactory. With a detailed investigation and with the aid of the Computational Fluid Dynamics (CFD) tool based on Finite Volume Method (FVM), it was possible to conclude that the underestimation of these forces are originated mainly from divergences in the prediction of the free-surface elevations diffracted by the columns under conditions that might involve near-trapping of waves.

Finally, with the purpose of evaluating how much these errors may interfere in the prediction of slow-drift motions in more realistic conditions, irregular waves were tested with the platform anchored by four catenary lines. For these cases, a variety of seas were replicated into the BEM code and at this time, the program managed to capture all the amplitudes of the slow-motions very well. This is an indication that the discrepancies only appear in cases with regular and bichromatic waves because they allow the system to reach steady-state at an isolated frequency. Therefore, at least for the semi-submersible geometry studied in this work, the effects of the errors that were evident under regular waves and wave groups, were eventually mitigated in more realistic conditions.

Keywords: Mean drift forces. Slow-drift motions. Semi-submersible. Boundary Element Method.

Resumo

Plataformas do tipo semi-submersível são recursos fundamentais não só para a exploração de óleo e gás offshore, mas também para o campo de turbinas eólicas flutuantes. Nos dois tipos de operação, as plataformas são ancoradas no fundo mar e é nesse momento, em que uma rigidez externa é adicionada ao sistema, que as forças das ondas de segunda ordem se tornam preocupantes. Parte dessas forças atuam em baixas frequências e são as responsáveis por induzir os movimentos de deriva lenta das plataformas em surge, sway e yaw.

Programas baseados na teoria do potencial, são grandes aliados no cálculo das forças de baixa frequência e de deriva lenta de plataformas. Todavia, os resultados fornecidos por eles, talvez sejam menos precisos para plataformas semi-submersíveis, como é citado na literatura. Em geral, os trabalhos nesta área abrangem mares severos com declividade muito alta para os softwares de Boundary Element Method (BEM), a presente tese, no entanto, foca em mares mais comuns e dentro dos limites operacionais desse tipo de programa.

Nas duas últimas décadas, pesquisadores notaram que o campo de elevações de onda de uma certa plataforma de 4 colunas e grande deslocamento não era bem capturado pelos programas de radiação/difração em algumas circunstâncias, no entanto, trabalhos posteriores não conseguiram se aprofundar no problema. Com o intuito de avaliar as forças e movimentos de deriva média e lenta providos pelos códigos potenciais, ensaios livres e cativos sob ondas regulares e bicromáticas com o modelo dessa plataforma foram realizados no Tanque de Provas Numérico da USP (TPN-USP).

Os resultados mostraram que os programas subestimaram consideravelmente os movimentos de deriva lenta para uma específica faixa de períodos para ondas regulares e bicromáticas. Já para os demais períodos, os resultados foram considerados satisfatórios. Com uma detalhada investigação e com o auxílio da ferramenta de Dinâmica dos Fluidos Computacional (CFD) basedo no método de volumes finitos (FVM), foi possível concluir que a subestimação dessas forças são originadas principalmente das discrepâncias na estimativa das elevações da superfície-livre difratadas pelas colunas sob condições que possam envolver ondas near-trapping.

Com o propósito de avaliar o quanto esses erros apresentados pelos códigos potenciais podem interferir na predição de movimentos de deriva lenta em casos mais realistas, ondas irregulares foram ensaiadas com a plataforma ancorada por catenárias. Para esses casos, uma variedade de mares foi replicada em código BEM e o programa conseguiu capturar bem as amplitudes dos movimentos de deriva lenta. Isso é uma indicativo que as discrepâncias aparecem de forma mais pronunciada em casos com ondas bicromáticas pois essas permitem o sistema atingir o regime estacionário em uma frequência isolada. Assim, pelo menos para a geometria da plataforma semi-submersível estudada, os efeitos dos erros que eram evidentes em ondas regulares e grupo de ondas, foram eventualmente mitigados em condições mais realistas.

Palavras-chave: Forças de deriva média. Movimento de deriva lenta. Semi-submersível. Boundary Element Method.

List of Figures

List of Tables

Contents

List of Acronyms

BEM	Boundary Element Method
CFD	Computer Fluid Dynamics
FOWT	Floating Offshore Wind Turbine
FVM	Finite Element Method
LCG	Longitudinal Center of Gravity
PSD	Power Spectral Density
QTF	Quadratic Transfer Function
RANS	Reynolds-Averaged Navier-Stokes
RAO	Response Amplitude Operator
TCG	Transverse Center of Gravity
TPN-USP	Numerical Offshore Tank of University of São Paulo
VCG	Vertical Center of Gravity
VOF	Volume of Fluid

List of Symbols

A	Wave amplitude
A_{11}	Added mass in surge
Am	Mean amplitude
As	Significant wave amplitude
B_{ext}	External damping
C_D	Drag coefficient
C_M	Inertia coefficient
ε	Steepness
EA	Axial elongation
F	Force
g	Gravity acceleration
H	Wave height
Hs	Significant wave height
k	Wave number
K	Stiffness
KC	Keulegan-Carpenter Number
λ	Wave length
M	Momentum
M_{11}	Mass in surge
P	Pressure
ϕ	Velocity potential
ϕ_w	Potential of the undisturbed incoming wave
ϕ_s	Scattering wave potential
ϕ_r	Radiation potential
ρ	Water density
t	Time
T	Wave period
Tn	Natural period
Tp	Wave peak period
ω	Wave frequency
x	Longitudinal coordinate

y	Transverse coordinate
z	Vertical coordinate
ζ	Free surface elevation
ζ_1	Damping coefficient

1 Introduction

Oil can be considered one of the most important natural resources on earth and it was the greatest responsible for initiating the development of the offshore industry worldwide. While countries had been extracting oil only onshore, the drilling process was quite simple. However, due to the fact that oil basins near to shore had been discovered, the drilling operations started to take place in the sea. Over the years, more oil reservoirs have been found farther away from the coast and, consequently, at greater depths.

The necessity of fixed structures under the platform was replaced by mooring systems, thus the vessel was able to operate at large depths. Figure 1.1 represents some of the types of oil extraction systems and their operational depth limits. At that point, fixed structures have become not practical and drilling barges were not stable enough to carry out deep water operations.

Figure 1.1: Onshore to offshore oil exploration systems.

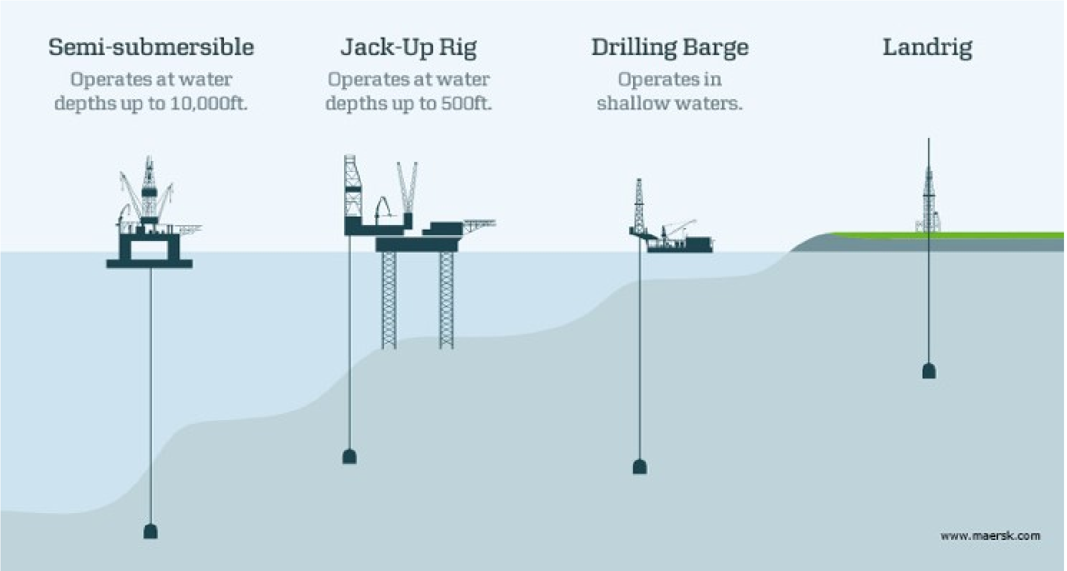

Extracted from (DEEP TREKKER, 2020).

Currently, floating offshore wind turbines have been following the same idea in order to generate more power by placing these systems in the sea. A variety of moored semi-submersible type platforms with an assortment of column numbers and arrangements are now being fundamental not only for the oil and gas industry, but also for the renewable energy field. Figure 1.2 exemplifies some floating offshore wind turbines geometries and presents how their configurations may vary. This renewable field is still considerably recent, but at the same time, huge efforts on research and development of offshore wind farms are being made by a large number of companies and universities all over the world. Hence, it is critical that the radiation/diffraction codes, which are the main tool for the designing stages of platforms, have their limitations well comprehended and results well validated.

Figure 1.2: Examples of floating offshore wind turbines geometries.

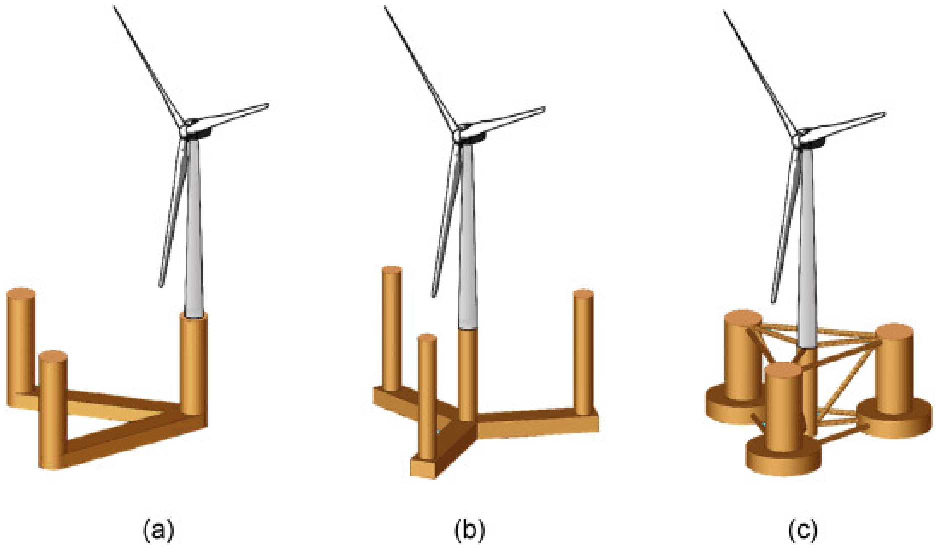

Extracted from (ZHANG et al., 2020)

Semi-submersible type platforms have actually been conceived in order to reduce the motions of the floating unit in waves, since their shape provides a better seakeeping than common ship-shaped hulls (LEFFLER; PATTAROZZI; STERLING, 2011). The main objective of its geometry is being more transparent to wave action. A feature that allows this type of system to work in severe environments is that the deck is significantly higher than the waves' crests. Nevertheless, this does not mean that a good prediction of the forces and motions induced by the waves are not important for the system design.

Waves are actually critical components impairing the offshore operations, for exciting the system dynamics. Following the classical approach proposed by Stokes (1847), the wave forces can be understood as the sum of components with different orders of magnitude with respect to the wave amplitude. The higher the order, the smaller its magnitude. Thus, the first-order wave forces are the largest and the easiest to comprehend. They are important mainly for the vertical degrees of freedom: heave, roll and pitch.

Although smaller, the low-frequency second-order wave forces are able to excite resonant motions of the moored platform in some degrees of freedom, usually surge, sway and yaw, and when this happens, the response amplitudes may be very large due to the small damping factor of these motions. In this case, the response is composed by slow-drift and mean-drift motions which are responsible for making the vessel drift slowly side to side around a displaced mean position.

Besides designing the platform itself, engineers are then challenged to design its respective mooring system, which is an interactive process that depends on the motions of the vessel. For that, software based on the diffraction/radiation theory have become a fundamental tools for platforms and mooring systems design. Among some of the commercial panel method codes available nowadays, WAMIT (LEE, 1995) and AQWA (ANSYS, 2013) are two of the most popular.

Regarding first-order loads; the potential theory is already well consolidated and uncountable model-scaled tests performed widely in the world are a proof of it. In relation to second-order wave forces and the motions related to them, these codes cannot be considered as solid yet. Indeed, underpredicting surge, sway and yaw motions is a matter of concern for many reasons: to miscalculate the mooring system, to cause errors in the risers and mooring lines fatigue predictions calculations and to disturb and compromise oil extraction operations are some examples.

Many authors as Berthelsen et al. (2009), Lopez-Pavon et al. (2015), Wang et al. (2021) and Wang et al. (2022) noted some discrepant results of the potential codes in relation to model tests even for mean drift forces and/or mean offsets. In general, the authors simulated high and steep sea states and assumed the lack of viscous in the Boundary Elements Based (BEM) codes as the main reason for underestimating such forces and motions. Nevertheless, what if deviations between potential codes and experimental results appear in mild sea states as well?

For sure, the slow-drift motions depend on important input parameters which are difficult to obtain and could compromise the predictions, such as the viscous damping. Into frequency-domain software, the users are allowed to input an external damping matrix which refers to the viscous damping in a linearized form. The viscous damping is actually quadratic in nature, thus composed by a linear and a quadratic term which can be estimated from decay tests, for example. Furthermore, in the resonant drift oscillations a wave-drift damping is also involved, which many times is not easy to compute. In fact, previous experimental and numerical works have suggested that sometimes the wave-drift damping coefficients in semi-submersibles result negative, such as Nossen, Grue and Palm (1991). However, the damping may not be the only possible source of error.

A four-column large displacement semi-submersible type platform that operates in Brazil, and which was already model tested a couple of times, has shown some evidence on the difficulty of modelling its wave elevation field even for common sea states. Matos (2009) has noticed this while evaluating the run-up and air-gap phenomena in vertical slow-motions for this platform. Previous model-scale tests of this unit have raised the suspicion that trapped waves could be occurring in certain sea conditions. A variety of other experiments were performed with this semi-submersible trying to capture this phenomenon, but, unfortunately, with no success. The semi-submersible in question, presented in Fig. 1.3, has a beam and length of 85 m, a draft of 27.5 m, besides pontoons that are 12m high and 17.5m wide, achieving almost 80,000 ton of displacement.

Figure 1.3: Small-scale model of the four-column large displacement semi-submersible platform used as object of study in the present thesis.

Having this semi-submersible as an object of study, the present thesis aims to describe challenges and doubts on estimating the mean and slow-drift forces and motions through BEM codes, trying to break down the effects into their main components and thus isolate and identify the main sources of discrepancies observed with the model tests records, which should be well predicted by radiation/diffraction codes. Any significant deviation between the results computed by the potential code and the experiment was evaluated. In order to better substantiate the issue, regular and bichromatic waves were adopted as the principal means for the analysis, in addition to irregular sea states to quantify the problem in real seas.

For that, three experimental tests especially designed for the task were devised. As the second-order forces have a small magnitude, these model tests needed to be carefully thought and designed in order to capture all the required data with sufficient accuracy. The tests were performed at head waves, so the forces and motions are focused on surge. The tests had to be planned to achieve a surge natural period sufficiently long enough to intensify the second order wave effects, but not that too large to get enough cycles.

A 1:100 model-scaled of the mentioned semi-submersible was chosen and the experiments were conducted in the wave basin of the Numerical Offshore Tank of USP (TPN-USP) in which many adversities had to be overcome to perform such sensitive tests. The first model test had the platform fixed to the bridge in order to measure directly the mean and low-frequency forces on the model caused by the effects of regular and bichromatic waves. The second experiment was performed with the model free to float, restricted only by a horizontal mooring system, under the same regular and bichromatic waves. Finally, the third and last model test attempted to provide a more realistic configuration with irregular waves and with four catenary lines. These lines do not represent a real mooring system, but they provide a more reasonable shape in relation to the reality, besides contributing to investigate if there is any doubt in the numerical modeling of the mooring systems.

All the runs of these three experiments were replicated in a potential code with the same waves and set-ups. Thus, a detailed evaluation of the forces and motions provided by the code could be prepared and an accurate investigation of possible sources of errors could be made.

In the pursuit of the origin of the differences between BEM based codes and model tests, CFD based on Reynolds-Averaged Navier-Stokes (RANS) simulations in FVM were also used as a complementary tool as well. For conciseness, the potential code will be referred to as diffraction/radiation code or BEM or potential code itself; and the CFD - RANS simulations will be defined as FVM from now on. In this latter, the forces components, including the viscous forces, can be extracted from the results. Another advantage is that they allow for a visualization of the predicted flow and free-surface motions. Furthermore, the wave elevations may be captured at any region on the domain.

1.1 Objectives

The main objective of the thesis is to evaluate the performance of potential codes in predicting mean and slow-drift forces and motions of a large displacement semi-submersible platform in waves of small steepness and amplitudes within software limitations, having a fundamental and systematic approach and identifying how possible discrepancies may affect its responses in real sea states. For that, different techniques are used to encircle the problem in the best way possible. In order to achieve that, the principal goal may be divided into three targets.

1. To evaluate direct measures of the forces acting on the fixed platform due to waves, since free floating tests are not capable of providing these direct measurements. In this analysis, the regular and bichromatic waves are executed due to their ability to easily achieve the stationary regime and isolate the frequency of interest. For meeting this goal, the following activities were performed:
   - (a) To design and perform regular and bichromatic wave tests with the captive model to obtain, respectively, the direct mean and difference/frequency forces acting on it. The wave elevations in some points between the columns are also captured.
   - (b) To use a radiation/diffraction software to compute the mean and difference-frequency forces having the same set-up as those from the experiments. To measure the free-surface elevations close to the four columns of the platform.
   - (c) To simulate and calculate the forces and wave elevation of the fixed platform in regular waves using CFD under the same experiment configurations as well.
   - (d) To compare experimental and numerical results at each wave period from 7 to 11 seconds, which are in the common range of the sea and represent a good variation of the behavior of the platform according to its geometry; and finally, raise the possible sources of errors.
2. To appraise the direct mean and slow-drift motions of the free floating semi-submersible under the same bichromatic waves. The following tasks are developed in order to achieve the objective.
   - (a) To perform free floating wave model tests with the semi-submersible in bichromatic waves.
   - (b) To compute mean and slow-drift motions using a potential code. In order to mitigate possible errors caused by the viscous damping prediction, a range of damping computed from the decay tests are used for each wave period. In addition, the other method to account with the viscous damping in the potential code was using the Morison's elements feature into the potential code.
   - (c) To compare experimental and numerical results at each period executed.
   - (d) To correlate possible results in common between mean and slow-drift forces and their respective motions.

3. To calculate the direct mean and slow-drift motions of the platform under irregular waves to represent a more realistic condition and evaluate if possible errors presented under stationary waves may also appear in real sea states. In pursuit of accomplishing this target, the specified duties are described below.
    (a) To perform free floating wave tests with the scaled-model platform under irregular waves.
    (b) To compute mean and slow-drift motions using a potential code by having the same methodology to select the viscous damping values as stated in the bichromatic waves section.
    (c) To compare experimental and numerical results at each period of interest.
    (d) To associate the final results with those from the bichromatic waves tests.

1.2 Methodology

In order to achieve the main objectives presented in the previous section, each minor objective must be fulfilled. Therefore, this section provides an overview of the procedures adopted to accomplish them. Detailed information about the experiments and numerical development will be presented in Chapter 4.

1.2.1 To evaluate direct measures of the forces acting on the captive platform due to waves

In pursuance of direct measuring surge mean and difference-frequency waves forces, excluding components related to the platform motion and damping, captive tests were executed at TPN. The model needed to be well attached to the bridge at the design draught. At this point, the system fixed to the bridge should be stiff enough in order to the smaller natural frequency be still way higher than those from the wave frequencies executed during the tests. A load cell was placed on the deck for measuring the loads at this point. Regular and bichromatic waves with various periods and with difference-frequencies close to the natural period of surge were carried out.

In order to guarantee the accuracy of the potential codes, only small steepness waves were generated, but it was also necessary to create waves that induce forces that are large enough to ensure that the measurements are reliable. Even with a high quality load cell, it is complex to measure such small forces acting on the model since any noise can affect the test results.

In addition to three wave probes placed far enough from the platform waves interactions, four wave probes were positioned near to the inboard center of the columns having the goal of measuring the wave elevations between the columns of semi-submersible. The wave probes were not attached to the platform to avoid capture run-up cases.

The same configuration of set-up and waves were developed into the BEM code AQWA and the FVM Fluent both from ANSYS. Into both software, the wave forces and wave elevation in each column of the platform could be computed. Having in hand the results of the experimental tests and numerical models, the contribution of the different second-order force components can be compared and the source of eventual errors can be sought.

1.2.2 To appraise the direct mean and slow-drift motions of the free floating semi-submersible

Free-floating model-scaled tests must be performed in order to analyse the mean and slow-drift motions predictions through potential codes and also correlate them to their forces. Lines and springs were chosen for reproducing the horizontal stiffness of the mooring system and in order to focus on the second-order related motions, bichromatic waves were selected since they are the representation of the regular wave groups which allow to measure directly the effects of each frequency pairs from the QTF.

The semi-submersible model was ballasted to have the same displacement, center of gravity, radii of gyrations as the real platform. Further, pre-test such as inclination, pull-out and decay tests were performed before the runs to check the system particulars. A camera system with reflexive targets was used during the tests to acquire the model motions in all of the 6 degrees of freedom.

Into the BEM software AQWA, time-domain simulations of the model subjected to the same bichromatic waves were executed. The external damping in surge was computed by two different approaches, decay tests and Morison's elements are used in an attempt to reduce the uncertainties related to the viscous flow effects. For the first one, each case was run with three different damping values: the damping percentage of the critical values obtained direct from the decay tests and a ±30% in relation to this value. Therefore, with all those results in addition to the ones provided by the second order forces analysis, relations between the level of agreement obtained in both analyses can be sought.

The FVM software was not used in this evaluation due to the complexity of modelling the entire system free to move into the domain. Another big obstacle, of course, is that this type of simulation is very computationally expensive since to get such small forces, the mesh needs to be highly refined.

1.2.3 To calculate the direct mean and slow-drift motions of the platform under irregular waves

For this task, the model was free floating with a catenary mooring system under irregular waves in an attempt of providing a more realistic environment to the experiments. The idea here was not representing a real mooring system, but offers a more similar set-up to real line shapes. The peak periods were selected in accordance to those from the two previous experiments.

The same pre-tests and motions acquisition system were used here, but now the hardest part is to define catenary mooring lines with a similar horizontal stiffness from the previous test. For that, the Petrobras dynamic simulator, DYNASIM (NISHIMOTO; FUCATU; MASETTI, 2002) was used as a tool. In this software, the platform was represented with four catenary lines divided into two segments, one significantly heavy and one with minimal linear weight. In this way, a catenary shape with the required particulars and with a long enough touch-down zone to allow the semi-submersible motions was defined.

One more time, this experiment was replicated only into AQWA and the mean and slow-drift motions were again evaluated in relation to the model tests. Hence, the impact of the possible deviations between potential codes predictions of motions and the ones presented by the platform in real life could be appraised.

1.3 Text Outline

Besides the present chapter, the thesis has been organized into other six sections:

- Chapter 2 contains a literature review focused on presenting an overview of works related to second order wave forces acting on cylinders or semi-submersible platforms, in addition to comparisons to numerical models which were essential to the development of the thesis.
- Chapter 3 is dedicated to the theoretical background required to understand the non-linear wave forces and their hypothesis, as well as evaluating the forces components acting on a single bottom-mounted cylinder.
- Chapter 4 describes the numerical modelling of both BEM and FVM programs, in addition to experimental tests set-up performed with the semi-submersible platform.
- Chapter 5 is devoted to presenting the results and explaining the challenges and sources of divergences on the numerical estimation of second order forces and mean and slow-drift motions.

- Lastly, Chapter 6 summarizes the main conclusions and presents proposals of future work.

2 Literature Review

Matos (2009) has observed a difficulty in representing the wave elevation field of a large displacement semi-submersible platform during the development of his thesis. Matsumoto et al. (2013) have also put this platform under investigation for evaluating the wave run-up and air gap predictions by both BEM and FVM codes. Even though their focus was on the vertical motions, their main findings are also related to the difficulty of modelling the wave elevation field of this platform. Seven waves probes were placed in different locations below the deck in the experiments, Fig. 2.1, and the same were modelled into WAMIT 1^{st} and 2^{nd} order, besides the volume of fluid code ComFLOW (RUG, 2023).

Figure 2.1: Location of the wave probes (values in mm).

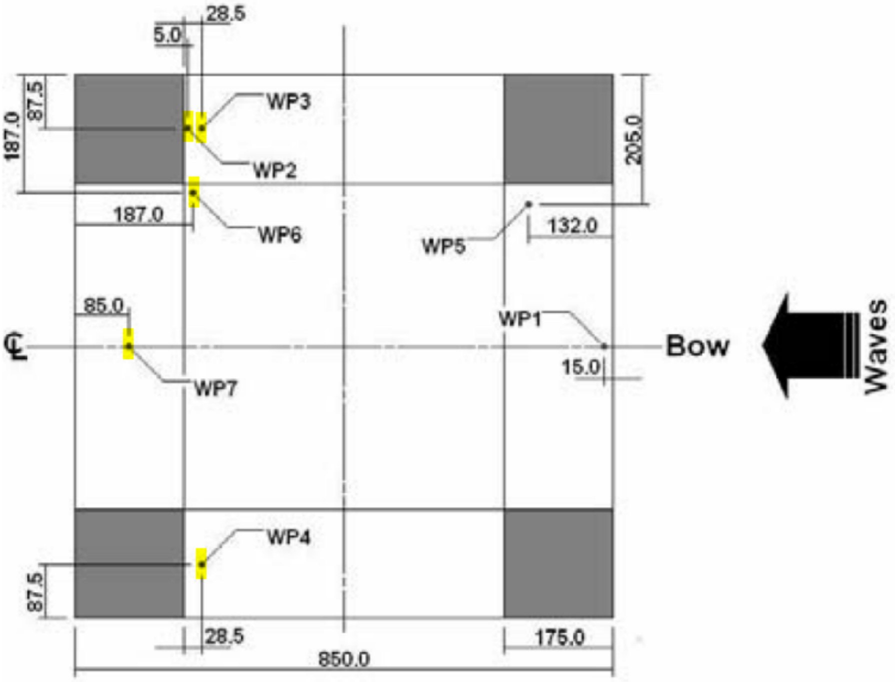

Extracted from (MATSUMOTO et al., 2013).

As Fig. 2.2 presents, the runs were performed in extreme waves with periods from 11.9 s to 21.5s in full scale. The first three waves have a relatively small steepness, however, the shorter ones are significantly steep.

Figure 2.2: Waves tested parameters (full scale).

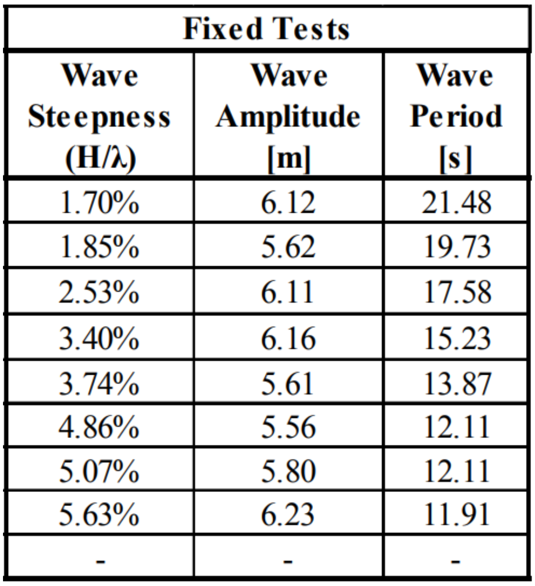

Fixed Tests		
Wave Steepness (H/λ)	Wave Amplitude [m]	Wave Period [s]
1.70%	6.12	21.48
1.85%	5.62	19.73
2.53%	6.11	17.58
3.40%	6.16	15.23
3.74%	5.61	13.87
4.86%	5.56	12.11
5.07%	5.80	12.11
5.63%	6.23	11.91
-	-	-

.

Adapted from (MATSUMOTO et al., 2013).

For illustrating their conclusions, Fig. 2.3 shows that the first order model missed a part of the wave amplitude for large steepness, which is partly recovered by the inclusion of the second order wave elevations, nevertheless, ComFLOW is able to well capture the experiments.

Figure 2.3: Non-dimensional wave elevation at a point near to the center of the aft port side column WP2.

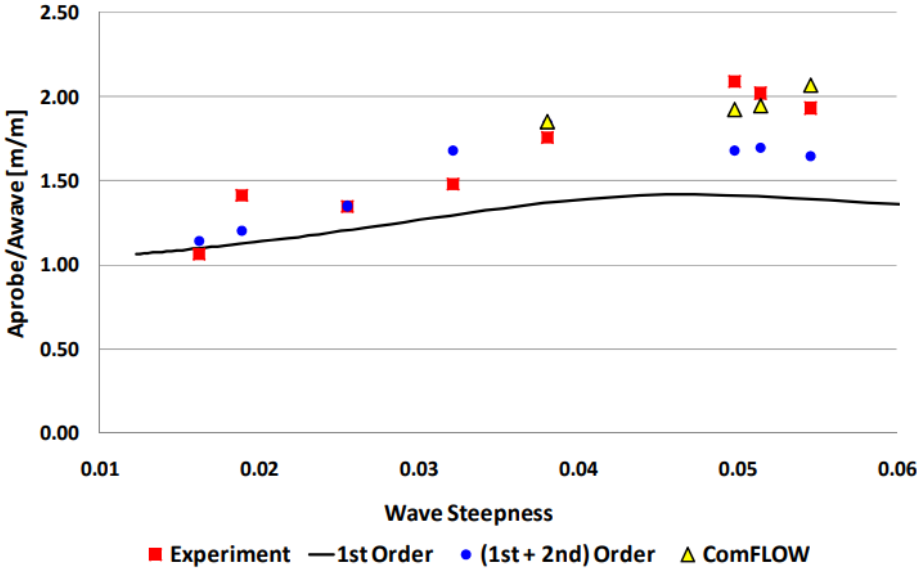

Extracted from (MATSUMOTO et al., 2013).

Although Matsumoto et al. (2013) study was performed only for extreme waves, which involve higher KC numbers and thus may be out of the range of potential codes, especially those restricted to the first-order problem, it provides an insight about how FVM codes may provide accurate predictions of waves and loads in this context. In addition, the second case (1.85% wave steepness) in Fig. 2.3, which should be well captured by the potential codes, also indicates a wave elevation underestimated by almost 20% by the potential code. The curious fact here is that both the cases with slightly higher and lower steepness are well recovered by the potential code.

Actually, other researchers had been suspicious of near-trapping or trapped waves phenomena happening in this hull. A set of experiments were performed in order to capture this phenomenon, but nothing was published since the results were not promising. On the other hand, some authors addressed in Section 2.1, such as Berthelsen et al. (2009), Wang et al. (2022) and Lopez-Pavon et al. (2015), have also described difficulties in estimating low-frequency forces and slow-drift motions of this type of platform.

2.1 Evaluation of the potential flow radiation/diffraction predictions

Different research centers and authors have been studying and analyzing the ability of BEM codes to estimate the second-order wave forces and mean and slow-drift motions in a variety of sea states and they also discuss whether the engineers can rely on these models.

Berthelsen et al. (2009) have compared the potential theory code WAMIT, along with Newman's approximation (NEWMAN, 1974), with experimental tests of a four-column semi-submersible platform in high waves. The full QTF matrix was not computed, since for using the Newman's method, only the mean drift coefficients are required. The tests were performed at MARINTEK with a 1:50 model and a horizontal mooring arrangement of 150 kN/m, resulting in a natural surge period of 146 s. Table 2.1 presents the main dimensions of the platform.

Table 2.1: Main dimensions of the semi-submersible. Adapted from (BERTHELSEN et al., 2009).

Item	Value	Unity
Length	84.48	m
Pontoons Height	8.40	m
Pontoons Width	16.64	m
Column Length	16.64	m
Column Width	16.64	m
Draft	21.00	m
Displacement	52660	ton

The authors have focused their study in surge motions in head waves in a variety of wave heights, peak periods and current velocities, however, the principal results for that thesis are related to the sea states shown in Tab. 2.2.

Table 2.2: Irregular waves tested. Adapted from (BERTHELSEN et al., 2009).

ID	Hs (m)	Tp (s)
6010	6.00	12.00
6020	12.00	12.00
6030	7.50	15.00
6040	15.00	15.00

The BEM code largely underestimated in a large scale both surge mean offset and standard deviation in the four tests. The authors have attributed these divergences to the viscous forces in the splash zone that are not taken into account in the potential code. Therefore, they have included the drag term in Morison's equation integrated up to the free surface as a slender body approximation. The drag coefficient, C_D, was calibrated by the decay tests results along to higher C_D values in the upper region of columns in the wave zone.

Figures 2.4 and 2.5 presented the main results of the paper for the cases without current. It is possible to notice a large difference between the experimental and the numerical results without the viscous component correction. Surge mean and standard deviation were represented when the viscous effects were taken into account.

Figure 2.4: Surge mean offset.

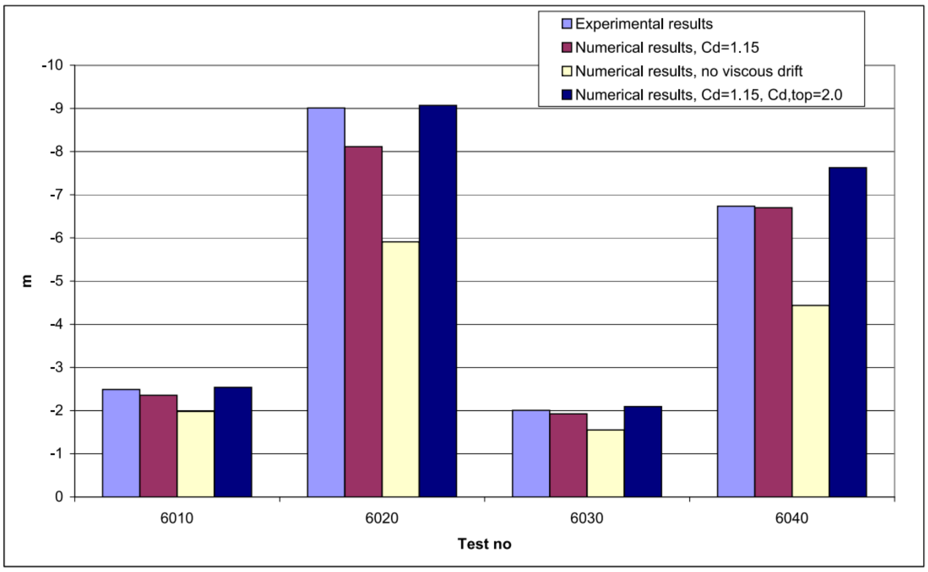

Extracted from (BERTHELSEN et al., 2009).

Figure 2.5: Surge standard deviation.

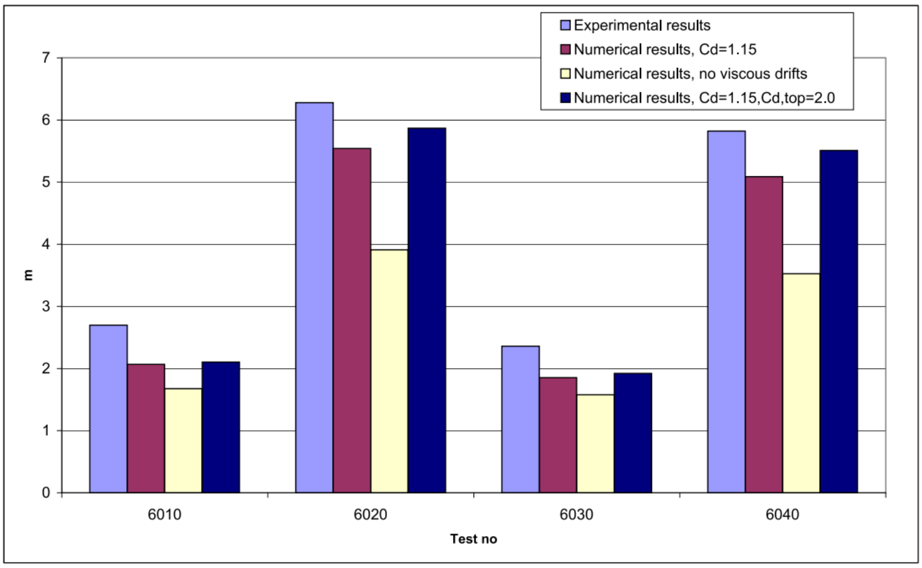

Extracted from (BERTHELSEN et al., 2009).

Nevertheless, not only for high waves but also for mild conditions of the sea, a large difference between potential code and experimental results are found. It is the case of a Floating Offshore Wind Turbine (FOWT) platform evaluated by Lopez-Pavon et al. (2015).

The authors have evaluated Newman's approximation (NEWMAN, 1974) in semi-submersible platforms by performing captive model-scaled tests with a semi-submersible FOWT platform, Fig. 2.6, with bichromatic waves at the difference-frequency in surge motion. The authors compared experimental tests with numerical models computed using WAMIT.

Figure 2.6: FOWT geometry.

Extracted from (LOPEZ-PAVON et al., 2015).

Figure 2.7 presents the results for surge motion at a difference-frequency of 0.15 rad/s or 41.9s. The tests (F2(-)/(A1.A2); numerical results from QTFs (FIX WAM) and Newman's approximation (NEW WAM) were compared. The first point to notice is that the WAMIT results had showed deviations when compared to the experiments at the lower wave periods. Also, Newman (1974) approximation has underestimated even more the second-order forces at the same region, but this was indeed expected because the surge natural period (around 70s) was not high enough for the use of this approximation. Besides, they have concluded that the captive tests had intensified the diffraction effects even more and, further, they determined that the numerical model underestimates the force at large diffraction region.

Figure 2.7: Second-order forces comparisons between WAMIT and experimental tests.

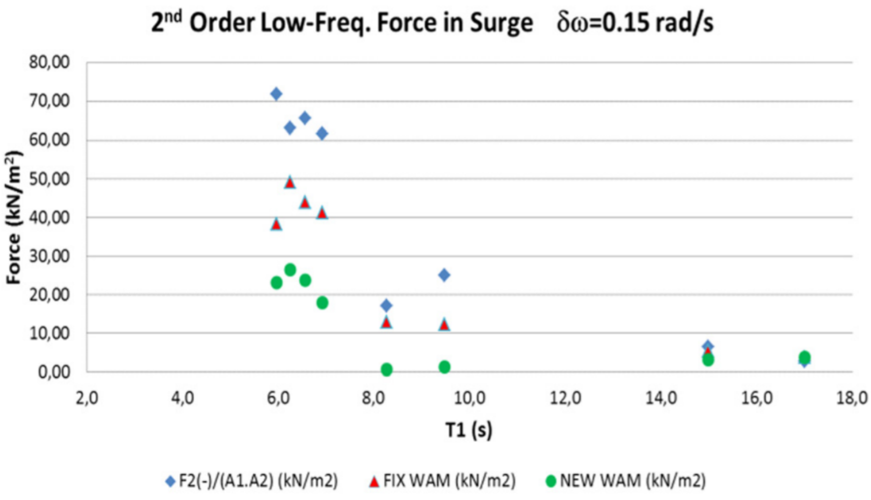

Extracted from (LOPEZ-PAVON et al., 2015).

Still there are other examples depicting large differences in motions related to the second-order wave forces, such as OC5 and OC6, two FOWTs. During their projects, Wang et al. (2022) have noticed persistent underpredictions of surge motions with potential codes, including OpenFAST, a time-domain software which uses WAMIT as input in this case. The authors have performed experimental tests according to Tab. 2.3, with fixed and freely floating conditions and for irregular (LC 3.3 and LC 5.3) and "white noise" waves (LC 3.4 and LC 5.3). Figure 2.8 introduces the experimental set and the natural period of the system is 105s.

Table 2.3: Irregular and white noise waves tested with OC6. Adapted from (WANG et al., 2022).

ID	Hs (m)	Wave Period (s)	Condition
LC 3.3	7.4	Tp = 12.0	Fixed
LC 5.3	7.4	Tp = 12.0	Freely floating
LC 3.4	6.7	6.0 to 26.0	Fixed
LC 5.4	6.7	6.0 to 26.0	Freely floating

Figure 2.8: Experimental set-up. (a) Geometry of the OC6-DeepCwind semi-submersible and the adopted coordinate system for both the fixed and the freely floating configurations. (b) The taut-spring mooring setup for the floating configuration.

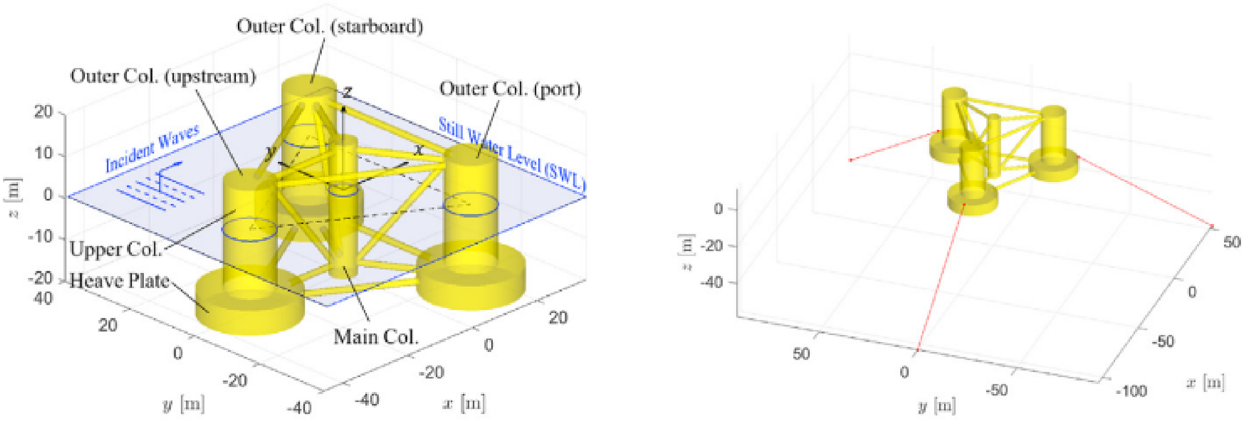

(a) Floater geometry and coordinate system.

(b) Mooring setup.

Extract from (WANG et al., 2022).

Results presented in Fig. 2.9 shows in pink the low-frequency region and in blue the wave frequency region. The comparisons are made in terms of power spectral densities (PSDs) of the forces and motions of surge and pitch. Fig. 2.9 (a) introduces that the surge force in the low-frequency range is underestimated by almost one order of magnitude while its motion is also underestimated in the same region, Figure 2.9 (b). The pitch force and motion in the low-frequency region is also smaller than it should, but in a less critical way (Fig. 2.9 (c) and (d)). However, in the case of the motions, other factors such as the viscous overprediction of the damping may also have contributed to the differences.

Figure 2.9: Power spectral densities (PSDs) of the wave-induced (a) surge force, Fx, and (b) pitch moment, My, on the DeepCwind offshore wind platform when constrained (LC 3.3), and PSDs of (c) surge motion and (d) pitch motion of the platform when freely floating (LC 5.3). The pink region indicates the low-frequency range, and the blue region is the wave frequency range.

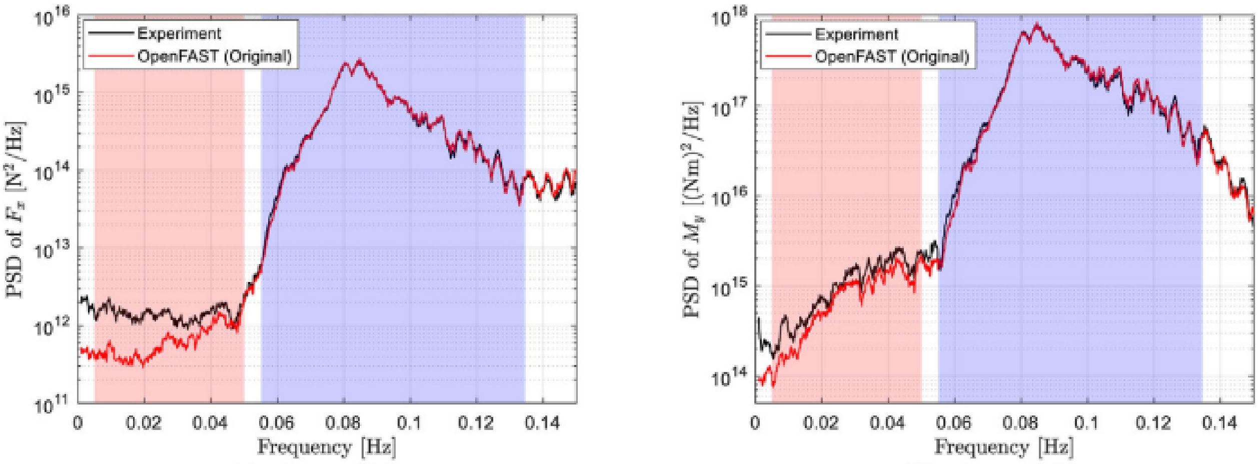

(a) PSDs of F_x. (b) PSDs of M_y.

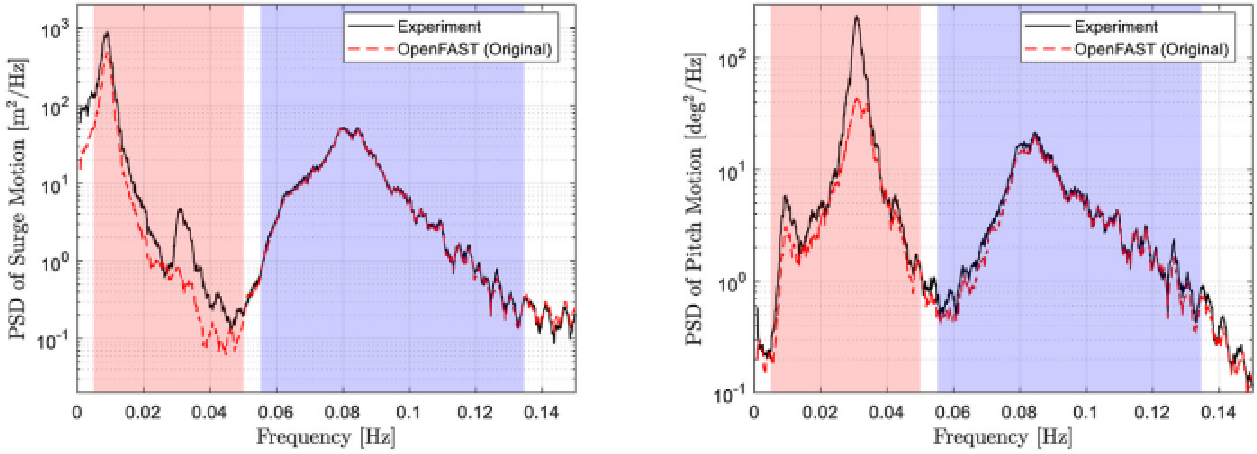

(c) PSDs of surge motion. (d) PSDs of pitch motion.

Extract from (WANG et al., 2022).

In order to overcome those divergences, Wang et al. (2022) have proposed some improvements to the OpenFAST code based on two factors: at the low-frequency region, the transverse viscous drag force is the main contributor to the surge force near to the waterline; and the diffraction can be neglected. Regarding the surge degree of freedom, authors modification was the use of an increased transverse drag coefficient, near to the waterline and along to a vertical wave stretching, similar to what Berthelsen et al. (2009) have proposed. At the columns, a transverse drag coefficient smaller than those obtained in experiments with free decay and forced oscillations was used. These changes reflected in a much improved agreement between both surge forces and motions, see Fig. 2.10.

Figure 2.10: Surge force, Fx; on the fixed semi-submersible in irregular waves (LC 3.3).

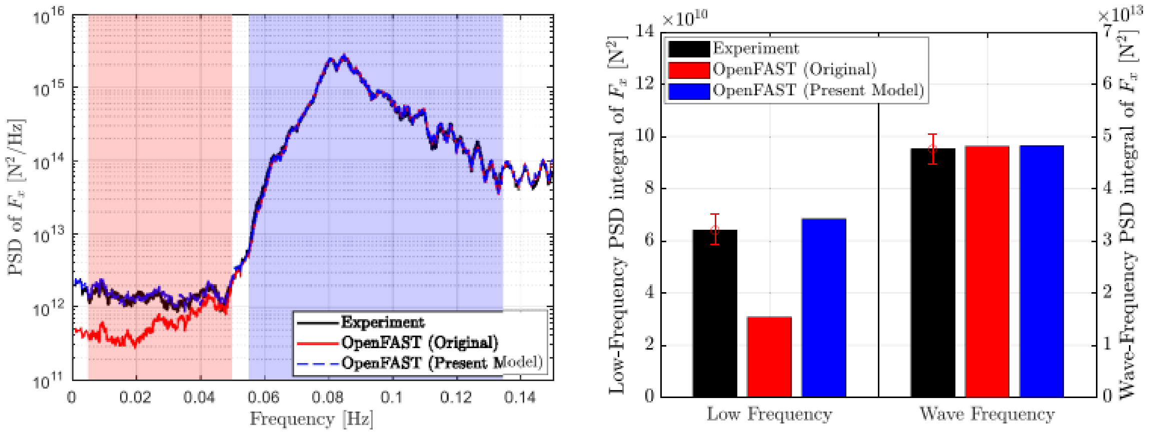

(a) PSDs of F_x.

(b) PSD integrals of F_x.

Extract from (WANG et al., 2022).

Wang et al. (2021), in order to examine the underprediction of the potential codes, carried out the 1:50 fixed tests with the OC5-DeepCwind model and compared them with CFD simulations performed by many different labs and software. Figure 2.11 demonstrates the experimental setup of the fixed platform without the central main column and cross-members.

Figure 2.11: Experimental setup of the fixed OC5-DeepCwind semi-submersible simplified.

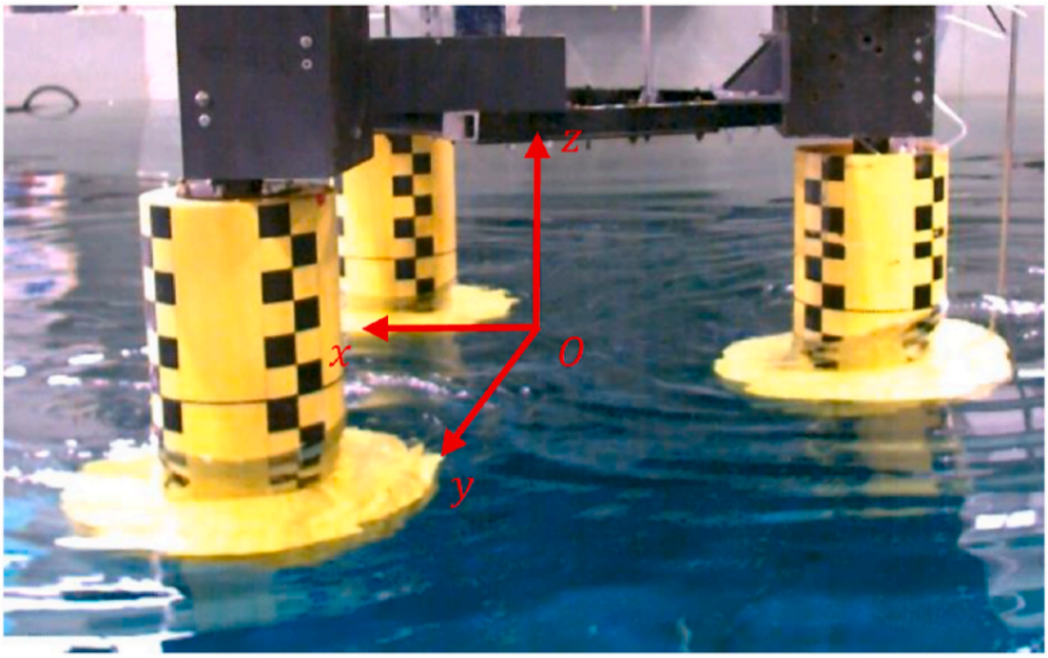

Extract from (WANG et al., 2021).

The tests were all performed at head bichromatic waves (from right to left in Fig. 2.11), as can be seen in Tab. 2.11. Wave B4 difference frequency is close to the resonance of surge.

Table 2.4: Bichromatic waves tested in full scale. Adapted from (WANG et al., 2021).

ID	$A_1(m)$	$A_2(m)$	$T_1(s)$	$T_2(s)$	Diff. Frequency (H_z)
B1	1.76	1.75	11.9000	8.6172	0.0320
B3	1.24	1.30	11.9000	8.6172	0.0320
B4	1.75	1.82	11.9000	10.5778	0.0105

After analyzing the imprecision about both numerical and experimental tests, the authors have compared the surge forces of the CFDs results, potential codes (hatched) and experiments at the difference frequency $|X_1^{(-)}|$ and at both wave frequencies, $|X_{1,1}|$ and $|X_{1,2}|$, see Fig. 2.12 to 2.13. The uncertainty bars refer to the difficulties in accurately capturing the nonlinear waves forces. In general, although at the wave frequency regions the potential codes show good responses, results confirm the underprediction of them at the difference frequency. Wave B4 shows even a more evident divergence between the potential software and experimental results at the difference frequency. On the other hand, CFD-FVM simulations have presented better agreement responses with the experiments at all frequencies regions, although, it is possible to see a wider difference between the CFD labs results in wave B4.

Figure 2.12: Normalized wave-exciting surge force on the entire floater at the difference and two wave frequencies for Wave B1 through experiments (EXP), CFD-FVM (colored bars) and potential codes (hatched bars).

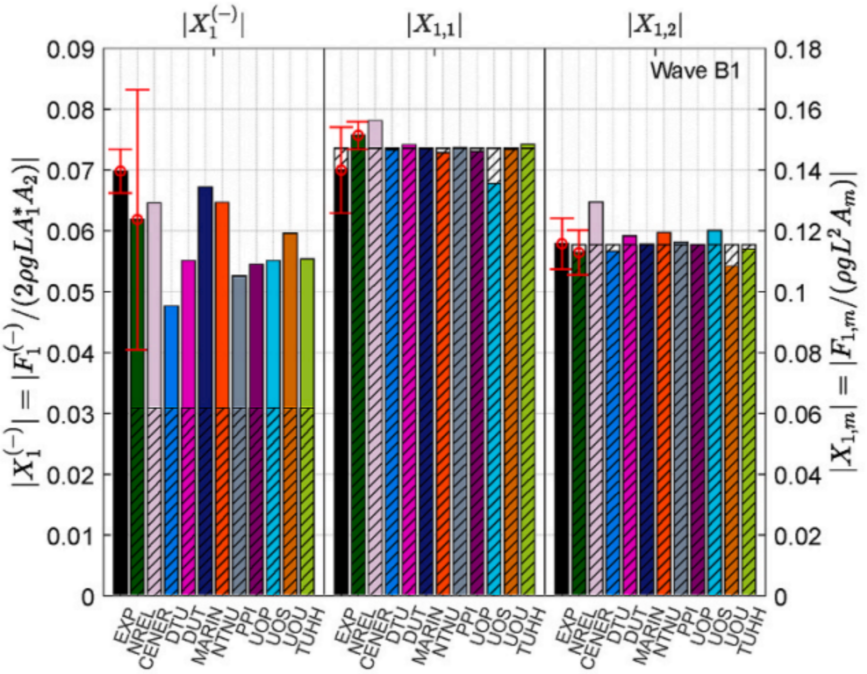

Extract from (WANG et al., 2021).

Figure 2.13: Normalized wave-exciting surge force on the entire floater at the difference and two wave frequencies for Wave B3 through experiments (EXP), CFD-FVM (colored bars) and potential codes (hatched bars)..

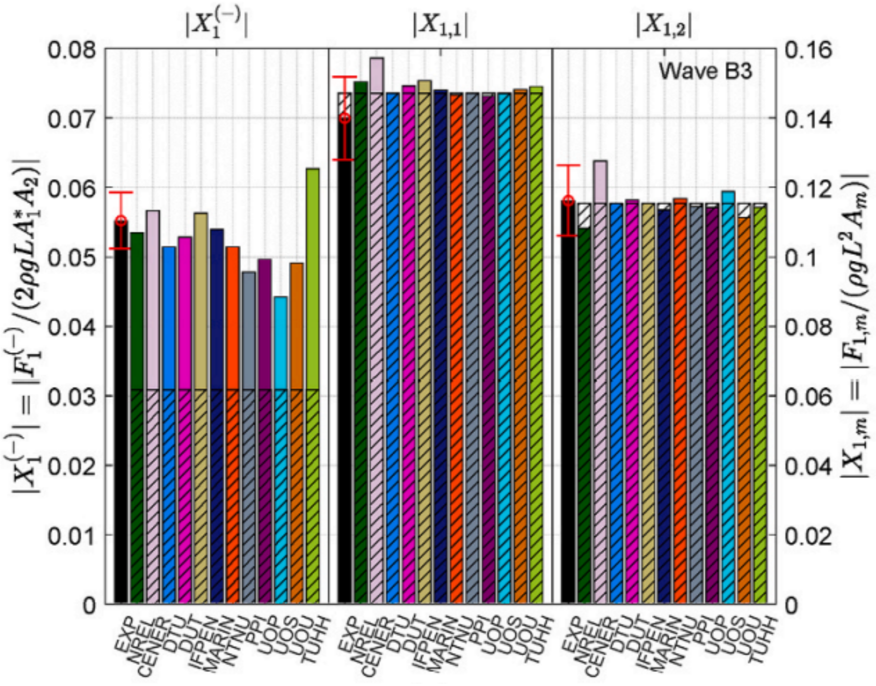

Extract from (WANG et al., 2021).

Figure 2.14: Normalized wave-exciting surge force on the entire floater at the difference and two wave frequencies for Wave B4 through experiments (EXP), CFD-FVM (colored bars) and potential codes (hatched bars)..

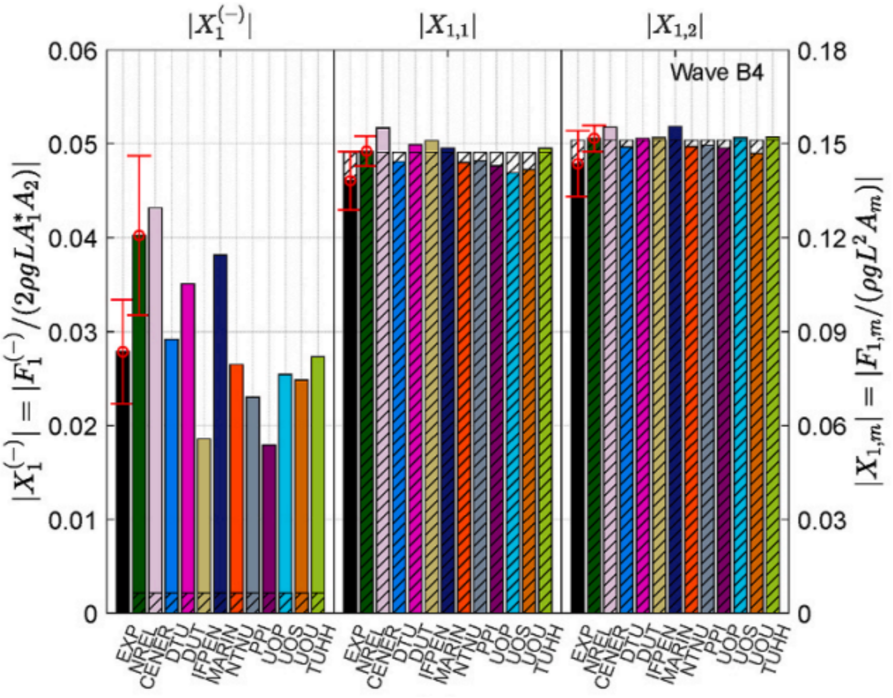

Extract from (WANG et al., 2021).

According to the authors, the underprediction of the potential codes regarding the surge forces is most likely due to the viscous drag excitation on the platform, which is not computed in the BEM codes and is accounted for in the FVM simulations.

Indeed for severe waves this may be the leading source of error, but what could explain the results deviations between BEM codes and experiments even in mild waves? To seek this answer, it is necessary to go back to basics. Next section will address works related to the cylinders interference phenomenon.

2.2 Numerical and experimental studies on wave forces acting on cylinders arrays

Studies pursuing to understand the wave cylinder interaction on arrays or any arrangement is a valuable way to substantiate the semi-submersible problem. Vadholm (2017) presented a fundamental work to discern how to divide the problem. The author proved through OpeamFOAM code that for a single 3D cylinder and on common environmental conditions, the viscous forces are insignificant in relation to the pressure forces.

Kamath et al. (2015) gives a vision about how the wave forces vary with the different number of cylinders in a row for low and high steepness waves. An illustration of this study is presented in Fig. 2.15 and 2.16, showing the wave elevation and the forces on each cylinder for each case. F_0 is the computed forces on the cylinder compared with the forces from the MacCamy and Fuchs (1954) theory. In summary, when downstream cylinders are added to the row, the wave force on a cylinder is increased and in all the cases, the most downstream cylinder presents the same forces as that on the single cylinder. These results are in accordance with the wave elevation field, in which the diffraction makes a redistribution of the wave field with the addition of downstream cylinders. Of course, the effect is more pronounced in the higher steepness case, however, for the low ones, it is also possible to observe the formation of a standing wave between the cylinders.

Figure 2.15: Free surface elevations in the vicinity of the cylinders in different arrangements for low steepness incident waves (H/L = 0.003) with H = 0.006 m and L = 2.0 m at t/T = 20.

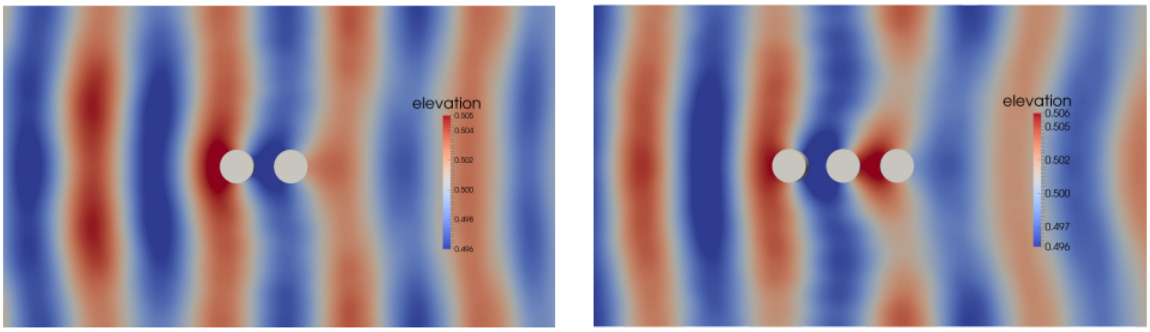

(a) two tandem cylinders

(b) three tandem cylinders

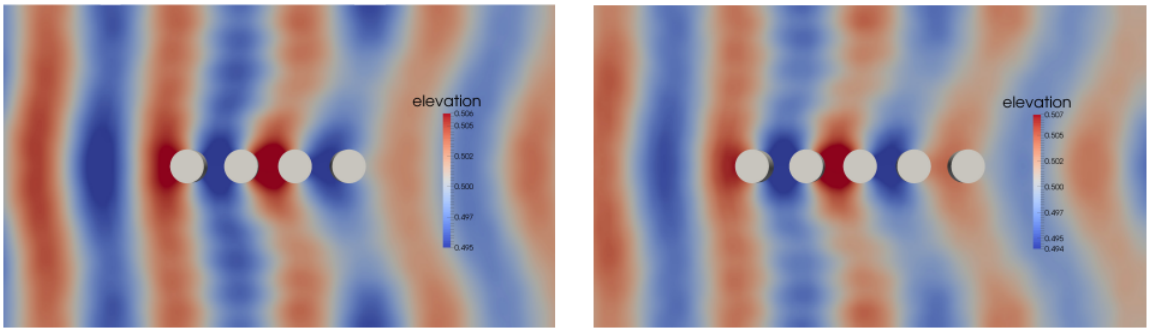

(c) four tandem cylinders

(d) five tandem cylinders

Extract from (KAMATH et al., 2015).

Figure 2.16: Wave forces on a single cylinder and in arrays of 1 to 5 cylinders for low steepness waves with H = 0.006 m and L = 2.0 m.

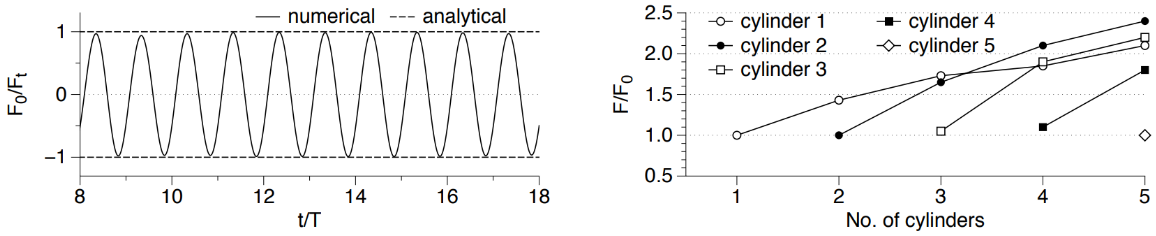

(a) Comparison of numerical and theoretical wave forces on a single cylinder

(b) Variation of wave forces on the different cylinders

Extract from Kamath et al. (2015).

Linton and Evans (1990), Callan, Linton and Evans (1991), Maniar and Newman (1997) and Evans and Porter (1997) have explored the effect of the forces on arrays of cylinders and contributed to the concept of near-trapped waves. Maniar and Newman (1997) investigated the force on each cylinder on a long array of bottom mounted identical cylinders for head seas and four wavenumbers, as introduced by Fig. 2.17. The forces magnitude were normalized as MacCamy and Fuchs (1954) proposed for a single cylinder and phase was normalized for each wavenumber. On the top figure, in which the long waves are represented, the forces increase slowly along the array. On the other hand, the third and the very bottom figures present a short wave regime in which the forces are greater in the beginning of the array and, because of sheltering, they reach minimum at the end.

The second figure, nevertheless, refers to a wavenumber $kd = 1.3907$, which is virtually the same value found by Callan, Linton and Evans (1991) and which is associated with the existence of trapped waves, for the case of a circular cylinder in the center of a channel with the width twice as wide as the radius of the structure. The spacing parameter d, in this case, is related to the cylinders radius α by $\alpha/d = 0.5$. Indeed, in this scenario, Fig. 2.17 illustrates extremely larger forces in relation to the other wavenumbers.

Figure 2.17: The distribution of the force magnitude (left) and phase (right) along an array of 100 circular cylinders in head seas.

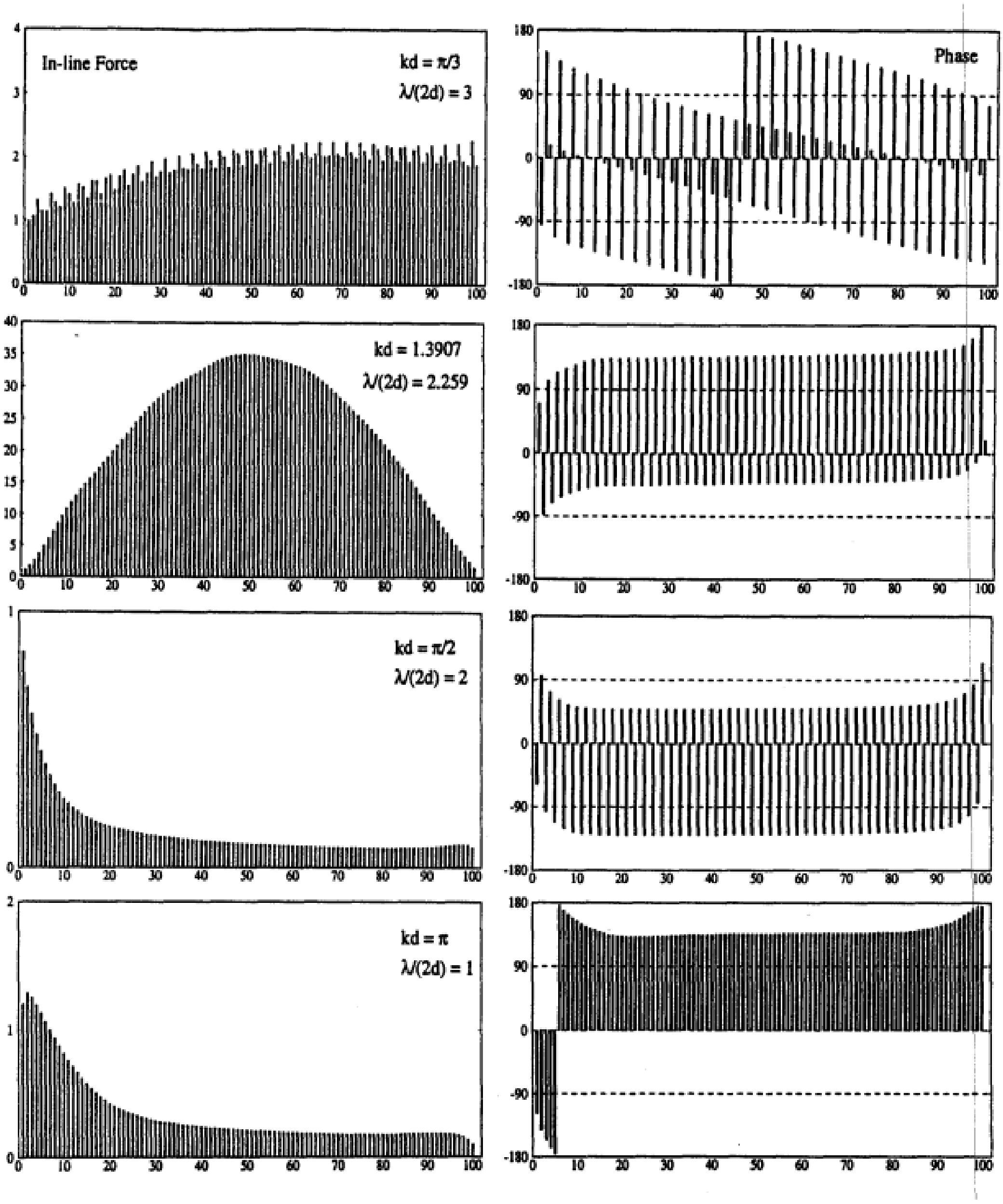

Extract from (MANIAR; NEWMAN, 1997).

The discussion of the Maniar and Newman (1997) paper made by D. V. Evans states that "Although a pure trapped mode for such configuration seems unlikely", here Evans is referring to the regular circular array of cylinders, "near-trapping might occur in some cases, resulting in an exceptionally large force on the cylinders at a particular incident wavelength and cylinder spacing." Naturally, this means that near-trapping is a local oscillation that decays gradually as the energy is dissipated due to the wave radiation. This oscillation can happen on an array of cylinders or platform columns at a very well-defined period. He also has noticed that if placing four cylinders in a square, the near-trapping occurs in the wave period at which the wavelength is almost exactly equal to the gap between the cylinders along the flow. Here an important contribution from Linton and Evans (1990) should be recalled as they have detected that the forces on cylinder arrays increase as the gap between them decreases.

Evans and Porter (1997) goes further on this subject by bringing up the discussion to the near-trapping mode on mean drift forces. The authors have evaluated 4 cylinders in a square arrangement, as well as 5 and 6 cylinders in circular layout, as Fig. 2.18 presents. In order to intensify this phenomenon, the cylinders are placed very close to each other on purpose, even though this is not likely a real semi-submersible configuration.

Figure 2.18: Arrangement, dimensions and cylinder labels for circular arrays of four, five and six cylinders.

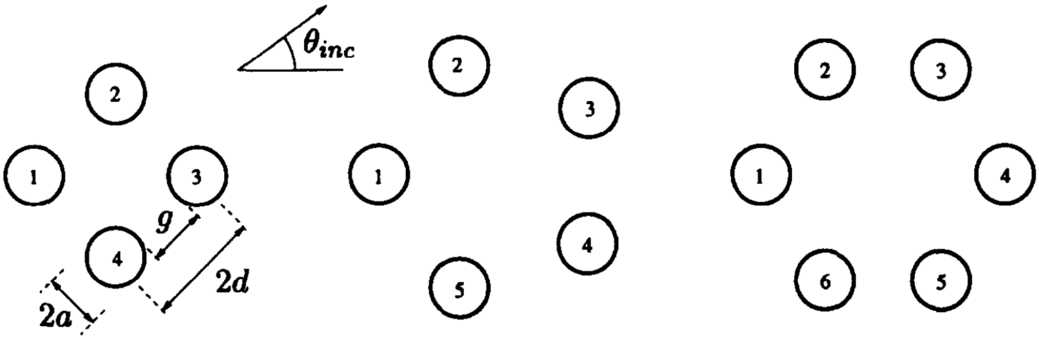

Extract from (EVANS; PORTER, 1997).

Figure 2.19 introduces the force on four cylinders against wave number for the five different distances between the columns starting from the far conditions to the closer ones. Two remarkable points are of interest here: the force peak value changes with the wavelength depending on the distance between the columns, as it was already addressed by the authors cited previously; and the force significantly increases as the cylinders get closer to each other.

Figure 2.19: Resultant force on each one of the four cylinders against wave number, ka, and a variety of a/d = 0.5 (a), 0.55 (b), 0.6 (c), 0.7 (d), 0.8 (e), wave progressing in the positive x-direction ($\theta_{inc} = 0$)

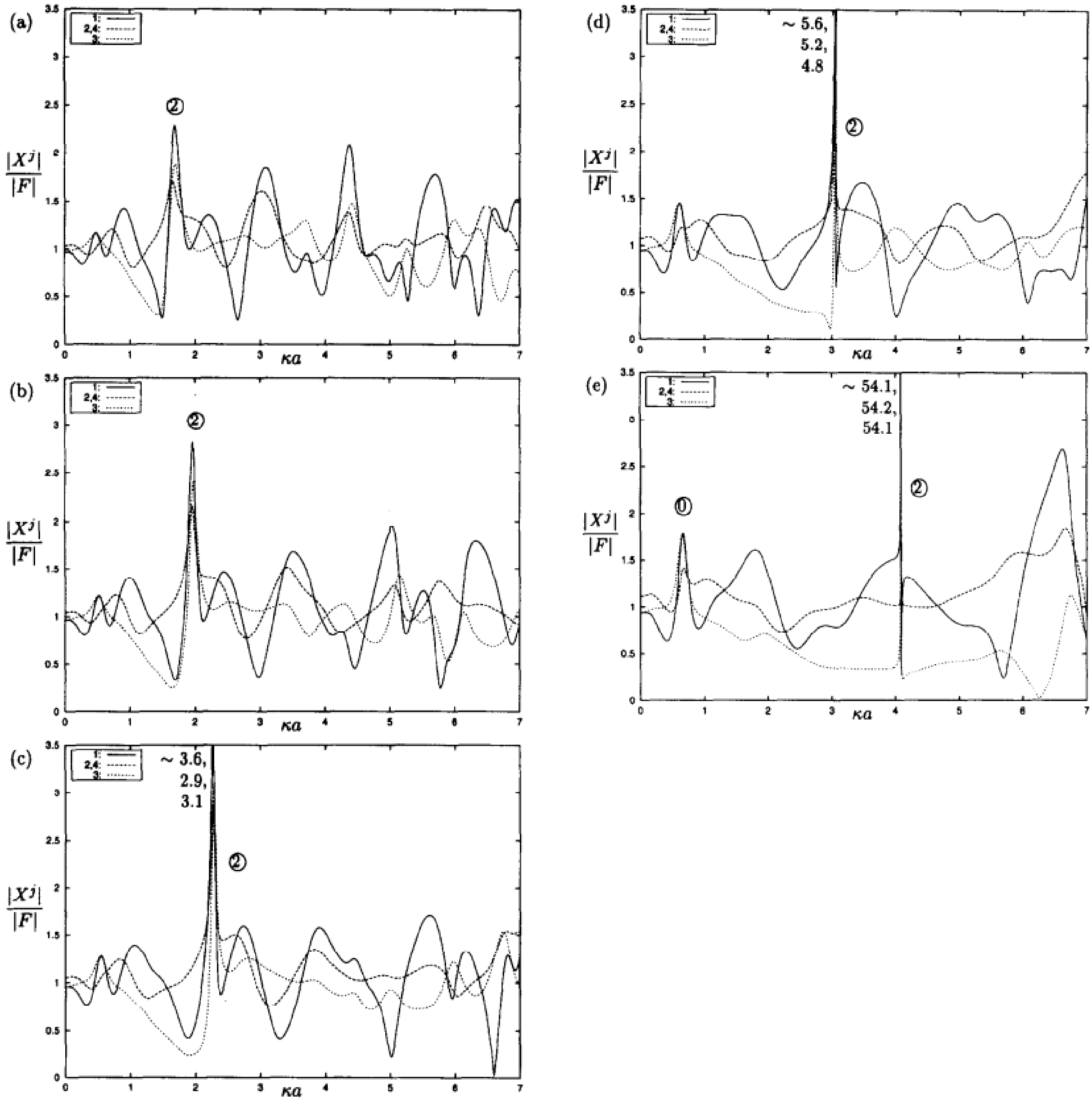

Extracted from (EVANS; PORTER, 1997).

Furthermore, the authors did notice that the peak drift forces for the three arrangements seem to be related to the square of the corresponding peak first-order forces. For exemplifying the problem, the case with a/d = 0.8 is observed. The modulus of the mean second-order drift forces in the resonant case for this arrangement was 2384, 2393 and 2364 for respectively cylinder 1, 2 and 4, and 3. Another finding was that the largest forces look to occur precisely when the near-trapped mode is associated with a standing wave motion.

As if the complexity related to the near-trapping phenomenon was not enough, there is still one more complicated event that may occur in semi-submersible platforms: the negative wave drift damping, which is going to be addressed in next section.

2.3 Wave Drift Damping

Not only the forces on semi-submersible platforms are sometimes still obscure. Damping is also a paramount input parameter on predicting slow-drift motions, which is hardly ever an assertive value. In addition to the uncertainties related to the viscous damping, in some cases there is still the wave drift damping phenomenon acting significantly on the structures. According to Newman (1993) these nonlinear surface wave effects derives from low-frequency oscillatory motions of a vessel when it is facing an incident wave. In accordance with Aranha (1994), the drift velocity can influence the exciting forces. The curious phenomenon here is that wave drift damping is generally positive for ship-shaped bodies or other simple forms; however, for more complex geometries, there are some evidences that these damping may lead to negative values.

Nossen, Grue and Palm (1991) has showed this phenomena by comparing two types of bodies. The first graph in Fig. 2.20 represents the wave drift damping (y-axis) for a range of frequencies (x-axis) of a singular vertical cylinder floating in a wave field. The second graph represents the wave drift damping for four vertical cylinders, equal to the one of the first analysis, placed symmetrically on x-axis and y-axis. The first evaluation provided only positive values of wave drift damping; nevertheless in the second analysis, the damping showed negative values at some frequencies, probably caused by interactions between the cylinders. C_F is the drift force coefficient, a is the cylinder radius, U is the relative speed.

Figure 2.20: Wave drift damping computation for one cylinder by two different methos (left) and for four cylinders (right).

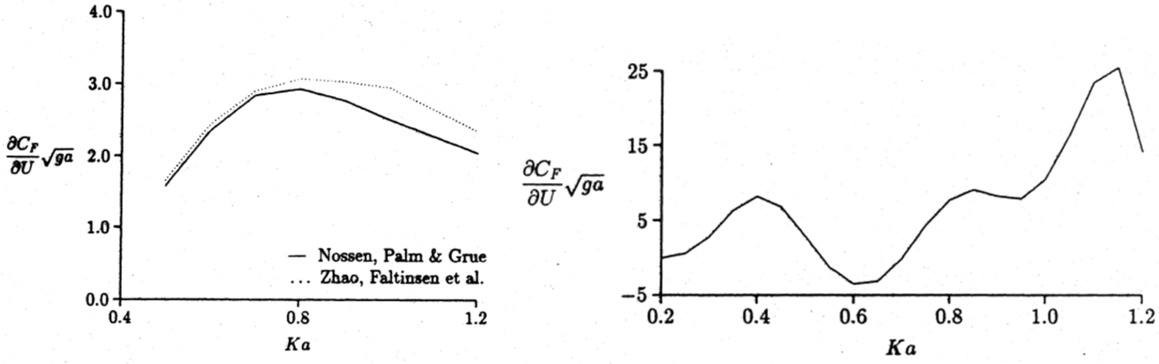

Extracted from Nossen, Grue and Palm (1991).

Other authors, such as Yang, Nestegård and Falkenberg (2018) also have reached negative wave drift damping values for semi-submersible type platforms. They have used a different formulation than Nossen, Grue and Palm (1991) for the computations and they also obtained similar results, as Fig. 2.21 presents.

Figure 2.21: Wave drift damping computation for a semi-submersible platform.

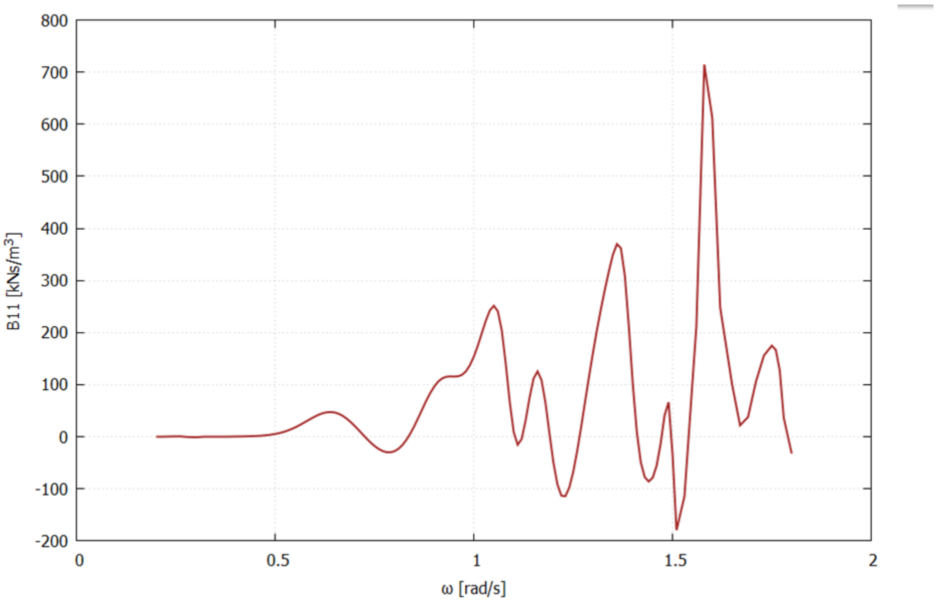

Extracted from Yang, Nestegård and Falkenberg (2018).

Hence, on semi-submersible type platforms, the phenomenon of both negative and positive wave drift damping can interfere much in the total motions of the system. Regarding the potential software, the wave drift damping can only be accounted for in time-domain simulations. AQWA employs Aranha (1994) formulae in its resolution, which is compounded by the drift matrix equation for a vessel with small forward speed and in surge and sway dependent on drift coefficients that are given also by Aranha (1994). The coefficients are based on wave frequency and heading, drift forces and moments.

3 Theoretical Background

This chapter is addressing a snip of the classic formulation for second-order waves forces provided by Pinkster (1980) based on the potential flow theory and which is used as a basis by the Boundary Element Method (BEM) of diffraction/radiation codes. Both Boundary Element or Finite Volume Methods (FVM) theory can easily be found in the literature, and they are not going to be minutely addressed here because their formulation is not in focus in the present thesis.

A freely floating structure without a mooring system or any other restraint feature will drift slowly and steadily in the direction of the wave due to the action of the drift forces (PINKSTER, 1980). The slow-drift motion is related to interactions between waves with different frequencies that compose the sea and which are responsible to create wave groups (PINKSTER, 1980). Figure 3.1 shows a regular wave group and indicates the low-frequency second-order wave elevation, which is represented by a long wave in the graph (dark blue dashed line).

Figure 3.1: Representation of a wave group structure.

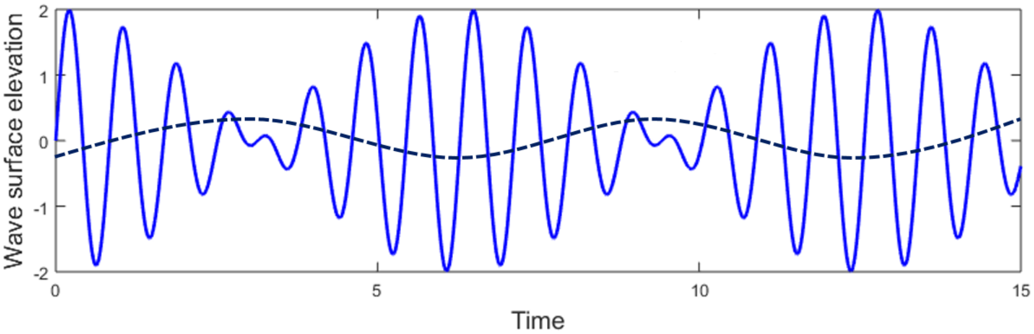

The magnitude of second-order wave forces is significantly lower than those of first-order. However, when a moored vessel faces an irregular sea, the drift forces may have components with the same frequencies as surge, sway or yaw natural frequencies, inducing resonant responses to the system. In addition, the problem is amplified by small levels of damping that usually characterize the horizontal degrees of freedom, leading to large amplitude motions.

Regarding the second-order wave forces, they are composed of terms of difference-frequency and are related to the drift forces, which are compounded by slow-drift and mean drift forces; and the sum-frequency, as is shown in Fig. 3.2.

Figure 3.2: Decomposition of the second-order wave forces.

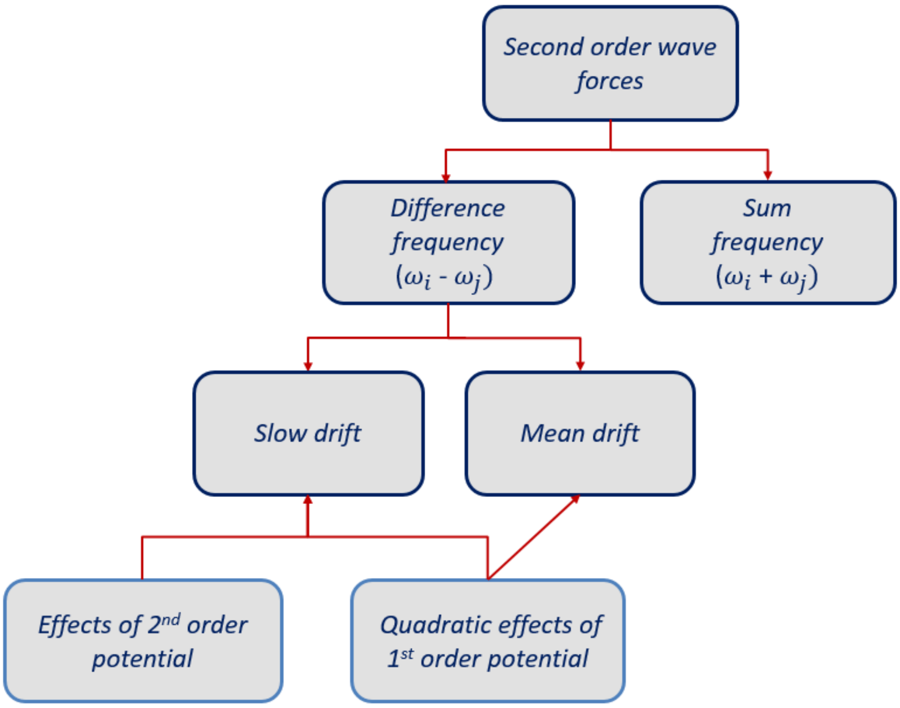

One way to demonstrate how the terms of difference-frequency and sum-frequency arise is through the pressure at a point within the fluid, using Bernoulli's equation, Eq. 3.1. Here, P is the pressure on the free surface, P_{atm} is the atmospheric pressure, ρ is the water density, g is the gravity acceleration and ζ is the free surface elevation. This relation is only one of many that contribute to the second-order forces.

$$P = P_{atm} - \rho\frac{\partial\phi}{\partial t} - \rho\frac{\nabla\phi^2}{2} - \rho g\zeta \tag{3.1}$$

Now taking the quadratic term in Eq. 3.1, which corresponds to a second-order term, and call it as $P^{(2)}$:

$$P^{(2)} = \frac{1}{2}\nabla\phi.\nabla\phi \tag{3.2}$$

Applying Eq. 3.2 on the superposition of two waves, $wave_1$ and $wave_2$ as presented in Fig. 3.1, the velocity potential field is provided in Eq. 3.3 and the pressure second-order term becomes Eq. 3.4.

$$\nabla\phi = \nabla\phi_1 + \nabla\phi_2 \tag{3.3}$$

$$P^{(2)} = \frac{1}{2}(\nabla\phi_1\nabla\phi_1 + 2\nabla\phi_1\nabla\phi_2 + \nabla\phi_2\nabla\phi_2) \tag{3.4}$$

However, each $wave_j$ has a velocity component with amplitude $\nabla\varphi_j$ and phase ε_j as Eq. 3.5 states.

$$\nabla\phi_j = \mathbb{R}\left\{\nabla\varphi e^{i\varepsilon_j} e^{i\omega_j t}\right\} \tag{3.5}$$

Further, the complex amplitude of the flow velocity term, $\nabla\varphi_j e^{i\varepsilon_j}$, can be expressed as Λ_j, as is shown in Eq. 3.6.

$$\nabla\phi_j = \mathbb{R}\left\{\Lambda_j e^{i\omega_j t}\right\} \tag{3.6}$$

Then, taking the real part of Eq. 3.6, Eq. 3.7 is derived in which $\Lambda_j^* = \nabla\varphi e^{-i\varepsilon_j}$ is the complex conjugate of Λ_j.

$$\nabla\phi_j = \frac{1}{2}\left\{\Lambda_j e^{i\omega_j t} + \Lambda_j^* e^{-i\omega_j t}\right\} \tag{3.7}$$

Finally, by taking each term from Eq. 3.4 and applying Eq. 3.7 to them, Eq. 3.8 and Eq. 3.9 are derived.

$$\nabla\phi_j.\nabla\phi_j = \frac{1}{4}\left\{(\Lambda_j\Lambda_j)e^{i(2\omega_j)t} + 2(\Lambda_j\Lambda_j^*)e^{i(0)t} + (\Lambda_j^*\Lambda_j^*)e^{-i(2\omega_j)t}\right\} \quad \text{for } j = 1 \text{ or } j = 2 \tag{3.8}$$

$$2\nabla\phi_1.\nabla\phi_2 = \frac{1}{2}\left\{(\Lambda_1\Lambda_2)e^{i(\omega_1+\omega_2)t} + (\Lambda_1\Lambda_2^*)e^{i(\omega_1-\omega_2)t} + (\Lambda_1^*\Lambda_2)e^{i(\omega_1-\omega_2)t} + (\Lambda_1^*\Lambda_2^*)e^{-i(\omega_1+\omega_2)t}\right\} \tag{3.9}$$

The low frequency forces are compounded by the sum of difference-frequencies of each pair of the wave components $(\omega_i - \omega_j)$. If the terms of a pair have the same frequencies $\omega_j = \omega_j$ their contribution to the wave drift forces is constant over time and they are named as mean drift. Otherwise, the pairs that contain frequencies with values close to each order $\omega_j \approx \omega_j$ are responsible for contributing to the part that slowly varies in the drift forces, resulting the well-know slow-drift.

Lastly, the sum-frequency is compounded by the sum of the frequencies of all terms of the wave pairs $(2\omega_i)$, $(2\omega_j)$ and $(\omega_i + \omega_j)$ corresponding, frequently, to the double of the wave frequencies. In other words, this part of second-order wave forces usually has significantly higher frequencies than the typical wave frequencies, thus, they are not very decisive to the mooring systems in catenary and horizontal plane motions regarding slow-drift motions and can be ignored in analysis like this.

Good predictions of the drift forces are also required so that mooring systems can be designed in order to maintain the platform offsets in predetermined limits. The major issue is: how to do that efficiently and in a sufficiently accurate manner? It is already known that the real sea is a natural and an intensely aleatory phenomenon; therefore, it can be imagined how complex it is to assess the non-linear forces related to them. Some of the procedures frequently adopted to tackle this problem will be given in the following sections.

3.1 Stokes' pertubation technique

In 1847, Stokes established a perturbation technique which transforms the non-linear wave problem in a sequence of other linear problems in different orders of magnitude (STOKES, 1847). This procedure can be employed when the fluid is assumed as homogeneous, inviscid and incompressible, in addition to the flow being irrotational, of course.

As an example, Eq. 3.10 demonstrates how the technique is applied to the velocity potential, ϕ, decomposing the problem into a power series in relation to the wave steepness parameter, ε. In fact, the problem can be solved separately by order of magnitude. The zero order components are represented by the term ε^0 and refer a possible component of the flow that is not related to the incoming wave (for systems with no forward speed, this component is null); the first-order by ε^1 and the second-order by ε^2, and so on. At first instance, people were not concerned with the non-linear parameters because of their order of magnitude. However, paying attention to the behavior of a moored system, it is visible that it moves slowly side to side around a non zero mean position in surge, sway and yaw. These phenomena defined as, respectively, slow-drift and mean-drift motions, appear due to the low and mean frequency second-order wave forces also known as wave drift forces. Into some numerical software such as CFD based on FVM, the implementation of the Stokes' expansion for modelling a wave is found until the fifth-order.

$$\phi(x,y,z,t) = \varepsilon^0\phi_0(x,y,z,t) + \varepsilon\phi_1(x,y,z,t) + \varepsilon^2\phi_2(x,y,z,t) + ... + \varepsilon^n\phi_n(x,y,z,t) \tag{3.10}$$

Stokes is responsible for providing this technique in the fluid dynamics area, which is actually the origin for later significant works. One of the most remarkable thesis in this field uses this technique with three dimensional bodies into the domain: Pinkster (1980). In his thesis, since there was no code capable of solving the complete second-order problem, Pinkster (1980) proposed an approximation for the second-order potential which depends on quadratic first-order quantities.

3.2 Boundary conditions according to Pinkster (1980)

Following the potential flow concept, Stokes' expansion technique in conjunction with the Taylor series expansion provides the boundary conditions to solve the problem. Indeed, boundary conditions are related to the physical restrictions that the flow must respect into the domain. In the present work, they may be expressed analytically in terms of the potential flow and the free surface elevation. As Fig. 3.3 shows, the fluid domain has three boundaries: free surface, surface of the body, the sea floor. Along with the potential flow theory, conditions for of each of boundaries must be respected. In addiction, there is one more condition that applies to the fluid domain and another related to the far field. Following Pinkster (1980), the development procedure for obtaining them will be presented next.

Figure 3.3: Fluid domain boundaries.

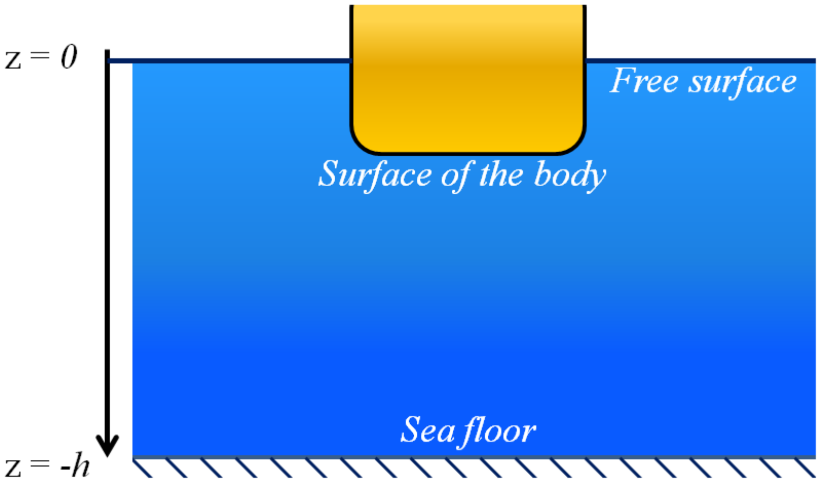

Part of the boundary conditions is modified if the second-order is included into the problem, other conditions will remain the same. The linear hypothesis assumes that the waves have small steepness, as Eq. 3.11 presents.

$$\frac{A}{\lambda} << 1 \qquad \text{or} \qquad kA << 1 \tag{3.11}$$

Some boundary conditions are imposed on the instantaneous free surface S or $z = \zeta$, which is divided at the mean wetted surface of the hull S_B and an increment that oscillates due to the body motions S_I. However, S_I is unknown, which makes the problem harder to be solved. Looking at Fig. 3.4, the first-order boundary conditions are imposed to the mean surface $z = 0$ and the second-order must be applied at the instantaneous free surface $z = \zeta$.

Figure 3.4: Boundaries conditions limits at free surface and at the body.

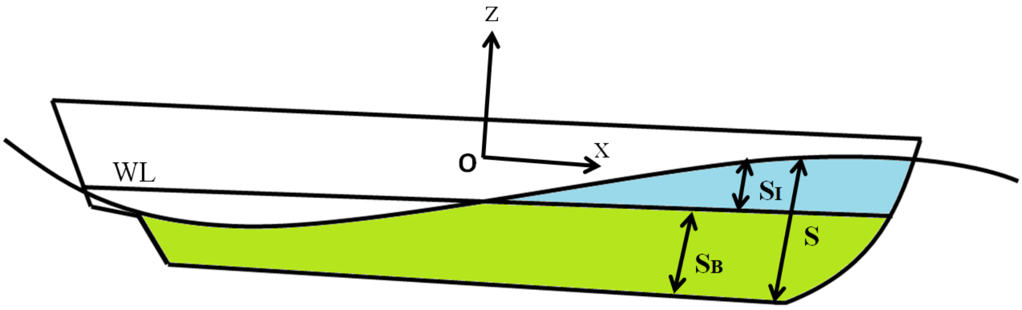

3.2.1 Boundary condition within the fluid

When considering the fluid incompressible, homogeneous and inviscid and the flow irrotational, the flow can be written in terms of the velocity potential, Eq. 3.10. Therefore, the boundary condition in the fluid domain is related to the Laplacian operator, which needs to satisfy the equation of continuity. This condition, considering the second-order terms, does not differ from the first-order, as Eq. 3.12 and 3.13 demonstrate.

$$\nabla^2\phi^{(1)} = 0 \tag{3.12}$$

$$\nabla^2\phi^{(2)} = 0 \tag{3.13}$$

3.2.2 Boundary condition at the free surface

It is not hard to define a free surface through a figure, but it is hard to think about it in terms of words. Pinkster (1980) states that *"The (unknown) free surface is a surface of constant pressure and the velocity component of the fluid normal to the free surface is equal to the velocity of the surface in the same direction".* This statement leads to two boundary conditions at the free surface: cinematic and dynamic. The first asserts that no fluid particles can pass through this boundary. The second implies that the pressure must be constant and equal to the atmospheric local pressure.

The cinematic boundary condition can be written mathematically by the relation in which the projection of the velocity vector of the particle $\bar{V}_p$ in the normal direction of the surface $\bar{n}_s$ must be equal to the projection of the velocity vector of the surface $\bar{V}_s$ in the same direction $\bar{n}_s$, as Eq. 3.14 demonstrates.

$$\bar{V}_p.\bar{n}_s = \bar{V}_s.\bar{n}_s \tag{3.14}$$

Thus, the cinematic compatibility, considering that the free surface is described by $z =$

$\zeta(x,t)$, is set by Eq. 3.15.

$$\frac{\partial \phi}{\partial z} = \frac{\partial \zeta}{\partial t} + \frac{\partial \zeta}{\partial x}\frac{\partial \phi}{\partial x} \quad \text{in } z = \zeta \tag{3.15}$$

However, for the first-order potential, the small steepness hypothesis is taken into account, therefore the second term in Eq. 3.15 can be neglected, resulting in Eq. 3.16.

$$\frac{\partial \phi}{\partial z} = \frac{\partial \zeta}{\partial t} \quad \text{in } z = 0 \tag{3.16}$$

The dynamic boundary condition is obtained from the Bernoulli's equations, Eq. 3.1, and it states:

$$P - P_{atm} = 0 \tag{3.17}$$

Then, replacing Eq. 3.17 in Eq. 3.1 and isolating the free surface elevation component, Eq. 3.18 is obtained.

$$\zeta = -\frac{1}{g}\left(\frac{\partial \phi}{\partial t} + \frac{\nabla \phi^2}{2}\right) \quad \text{in } z = \zeta \tag{3.18}$$

Moreover, for the first-order boundary condition, the term $\nabla \phi^2$ can be neglected due to small steepness hypotheses. Also, the instantaneous surface at $z = \zeta$ is not known at first, which results in another non-linear source to the problem. Therefore, the linearized kinematic boundary condition is given by Eq. 3.19.

$$\zeta = -\frac{1}{g}\left(\frac{\partial \phi}{\partial t}\right) \quad \text{in } z = 0 \tag{3.19}$$

Further, it is possible to assemble these boundaries conditions, as Eq. 3.20, through the Stokes expansion 3.10 of Eq. 3.19 applied to the Taylor series around $z = 0$.

$$g\frac{\partial \phi}{\partial z} + \frac{\partial^2 \phi}{\partial t^2} = -2\nabla \phi . \nabla \left(\frac{\partial \phi}{\partial t}\right) + \frac{\nabla \phi . \nabla (\nabla \phi^2)}{2} \tag{3.20}$$

Hence, Pinkster (1980) obtains the homogeneous first-order free surface boundary condition Eq. 3.21 and the non-homogeneous second-order Eq. 3.22. Both potentials are computed on the mean surface $z = 0$.

$$g\frac{\partial \phi^{(1)}}{\partial z} + \frac{\partial^2 \phi^{(1)}}{\partial t^2} = 0 \tag{3.21}$$

$$g\frac{\partial \phi^{(2)}}{\partial z} + \frac{\partial^2 \phi^{(2)}}{\partial t^2} = -2\nabla \phi^{(1)} . \nabla \left(\frac{\partial \phi^{(1)}}{\partial t}\right) + \frac{\partial \phi^{(1)}}{\partial t}\left(\frac{\partial^2 \phi^{(1)}}{\partial z^2} + \frac{1}{g}\frac{\partial^3 \phi^{(1)}}{\partial t^2 \partial z}\right) \tag{3.22}$$

Substituting the first-order potential $\phi^{(1)}$ in Eq. 3.22, an equation to the second-order potential with general terms is provided and divided in nine therms, in which the subscript w refers to the incoming waves potential, s to the scattering potential and r to the potential due to the body motions.

$$\phi^{(2)} = \phi^{(2)}_{ww} + \phi^{(2)}_{ss} + \phi^{(2)}_{rr} + \phi^{(2)}_{ws} + \phi^{(2)}_{wr} + \phi^{(2)}_{sw} + \phi^{(2)}_{sr} + \phi^{(2)}_{rw} + \phi^{(2)}_{rs} + \phi^{(2)}_{r} \tag{3.23}$$

In Eq. 3.23, any of the first nine terms on the right-hand side satisfies the non-homogeneous second-order boundary condition, Eq. 3.22, as $\phi^{(2)}_w$ and $\phi^{(2)}_s$. Thus, the second-order potential of the undisturbed incoming waves $\phi^{(2)}_w$ only depends on its first-orders potentials $\phi^{(1)}_w$, which can be obtained analytically at mean position $z = 0$. Nevertheless, the second-order scattering potential $\phi^{(2)}_s$ is dependent on its first-order potential, which in turn depends on the presence of the body in the domain. Otherwise, the potential due to body motions of Eq. 3.23, $\phi^{(2)}_r$, satisfies the homogeneous first-order boundary condition, Eq. 3.21.

3.2.3 Boundary condition at the sea floor

At the sea floor, no fluid particles should pass through the sea bottom. Physics here states an impermeability condition and since this condition is applied to a fixed boundary, there is no difference between the first and second-order, as Eq. 3.24 and Eq. 3.25 demonstrate. Hither, $\bar{n_b}$ is the normal vector at any surface point of the sea bottom.

$$\nabla\phi^{(1)}.\bar{n_b} = 0 \tag{3.24}$$

$$\nabla\phi^{(2)}.\bar{n_b} = 0 \tag{3.25}$$

3.2.4 Boundary condition on the body

The boundary conditions on the body have the physical meaning that no fluid enters the body; in other words, the relative velocity between the body and the fluid in the normal direction of the body surface must be zero. Equation 3.26 analytically presents this boundary condition with $\bar{N}$, the outward pointing normal vector of a surface element in the axes system out of the body, and $\bar{V}$, the velocity of each point (x_1, x_2, x_3) on the body surface. This equation must be satisfied at the instantaneous position of the body surface.

$$\nabla\phi.\bar{N} = \bar{V}.\bar{N} \tag{3.26}$$

For the first-order potential, the boundary condition on the body surface is represented by Eq. 3.27, in which $\bar{n}$ is the outward pointing normal vector in the system with the body axes with origin of the center of gravity.

$$\nabla\phi^{(1)}.\bar{n} = \bar{V}^{(1)}.\bar{n} \tag{3.27}$$

On the other hand, the problem for the second-order potential becomes a little more complicated, as Pinkster (1980) describes in Eq. 3.28.

$$\nabla\phi^{(2)}.\bar{n} = (\bar{V}^{(1)} - \nabla\phi^{(1)}).\bar{N} + \bar{V}^{(2)}.\bar{n} \tag{3.28}$$

At this point, some assumptions may be taken into account in order to simplify the problem. The motions are assumed to be small, hence, the Taylor expansion in the potentials can be applied at the mean position of the hull surface. The first-order boundary condition, Eq. 3.27 remains the same, except that now the first-order potential $\nabla\phi^{(1)}$ is calculated at the mean position of the body, not at the instantaneous position. In the second-order equation, Eq. 3.29, an adjustment term is added due to the first-order motion when the Taylor expansion is applied. Illustrated by Fig. 3.4, the first-order boundary condition is computed up to S_B or $z = 0$ and the second-order one up to S or $z = \zeta$.

$$\nabla\phi^{(2)}.\bar{n} = -(\bar{X}^{(1)}.\nabla).\nabla\phi^{(1)} + (\bar{V}^{(1)} - \nabla\phi^{(1)}).\bar{N} + \bar{V}^{(2)}.\bar{n} \tag{3.29}$$

Both in Eq. 3.27 and Eq. 3.28, the first-order potential is calculated by Eq. 3.30. Here, $\phi_w^{(1)}$ is the first-order potential of the undisturbed incoming waves, which physically means that there is no body on the wave domain. $\phi_s^{(1)}$ is the scattering wave potential, which represents the incoming waves acting on a fixed body. $\phi_w^{(1)}$ and $\phi_s^{(1)}$ together are defined as the diffraction potential that refers to the interaction of the incoming waves with a fixed body. Lastly, $\phi_r^{(1)}$ is the radiation potential in which there are no incoming waves, but the body moves and irradiates waves that propagate in the radial direction.

$$\phi^{(1)} = \phi_w^{(1)} + \phi_s^{(1)} + \phi_r^{(1)} \tag{3.30}$$

Now, Eq. 3.30 and Eq. 3.27 can be joined, resulting on Eq. 3.31.

$$(\phi_w^{(1)} + \phi_s^{(1)} + \phi_r^{(1)}).\bar{n} = \bar{V}^{(1)}.\bar{n} \tag{3.31}$$

Knowing that Eq. 3.31 is linear, it may be divided into two other equations associated with the radiation and diffraction problem, respectively, Eq. 3.32 and Eq. 3.33.

$$\nabla\phi_r^{(1)}.\bar{n} = \bar{V}.\bar{n} \tag{3.32}$$

$$\nabla\phi_w^{(1)}.\bar{n} = -\nabla\phi_s^{(1)}.\bar{n} \tag{3.33}$$

According to Eq. 3.32, as long as there are no incoming waves in the domain, the scattering potential will be null as well. Nevertheless, the radiation potential appears if any motion is imposed to the body; then, this potential is responsible for resisting the body motion. Further, the radiation potential is employed to obtain the hydrodynamics reactions forces which are mainly related to added mass and potential damping. Contrarily, the Eq. 3.33 establishes that the velocity associated to the diffraction potential cancels the velocity induced by the incoming wave to guarantee impenetrability.

Likewise the first-order boundary condition, the second-order potential can be decomposed in terms of the same potentials, but in the second-order components, as Eq. 3.34 shows.

$$\phi^{(2)} = \phi_w^{(2)} + \phi_s^{(2)} + \phi_r^{(2)} \tag{3.34}$$

Substituting Eq. 3.34 in Eq. 3.28, Eq. 3.35 is provided.

$$(\phi_w^{(2)} + \phi_s^{(2)} + \phi_r^{(2)}).\bar{n} = -(\bar{X}^{(1)}.\nabla).\nabla\phi^{(1)}.\bar{n} + (\bar{V}^{(1)} - \nabla\phi^{(1)}).\bar{N}^{(1)} + \bar{V}^{(2)}.\bar{n} \tag{3.35}$$

As well as the first-order potential, the second-order also may be decomposed into two equations, Eq. 3.36 and Eq. 3.37.

$$\nabla\phi_r^{(2)}.\bar{n} = \bar{V}^{(2)}.\bar{n} \tag{3.36}$$

$$(\phi_w^{(2)} + \phi_s^{(2)}).\bar{n} = -(\bar{X}^{(1)}.\nabla).\nabla\phi^{(1)}.\bar{n} + (\bar{V}^{(1)} - \nabla\phi^{(1)}).\bar{N}^{(1)} \tag{3.37}$$

The same conclusions obtained from the first-order boundary conditions worth here, but are related to the second-order terms. The second-order radiation potential arises from the body's second-order motion, thus, low frequency motions and motions at double frequency as well. Eq. 3.36 and Eq. 3.32 show that $\phi_r^{(2)}$ and $\phi_r^{(1)}$ satisfy the same boundary condition and have the same physically significance, but the first one has a smaller order of magnitude. On the other hand, Eq. 3.37 characterizes the second-order diffraction potential relation which provides the excitation of second-order hydrodynamics forces. The second-order scattering and undisturbed incoming waves potentials impose a velocity on the particles, so the velocity on the body surface corrected by the first-order motion is canceled.

3.2.5 Boundary condition at infinity

This boundary condition is the one responsible for ensuring the uniqueness of the solutions. The first and second-order scattering and radiation potential, $\phi_r^{(1)}$, $\phi_s^{(1)}$, $\phi_r^{(2)}$ and $\phi_s^{(2)}$, must propagate outward at a great distance from the body due to the radiation condition. The term $\phi_w^{(2)}$ dismisses the radiation condition used, since it depends only on the undisturbed incoming waves first-order potential $\phi_w^{(1)}$, as Eq. 3.23 shows.

3.3 Second-order forces and moments

Second-order forces and moments are obtained from the direct integration of pressure on the hull surface. Firstly, a referential coordinate system is defined in $O(x, y, z)$, as Fig. 3.4 illustrates. Hence, the force acting on the body related to $O(x, y, z)$ is given by Eq. 3.38, in which $\bar{N}$ is the instantaneous normal vector of the dS surface.

$$\bar{F} = -\iint\limits_{S} P\bar{N}dS \tag{3.38}$$

It is noteworthy that $S = S_B + S_I$, represented in Fig. 3.4 and applying the Stokes expansion of the pressure P and vector $\bar{N}$ in the Eq. 3.38, Eq. 3.39 is derived.

$$\begin{aligned}\bar{F} = &-\iint\limits_{S_B} (\varepsilon^0 P^{(0)} + \varepsilon^1 P^{(1)} + \varepsilon^2 P^{(2)})(\varepsilon^0 N^{(0)} + \varepsilon^1 N^{(1)} + \varepsilon^2 N^{(2)})dS \\ &-\iint\limits_{S_I} (\varepsilon^0 P^{(0)} + \varepsilon^1 P^{(1)} + \varepsilon^2 P^{(2)})(\varepsilon^0 N^{(0)} + \varepsilon^1 N^{(1)} + \varepsilon^2 N^{(2)})dS\end{aligned} \tag{3.39}$$

Also, Eq. 3.38 can be written in terms of the perturbation parameter as Eq. 3.40 shows.

$$\bar{F} = \varepsilon^0 \bar{F}^{(0)} + \varepsilon^1 \bar{F}^{(1)} + \varepsilon^2 \bar{F}^{(2)} + O(\varepsilon^3) \tag{3.40}$$

Each force component of Eq. 3.40 can be decomposed in terms of the P and $\bar{N}$. The variable $F^{(0)}$ represents the hydrostatic force integration over the wetted surface S_B, Eq. 3.41.

$$\bar{F}^{(0)} = -\iint\limits_{S_B} P^{(0)}\bar{N}^{(0)}dS \tag{3.41}$$

The force $F^{(1)}$ is the total first-order force which oscillates with the incoming wave frequency given by Eq. 3.42.

$$\bar{F}^{(1)} = -\iint\limits_{S_B} (P^{(0)}\bar{N}^{(1)} + P^{(1)}\bar{n})dS \tag{3.42}$$

Lastly, the second-order wave force is obtained from the integration of all the terms which contribute to the second-order over the wetted surface S_B, in addition to the integral of the first-order pressure over the oscillatory surface S_I, as Eq. 3.43 defines.

$$\bar{F}^{(2)} = -\iint\limits_{S_B} (P^{(0)}\bar{N}^{(2)} + P^{(1)}\bar{N}^{(1)} + P^{(2)}\bar{n})dS - \iint\limits_{S_I} P^{(1)}\bar{n}dS \tag{3.43}$$

Further, the hydrostatic $P^{(0)}$, the first-order $P^{(1)}$ and the second-order $P^{(2)}$ are given, respectively, by Eq. 3.44, Eq. 3.45 and Eq. 3.2. They are all computed in the mean position.

$$P^{(0)} = -\rho g z^{(0)} \tag{3.44}$$

$$P^{(1)} = -\rho g z^{(1)} - \rho\frac{\partial \phi^{(1)}}{\partial t} \tag{3.45}$$

$$P^{(2)} = -\rho g z^{(2)} - \rho\frac{\partial \phi^{(2)}}{\partial t} - \frac{1}{2}\rho|\nabla\phi^{(1)}.\nabla\phi^{(1)}| - \rho\left(X^{(1)}.\nabla\frac{\partial \phi^{(1)}}{\partial t}\right) \tag{3.46}$$

After some mathematical work, Pinkster (1980) arrives in the final equation for the total second-order wave forces which includes the wave exciting and the hydrostatic and hydrodynamic forces, Eq. 3.47.

$$
\begin{aligned}
\bar{F}^{(2)} = & -\int\limits_{WL} \frac{1}{2}\rho g(\zeta_r^{(1)})^2 \bar{n}dl + \bar{\alpha}^{(1)} \times (M.\ddot{\bar{X}}_g^{(1)}) + \\
& -\iint\limits_{SB} \left\{ -\frac{1}{2}|\nabla\phi^{(1)}|^2 - \rho\frac{\partial\phi^{(2)}}{\partial t} - \rho\left(\bar{X}^{(1)}.\nabla\frac{\partial\phi^{(1)}}{\partial t}\right)\right\}\bar{n}dS + \\
& \iint\limits_{SB} \rho g z^{(2)}\bar{n}dS + \bar{\alpha}^{(2)} \times (0,0,\rho g\nabla)
\end{aligned}
\tag{3.47}
$$

In most cases, the interest is only in the wave exciting force; then, the potential $\phi^{(2)}$ can be represented by the diffraction component $(\phi_w^{(2)} + \phi_s^{(2)})$ [1]. Also, the last term of Eq. 3.47 represents the hydrostatic reaction force and can be dismissed. Finally, the exciting force of second-order waves is shown in Eq. 3.48.

$$
\begin{aligned}
\bar{F}^{(2)} = & -\int\limits_{WL} \frac{1}{2}\rho g(\zeta_r^{(1)})^2 \bar{n}dl + \bar{\alpha}^{(1)} \times (M.\ddot{\bar{X}}_g^{(1)}) + \\
& -\iint\limits_{SB} \left\{ -\frac{1}{2}|\nabla\phi^{(1)}|^2 - \rho\frac{\partial(\phi_w^{(2)} + \phi_s^{(2)})}{\partial t} - \rho\left(\bar{X}^{(1)}.\nabla\frac{\partial\phi^{(1)}}{\partial t}\right)\right\}\bar{n}dS
\end{aligned}
\tag{3.48}
$$

The total moment in relation to the $O(x, y, z)$ coordinate system is given by Eq. 3.49.

$$
\bar{M} = -\iint\limits_{S} P(\bar{X}' \times \bar{N})dS \tag{3.49}
$$

Following the same procedure, the total second-order wave moment is defined by Eq. 3.50.

$$
\begin{aligned}
\bar{M}^{(2)} = & -\int\limits_{WL} \frac{1}{2}\rho g(\zeta_r^{(1)})^2 (\bar{X} \times \bar{n})dl + \bar{\alpha}^{(1)} \times (I.\ddot{\bar{X}}_g^{(1)}) + \\
& -\iint\limits_{SB} \left\{ -\frac{1}{2}|\nabla\phi^{(1)}|^2 - \rho\frac{\partial\phi^{(2)}}{\partial t} - \rho\left(\bar{X}^{(1)}.\nabla\frac{\partial\phi^{(1)}}{\partial t}\right)\right\}(\bar{x} \times \bar{n})dS + \\
& -\iint\limits_{SB} -\rho g z^{(2)}(\bar{x} \times \bar{n})dS
\end{aligned}
\tag{3.50}
$$

---

[1] Having no available means to numerically take the solution of the second-order Boundary Value Problem (BVP) and obtain a solution for the second-order potential, Pinkster (1980) proposed a simplification considering only the second-order potential due to the incoming waves. In this regard, it is important to note that Aranha and Pesce (1986) have proposed a more refined approximation for this force component based on the assumption of a narrow-banded wave spectrum.

After all, the second-order wave exciting moment is presented in Eq. 3.51.

$$
\begin{aligned}
\bar{M}^{(2)} = & -\int\limits_{WL} \frac{1}{2}\rho g(\zeta_r^{(1)})^2(\bar{X} \times \bar{n})dl + \bar{\alpha}^{(1)} \times (I.\ddot{\bar{X}}_g^{(1)}) + \\
& - \iint\limits_{SB} \left\{ -\frac{1}{2}|\nabla\phi^{(1)}|^2 - \rho\frac{\partial(\phi_w^{(2)} + \phi_s^{(2)})}{\partial t} - \rho\left(\bar{X}^{(1)}.\nabla\frac{\partial\phi^{(1)}}{\partial t}\right) \right\} (\bar{x} \times \bar{n})dS
\end{aligned}
\tag{3.51}
$$

3.3.1 Quadratic Transfer Function

Equations of the second-order wave forces and moments expressed as Eq. 3.48 and Eq. 3.51 are not the most suitable way for numerical computations in frequency-domain software based on the BEM. In order to simplify the problem, these non-linear forces and moments can be expressed in terms of the Quadratics Transfer Functions (QTFs), capable of representing forces in the frequency-domain in terms of a force spectrum, or in time-domain in terms of time series of these forces.

WAMIT, as stated before, is a BEM-based software as well as a numerical tool for the present thesis. This program divides the second-order forces and moments into two components, Eq. 3.52 and Eq. 3.53, in which $\bar{F}_p^{(2)}$ and $\bar{M}_p^{(2)}$ are the second-order potential terms and $\bar{F}_q^{(2)}$ and $\bar{M}_q^{(2)}$ are defined as the quadratic terms.

$$\bar{F}^{(2)} = \bar{F}_p^{(2)} + \bar{F}_q^{(2)} \tag{3.52}$$

$$\bar{M}^{(2)} = \bar{M}_p^{(2)} + \bar{M}_q^{(2)} \tag{3.53}$$

The terms $\bar{F}_p^{(2)}$ and $\bar{M}_p^{(2)}$ are obtained from the direct integration of the second-order potential on the hull, thus, calculating them requires great computational efforts due to non-homogeneous free surface condition. On the other hand, $\bar{F}_q^{(2)}$ and $\bar{M}_q^{(2)}$ are easier to compute since they only depend on the quadratic relations of the first-order terms. They arise from the pressure term in Bernoulli's equation, Eq. 3.1, and from the correction due to the mean position free surface approximation.

Thereafter, each term of the second-order force is presented along its meaning, the same idea works to the moment equations. Eq. 3.54 is the $\bar{F}_q^{(2)}$ term itself. The $\bar{F}_p^{(2)}$ is composed of the sum of Eq. 3.55, Eq. 3.56, Eq. 3.57 and Eq. 3.58.

Equation 3.54 represents the second-order potential contribution:

$$-\iint\limits_{SB} -\rho\frac{\partial(\phi_w^{(2)} + \phi_s^{(2)})}{\partial t}\bar{n}dS \tag{3.54}$$

Equation 3.55 is a force that express the first-order wave elevation over the hull surface:

$$-\int_{WL} \frac{1}{2}\rho g(\zeta_r^{(1)})^2 \bar{n} dl \tag{3.55}$$

Equation 3.56 is the quadratic term of the first-order potential:

$$\iint_{SB} \frac{1}{2}|\nabla\phi^{(1)}|^2 \bar{n} dS \tag{3.56}$$

Equation 3.57 is the product between the first-order pressure gradient and the first-order motion:

$$\iint_{SB} \rho \left(\bar{X}^{(1)}.\nabla\frac{\partial\phi^{(1)}}{\partial t}\right) \bar{n} dS \tag{3.57}$$

Equation 3.58 represents the product between the first-order angular motion and the inertial force:

$$\bar{\alpha}^{(1)} \times (M.\ddot{\bar{X}}_g^{(1)}) \tag{3.58}$$

The mathematical work from Eq. 3.55 to the QTF term itself is found in Pinkster (1980), but generally the second-order forces can be expressed as Eq. 3.59. Here, $A_{i,j}$ are the wave amplitudes, $\omega_{i,j}$ are the wave frequencies and $\varphi_{i,j}$ the phases. The term $T_{i,j}$ is the QTF modulus, which is also dependent on two frequencies, compounded by the sum of the terms in phase and off phase.

$$\bar{F}^{(2)} = \mathbb{R}\left[\sum_{i=1}^{N}\sum_{j=1}^{N} A_i^{(1)} A_j^{(1)} T_{ij} e^{i[(\omega_i-\omega_j)t+(\varphi_i-\varphi_j)]}\right] \tag{3.59}$$

QTFs are usually represented as matrices with many pairs of frequencies which have the size (ω_n x ω_n). The values of the main diagonal are, actually, the mean drift forces. The off-diagonal terms are the difference-frequency forces related terms.

3.4 Numerical Methods

At this point, the second-order forces problem complexity is inferred and understood. Specially for geometries as ships and platforms, solving such a sophisticated problem analytically is almost impossible, even considering all assumptions and simplifications that have been made. As stated before, in 1980, when Pinkster developed his thesis, there were not computers and software able to solve these types of problems. However, BEM arose some time later to figure out this issue and they are the main tool that engineers work with until nowadays. Another tool that can be used in this scenario is the Finite Volume Method (FVM) based on the Reynolds-Averaged Navier-Stokes (RANS) equations. Although, using it for second-order problems is less common due to its high computational cost.

In this thesis, of course, BEM codes were used since the main objective aims to evaluate their prediction regarding mean and slow-drift motions. In addition, a FVM software was used as a complementary tool in order to assist in the analysis.

3.4.1 Boundary Element Method (BEM)

According to Khalili et al. (2012), BEM emerged in the last four decades as a numerical tool that only needs surface discretisations. In other words, as it is stated by Egab (2020), BEM is an alternative technique that assimilates the mesh only on the boundaries of the domain, which makes it interesting for free surface problems. That is why this method has been implemented into a variety of commercial software over the years.

Basically, the method consists in finding the velocity potential through source distributions over the body surface, known as sources method, or using the Green's theorem, in which the appropriate function is the one that satisfies the free-surface boundary condition. The latter is largely popular in hydrodynamics software for the advantage of requiring only the discretisation of the fluid surface in the computational domain.

One of the most popular hydrodynamics software, which is based on BEM, is Wave Analysis MIT (WAMIT). *" The radiation and diffraction velocity potentials on the body wetted surface are determined from the solution of an integral equation obtained by the Green's theorem with the free-surface source-potential as the Green function"* (WAMIT, 2006). WAMIT is a versatile software that allows modelling one or multiple interacting bodies, on the surface or submerged, freely floating or fixed.

A variety of features, such as added-mass, damping factors, motions amplitudes, drift forces and moments and quadratic transfer functions can be evaluated in WAMIT. The panels can be discretized by either low-order or higher-order methods. The first refers to quadratic or triangular type panels and the second to B-Spline or Non-uniform Rational Basis Spline (NURBS). This software solves problems in the frequency domain, providing the main advantage of requiring lower computational time than in time-domain. Nevertheless, software in time-domain apply boundary conditions in each time step stage; so, even under some assumptions and approximations, they can handle non-linear effects better than those in frequency-domain.

AQWA also works in frequency domain, but has the advantage of having a time-domain simulator integrated in. According to Ansys (2013), this software is also able to simulate linearized hydrodynamic fluid wave loading on floating or fixed rigid bodies. In addition to the three-dimensional radiation/diffraction theory, AQWA accounts with Morison's elements feature implemented into the software.

Its code performs in a similar way as WAMIT, both provide options to compute the second-order forces by using Newman's approximation or computing the complete QTF. Nevertheless, for WAMIT performing the complete calculations of the QTF, it is possible to model a free surface mesh into the software, while AQWA considers that the second-order potential force component is too small in deep waters and no extra action is required. Except for that, both potential codes have correspondent considerations and ways to solve the forces and motions of any type of vessel in frequency-domain. It is essential to highlight that these potential codes have a substantial and grounded theory behind them, and which have been used for decades.

3.4.2 Finite Volume Method (FVM)

In this method, as the name itself states, the domain is divided into finite volumes. As Rapp (2022) states, the FVM is able to be used at any differential equation that can be written in the divergence form. According to Runchal (2009), Prof. Brian Spalding and his research group developed the engineer practice approach to CFD in the mid-70s, which is used in the majority of commercial CFD software nowadays. Prof. Brian is the creator of the Semi-Implicit Method for Pressure Linked Equations (SIMPLE) algorithm, which is a universally used numerical procedure to solve the fundamental governing equations of fluid dynamics, according to Rodi and Fueyo (2002).

For the case of second-order wave forces acting on semi-submersible platforms, the Reynolds-Averaged Navier-Stokes (RANS) turbulence model can be used. These equations are similar to the original ones, in exception that they account with Reynolds stresses terms which are additional terms that need to be modelled into momentum equations.

In compliance with Goodfellow and Wang (2021), there are a variety of models to compute these parameters, but the most common are $k\epsilon$ and $k\omega$ in their different forms. In the mentioned semi-submersible problem, $k\omega$ is an appropriate model since it achieves higher accuracy for boundary layers with separate flows. In order to save computational costs and to eliminate possible dependencies that this model may have in some regions, Menter (1993) created the $k\omega - SST$ model, which behaves as $k\omega$ close to the wall and $k\epsilon$ as the problem is moving away from it. The idea here is not to go further in the modelling and parameters details, but a precise explanation is found in Goodfellow and Wang (2021) and Wilcox et al. (1998).

Fluent from ANSYS (FLUENT, 2011) and STAR-CCM+ (CCM+, 2018) are very well known CFD commercial softwares that are used in the marine field. Both have as options the parameters and models described in the last paragraph. In this specific problem, well modelling the free surface is essential. In FVM tools, this phenomenon is captured by the Volume Of Fluid method (VOF). Katopodes (2018) states that VOF is a robust method for representing the free surface, air-water interface in this case. In this method, the phase interface is characterized by Ψ, which is the liquid volume fraction in each cell, as Fig. 3.5 presents.

Figure 3.5: The fraction of liquid volume in VOF method: (A)$\Psi = 1$, (B)$\Psi = 0$, (C)$0 < \Psi < 1$.

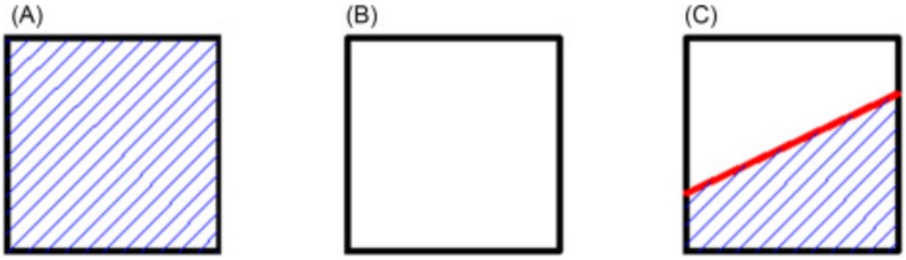

Extracted from Sun and Zhang (2020).

At least in Fluent, the waves modelling along with the VOF method are able to replicate first-order Airy waves and second to fifth-order Stokes waves. The last ones are recommended for high steepness waves, while the first one, Airy (1845), is based on the linear theory, therefore it should be used only for small steepness waves. Independently of the wave model, the inputs are only the wave height and wavelength.

In summary, regarding FVM, there are abounding CFD software options that capture, in theory, first, second, third-order wave related forces. These programs are powerful prediction tools of fluid-flow phenomena. Although they provide great ways to visualize the flow and the phenomena and have the possibility of breaking the force contributions, besides including viscous forces and non-linearities; it takes a large amount of time to develop and solve a problem, especially in these cases where waves have to be modelled.

3.5 Second-order forces approximations

The process of computing the second-order forces and moments is complex. As matter of fact, there are different versions of WAMIT just for computing the non-linear forces. Pinkster (1980) has already made a simplification by dismissing the forcing effect acting on the free surface and assuming that the majority part of the force is due to the undisturbed incoming wave potential. Other authors such as Newman (1974) developed some models capable of approximating these forces using only the mean drift forces which are easier to compute. Newman's approximation is incorporated into potential codes such as AQWA and WAMIT and will be used for the semi-submersible motions predictions in irregular waves in Chapter 5.

Newman (1974) has noticed that for horizontal plane motions with low natural frequencies, second-order forces present small variations close to the difference-frequency equals to zero. Hence, these forces can be approximated based on the mean drift forces.

The author started focusing on the slowly-varying second-order force, $f(t)$, Eq. 3.60. Here, A_m and A_n are the two wave amplitudes and ω_m and ω_n are, respectively, their frequencies. F_{mn} is the QTF which physically represents the amplitude and phase of the second-order force associated with the difference-frequency terms, due to the presence of these two waves. Actually, F_{mm} is assumed real since the imaginary part does not matter to this analysis.

$$f(t) = \mathbb{R}\left\{\sum_m \sum_n A_m A_n F_{mn} e^{i(\omega_m - \omega_n)t}\right\} \tag{3.60}$$

The slowly-varying force is related to the QTF off-diagonal elements, which are very close to the main diagonal, in other words, where the difference-frequency is very small, as Eq. 3.61 describes.

$$|\omega_m - \omega_n| << \frac{1}{2}(\omega_m + \omega_n) \tag{3.61}$$

If Eq. 3.61 is satisfied, the difference-frequency is good enough to apply the approximation shown in Eq. 3.62 with an error of the order of the difference-frequency. In fact, the following expression allows a variety of ways to express this approximation.

$$F_{mn} = F_{mm} + O(\omega_m - \omega_n) \tag{3.62}$$

The main advantage of this approximation model is that F_{mm} is the mean drift itself and depends only on the first-order solution. Therefore, the approximate slowly-varying force, $\tilde{f}(t)$ is given by Eq. 3.63 which provides an asymptotic approximation to these forces.

$$\tilde{f}(t) = Re \sum_m \sum_n A_m A_n F_{mm} e^{(\omega_m - \omega_n)t} + O(\omega_m - \omega_n) \tag{3.63}$$

Newman (1974) validated his approximation model by illustrating a numerical example of the second-order pressure field associated with an undisturbed incident wave system. He has concluded that the model can recover the time series of the second-order pressure very well at small depths; however, his model did not work well at larger depths. See Fig. 3.6 to Fig. 3.9. Fortunately, the majority of the second-order wave forces are close to the free surface region.

Figure 3.6: Second-order pressure at depth = 0.01 m.

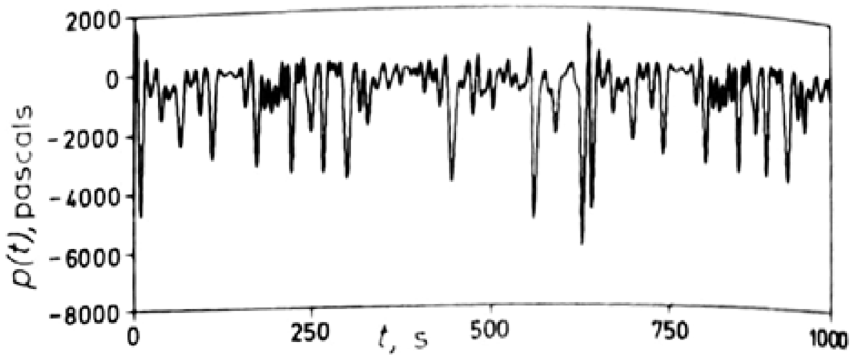

Extracted from Newman (1974).

Figure 3.7: Second-order pressure with second-order transfer functions approximated by their values on the principal diagonal at depth = 0.01 m.

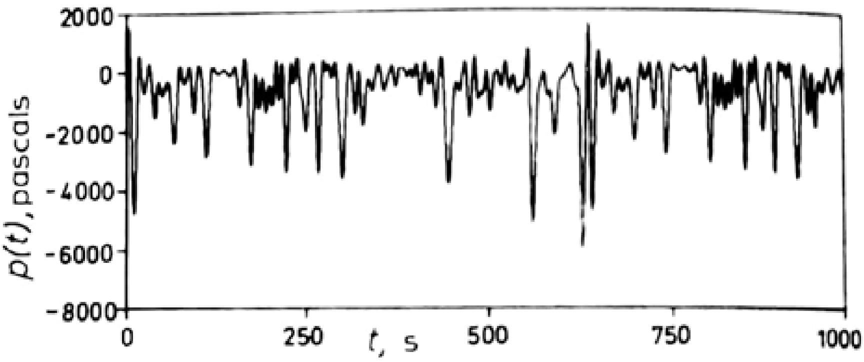

Extracted from Newman (1974).

Figure 3.8: Second-order pressure at depth = 10 m.

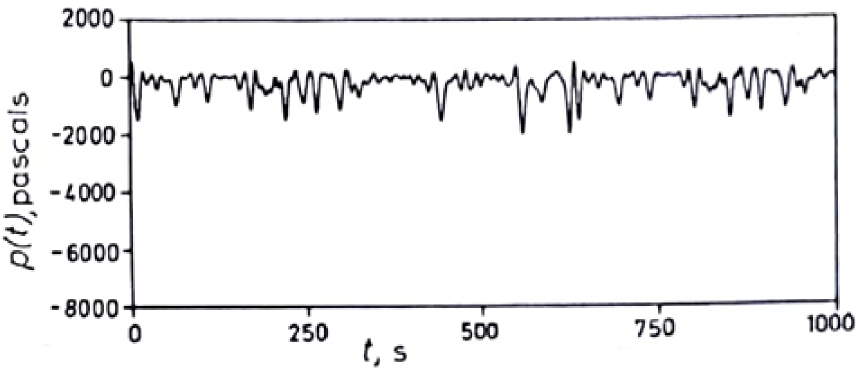

Extracted from Newman (1974).

Figure 3.9: Second-order pressure with second-order transfer functions approximated by their values on the principal diagonal at depth = 10 m.

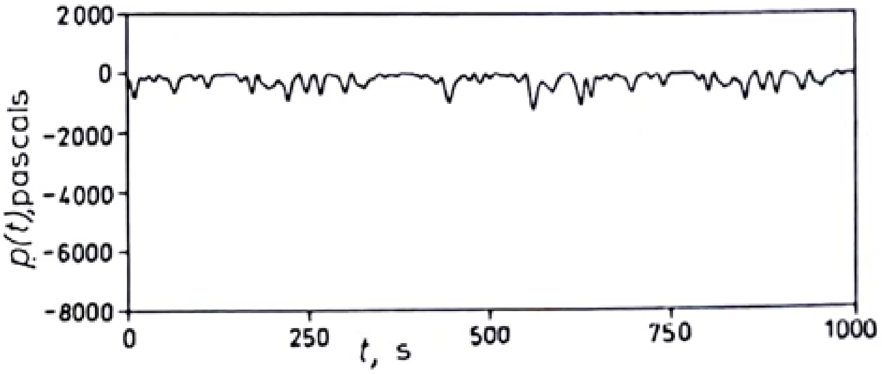

Extracted from Newman (1974).

3.6 Mean Drift Forces on a Fixed Cylinder

Slow-drift horizontal forces on semi-submersible platforms are dominated by the forces acting on the vertical columns. Therefore, from a qualitative point of view, a lot can be inferred about these forces from the solution of a fixed vertical cylinder, which has an analytical solution. Having this feature in hand, a bottom-mounted fixed cylinder problem was addressed and correlated with the semi-submersible studied in this thesis.

MacCamy and Fuchs (1954) have provided an analytical solution for the wave incident on a bottom-mounted fixed circular cylinder problem which is based on the diffraction linear theory. The main considerations, which are small steepness of the incident wave, the fluid is frictionless and the motion is irrotational, lead to the force in the x-axis on the cylinder per unit length as shown in Eq. 3.64.

$$F_z = \frac{2\rho g H}{k}\frac{coshk(d+z)}{coshkd}A(\frac{D}{L})cos(\omega t - \alpha) \tag{3.64}$$

In which L is the wavelength, d the cylinder depth, z is the vertical coordinate with origin in the free-surface level, D the cylinder diameter and:

$$tan\alpha = \frac{J_1'(\pi\frac{D}{L})}{Y_1'(\pi\frac{D}{L})}$$

J_1' and Y_1' are the Bessel Functions of first and second kind, and:

$$A(\frac{D}{L}) = \frac{1}{\sqrt{J_1'^2(\pi\frac{D}{L}) + Y_1'^2(\pi\frac{D}{L})}}$$

Hence, integrating Eq. 3.64 along its z-axis, the first-order x-component force for a fixed cylinder is obtained in time. However, Kim and Yue (1989) have developed an analytical formulation in order to obtain the mean drift forces of a cylinder of the same case.

Carmo (2021) divided the total mean drift forces into quadratic parcel of the first-order potential (incident and perturbed) and the second-order wave potential (incident and perturbed) for bottom-mounted cylinder based on Kim and Yue (1989) and Kim and Yue (1990). These equations modified for the real semi-submersible columns shape will be used in Section 5.3.2 as well.

The forces due to the incident quadratic parcel of the first-order potential is given by Eq. 3.67. In which j represents the sub index to the first wave and l to the second wave. The index I refers to the incident component and P to the perturbed one; ∇^2 is the quadratic first-order potential represention and η is the wave elevation representation. R is the cylinder radius, $\bar{h}$ is the non-dimensional depth h/R and $\bar{k}$ is the non-dimensional wave number kR. Finally, n represents the order of the functions.

$$\begin{aligned} f^-_{I,\nabla^2,jl} = \rho g R i \pi \sqrt{\frac{\bar{k}_j \bar{h}}{tanh(\bar{k}_j \bar{h})}} \sqrt{\frac{\bar{k}_l \bar{h}}{tanh(\bar{k}_l \bar{h})}} \sum_{n=0}^{\infty} \frac{J_{n+1}(\bar{k}_j) J_n(\bar{k}_l) - J_n(\bar{k}_j) J_{n+1}(\bar{k}_l)}{cosh(\bar{k}_j \bar{h}) cosh(\bar{k}_l \bar{h})} \\ \left[I^-_{jl} + I^+_{jl} \left(\frac{n(n+1)}{\bar{k}_j \bar{k}_l} + \frac{J'_{n+1}(\bar{k}_j) J'_n(\bar{k}_l) - J'_n(\bar{k}_j) J'_{n+1}(\bar{k}_l)}{J_{n+1}(\bar{k}_j) J'_n(\bar{k}_l) - J'_n(\bar{k}_j) J_{n+1}(\bar{k}_l)} \right) \right] \end{aligned} \tag{3.65}$$

$$f^-_{I,\eta,jl} = -\frac{\rho g R i \pi}{2} \sum_{n=0}^{\infty} J_{n+1}(\bar{k}_j) J_n(\bar{k}_l) - J_n(\bar{k}_j) J_{n+1}(\bar{k}_l) \tag{3.66}$$

In which the prime derivative is:

$$I^{\pm}_{jl} = \frac{1}{2} \left[\frac{sinh(\bar{k}^+_{jl} \bar{h})}{\bar{k}^+_{jl} \bar{h}} \pm \frac{sinh(\bar{k}^-_{jl} \bar{h})}{\bar{k}^-_{jl} \bar{h}} \right] \tag{3.67}$$

The total force due to the quadratic parcel of the first-order potential is given by Eq. 3.68.

$$f_{\bar{\nabla}^2,jl} = \frac{2 i \rho g R}{\pi} \sqrt{\frac{\bar{h}}{\bar{k}_j tanh(\bar{k}_j \bar{h})}} \sqrt{\frac{\bar{h}}{\bar{k}_l tanh(\bar{k}_l \bar{h})}} \sum_{n=0}^{\infty} \frac{\Omega^-_{n,jl} [I^-_{jl} + I^+_{jl} n(n+1)/(\bar{k}_j \bar{k}_l)]}{cosh(\bar{k}_j \bar{h}) cosh((\bar{k}_l \bar{h})} \tag{3.68}$$

And the total force due to the wave elevation parcel is given by Eq. 3.69.

$$f^-_{\bar{\eta},jl} = \frac{2 i \rho g R}{\pi \bar{k}_j \bar{k}_j} \sum_{n=\infty}^{\infty} \Omega_{n,jl} \tag{3.69}$$

$$\Omega^{-}_{n,jl} = \frac{1}{H'_{n+1}(\bar{k_j})H'^{*}_{n}(\bar{k_l})} - \frac{1}{H'_{n}(\bar{k_j})H'^{*}_{n+1}(\bar{k_l})}$$

The forces due to the perturbed potential are obtained from the total minus the incident components.

The forces due to the incident difference-frequency second-order wave potential is given by Eq. 3.70.

$$f^{-}_{I,\phi^{(2)},jl} = \rho g R \pi \bar{\omega}^{-}_{jl}(\bar{\gamma}_{\bar{j}l} + \bar{\gamma}^{*}_{\bar{j}l})\frac{tanh(\bar{k}_{\bar{j}l}\bar{h})}{\bar{k}_{\bar{j}l}\bar{h}}J_1(\bar{k}_{\bar{j}l}) \tag{3.70}$$

Where

$$\bar{\gamma}_{\bar{j}l} = -i\frac{(\bar{k_j}\bar{h})^2[1 - tanh^2(\bar{k_j}\bar{h})] - 2(\bar{k_j}\bar{h})(\bar{k_l}\bar{h})[1 + tanh(\bar{k_j}\bar{h})tanh(\bar{k_l}\bar{h})]}{2\sqrt{\bar{k_j}\bar{h}tanh(\bar{k_j}\bar{h})}[\bar{\omega}^{2}_{jl}{}^{-} - \bar{k}^{-}_{jl}\bar{h}tanh(\bar{k}_{\bar{j}l}\bar{h})]}$$

Finally, the forces due to the perturbed second-order wave potential is given by Eq. 3.71.

$$\begin{aligned} f^{-}_{P,\phi^{(2)},jl} = -\rho g R \pi \bar{\omega}^{-}_{jl}(\bar{\gamma}_{\bar{j}l} + \bar{\gamma}^{*}_{\bar{j}l})\frac{\bar{k}_{\bar{j}l}\bar{h}}{cosh(\bar{k}_{\bar{j}l}\bar{h})}J_1(\bar{k}_{jl})\Bigg[B_{0,jl}\Pi_{0,jl}\frac{H_1(v_{0,jl})}{v_{0,jl}H'_1(v_{0,jl})} + \\ \sum_{n=1}^{\infty} B_{n,jl}\Pi_{n,jl}\frac{K_1(k_{n,jl})}{k_{n,jl}K'_1(k_{n,jl})} \end{aligned} \tag{3.71}$$

In which:

$$\Pi_{n,jl} = \frac{1}{2}\left[\frac{sinh(\bar{k}_{\bar{j}l}\bar{h} + v_{n,jl})}{\bar{k}_{\bar{j}l}\bar{h} + v_{n,jl}} + \frac{sinh(\bar{k}_{\bar{j}l}\bar{h} - v_{n,jl})}{\bar{k}_{\bar{j}l}\bar{h} - v_{n,jl}}\right]$$

$$B_{n,jl} = \frac{4sinh(v_{n,jl})}{2v_{n,jl} + sinh(2v_{n,jl})}$$

And, with *vo* working like a wave number, but associated with the difference frequency,

$$v_{n,jl} = \frac{\bar{\omega}^{2}_{jl}{}^{-}}{tanh(v_{o,jl})} \qquad for \qquad n = 0$$

Or,

$$v_{n,jl} = ik_{n,jl} \qquad for \qquad n \neq 0$$

With,

$$\bar{\omega}_{jl}^{2\,-} = -k_{n,jl}tank_{n,jl}, \left(n - \frac{1}{2}\right)\pi \leq k_n \leq n\pi$$

These equations can be used in order to evaluate the influence of each parcel on a cylinder of the same sectional area than one column of platform used as object of study of the present thesis. Indeed it was necessary to consider one column of the semi-submersible platform as a bottom-mounted fixed cylinder. The cylinder radius, R = 10m, represents a circumference area with a similar cross-sectional area of the semi-submersible's column. The height of the columns of the semi-submersible platform in question is 27.5 m, so, for this problem a cylinder of at least of this height was selected. However, in order to get a sensibility of how much the forces vary with the water depth, a cylinder of 100 m was chosen. The forces along the cylinder depth, which is divided at each 1m, can be defined, Fig. 3.10.

Figure 3.10: Representation of a cylinder of same sectional area of one column.

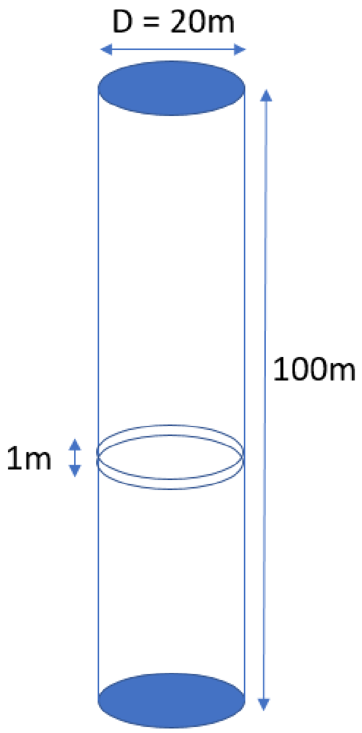

This case study was performed with regular 1 m amplitude waves and five periods: 7, 8, 9, 10 and 11 seconds. The main goal here is to measure the sensibility of each parcel of the mean drift wave forces acting on this structure. Tab. 3.1 shows the results of:

- f_{I,∇^2}: Force due to the quadratic first-order potential (Incident parcel);
- f_{P,∇^2}: Force due to the quadratic first-order potential (Perturbed parcel);

- $f_{I,\eta}$: Force due to the wave elevation (Incident parcel) and
- $f_{P,\eta}$: Force due to the wave elevation (Perturbed parcel).

Table 3.1: Force components contribution to the mean drift forces acting in a bottom-mounted fixed cylinder.

T(s)	$f_{I,\nabla^2(N)}$	$f_{P,\nabla^2}(N)$	$f_{I,\eta}(N)$	$f_{P,\eta}(N)$
7	0.00	-3.11e+04	0.00	9.34e+04
8	0.00	-2.27e+04	0.00	6.79e+04
9	0.00	-1.48e+04	0.00	4.31e+04
10	0.00	-9.25e+03	0.00	2.62e+04
11	0.00	-5.83e+03	0.00	1.59e+04

The first point to be observed is that both incident parcels are null to the mean drift contribution for one cylinder due to the symmetry that is found in the pressure field of the incident wave in relation to $(x, y) = (0, 0)$. Also, from the results it is possible to notice that the dominant part of the mean drift forces is derived from the wave elevation (perturbed parcel). This means that the majority of the force is related to the free-surface region. In addition, Fig. 3.11 gives the quadratic first-order force acting on each 1 m section of the cylinder along its depth for each period. From these results, it can be confirmed that the free-surface region dominates the forces by a large difference as the depth decreases. Just for comparison purposes, it is important to mention that at the draft of 27.5 m, little mean drift forces are acting on the cylinders.

Figure 3.11: Mean drift forces acting along the cylinder depth.

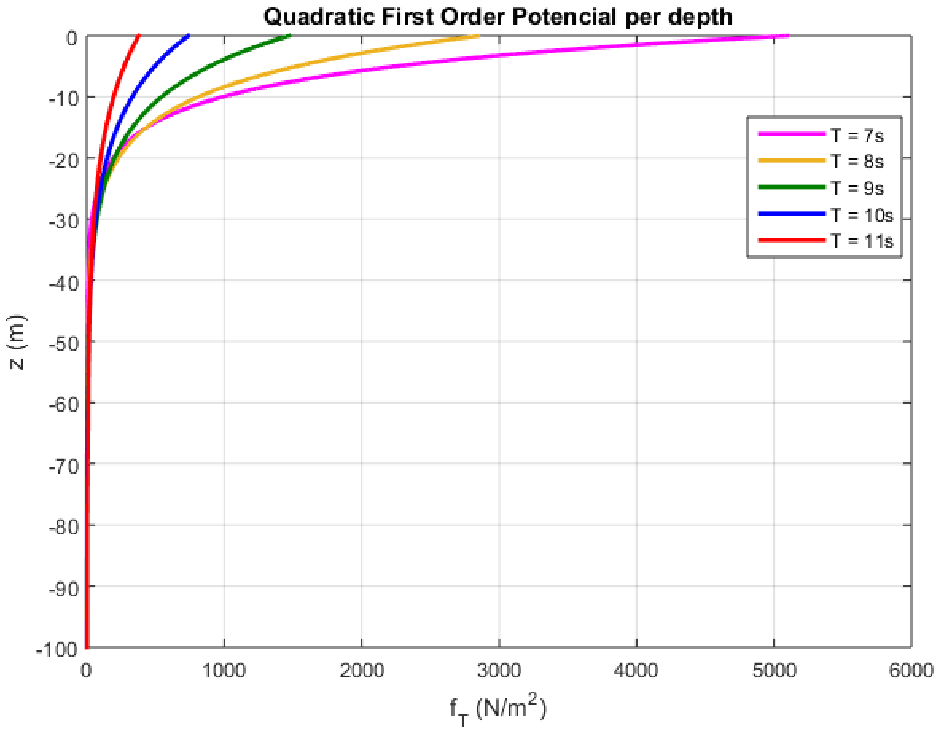

In order to contribute to this mean drift forces sensitivity analysis, and also, to assist in the validation of BEM and FVM simulations, the same cases were run into AQWA and Fluent. Details about their set-up will be given in Chapter 4. Figure 3.12 and 3.13 present the graphic representation results from BEM and Fluent compared to AQWA, respectively, for a period of 10 s.

Figure 3.12: Wave elevation around a bottom-mounted fixed cylinder in AQWA for an unitary amplitude wave.

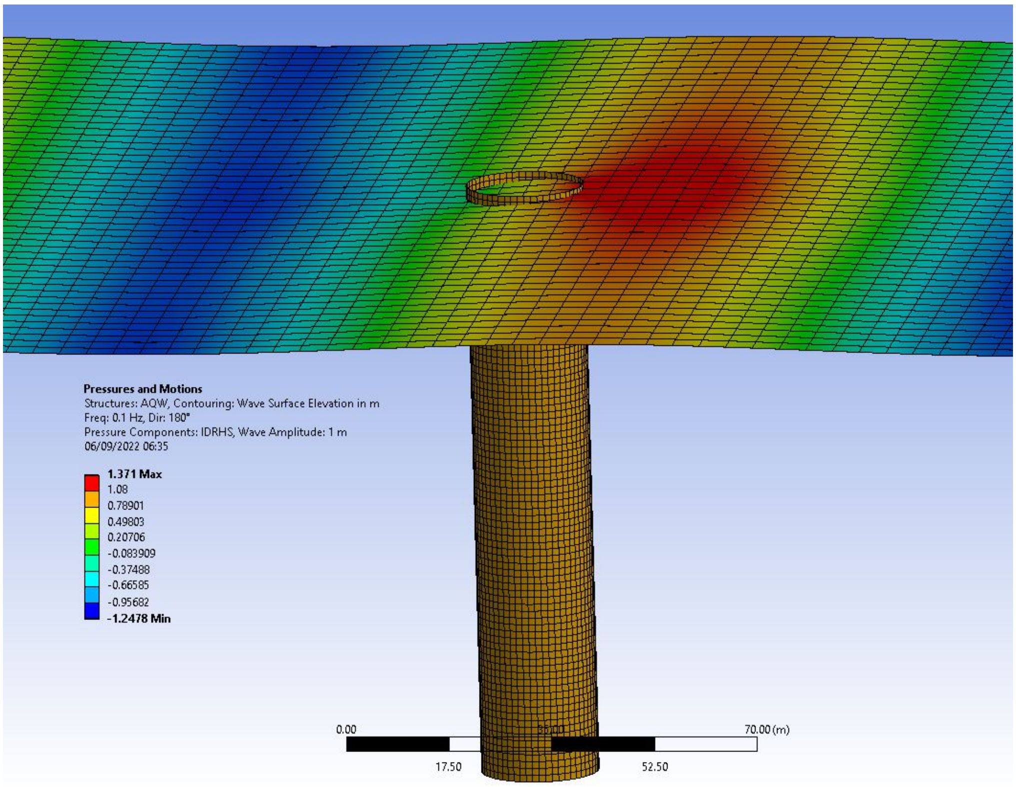

Figure 3.13: Wave elevation around a bottom-mounted fixed cylinder in Fluent and AQWA for an unitary amplitude wave.

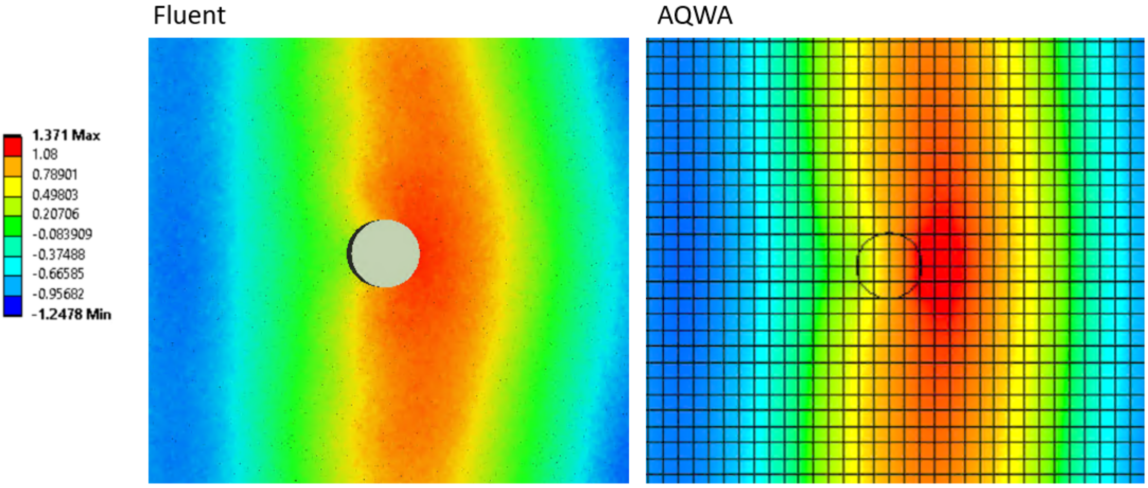

Figure 3.14 shows that the total forces acting on the cylinder by the three different methods have very similar results for all the periods evaluated. The viscous part of the force acting on the cylinders computed by Fluent was insignificant at all periods.

Figure 3.14: Comparison of total forces in a bottom-mounted fixed cylinder obtained from MacCamy and Fuchs (1954), AQWA and Fluent.

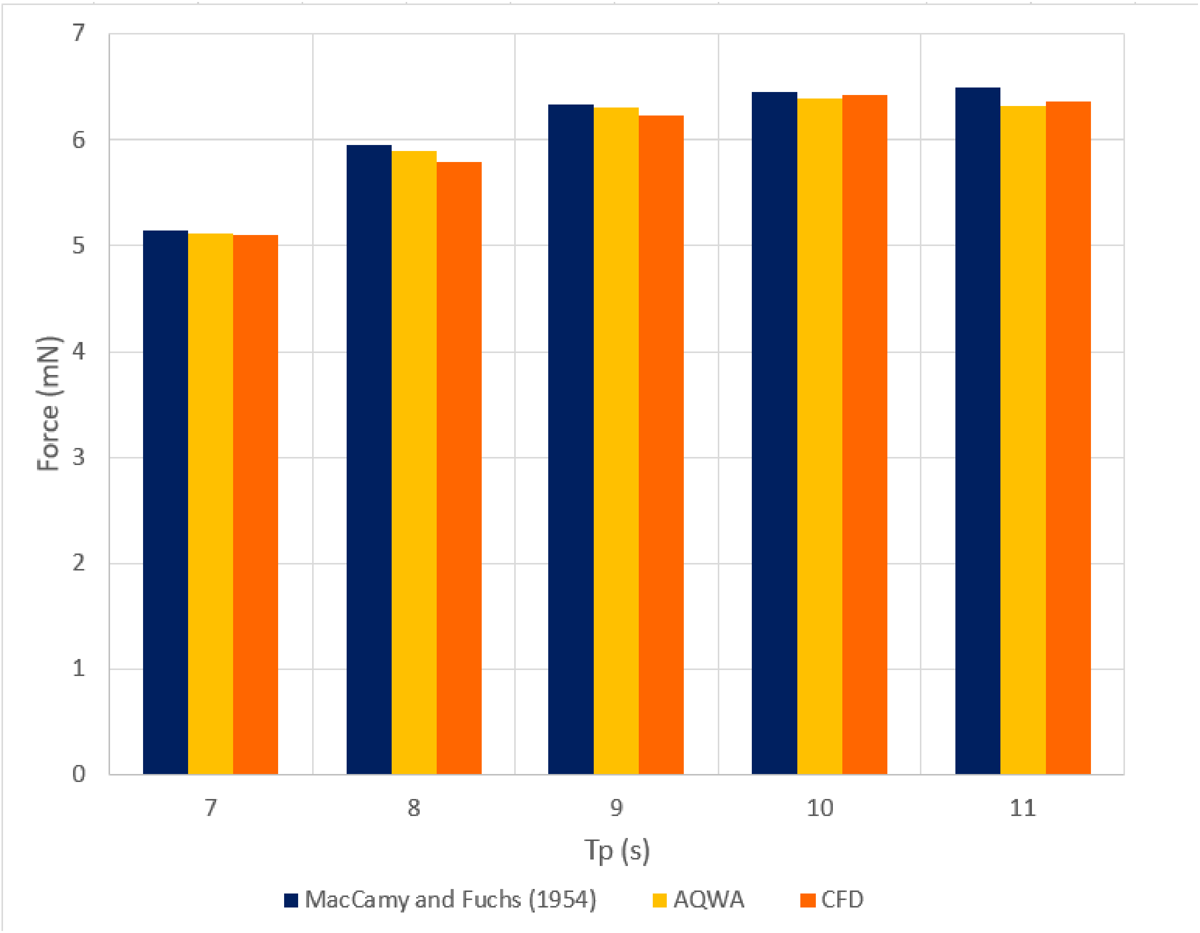

Similar results also can be found for the mean drift forces considering analytical, BEM and FVM, Fig. 3.15, no outlier results were obtained. Hence, it is possible to conclude that both AQWA and Fluent numerical models were designed appropriately, leading to a good reproduction of the exact analytical solution.

Figure 3.15: Comparison of mean drift forces in a bottom-mounted fixed cylinder obtained from Kim and Yue (1989), AQWA and Fluent.

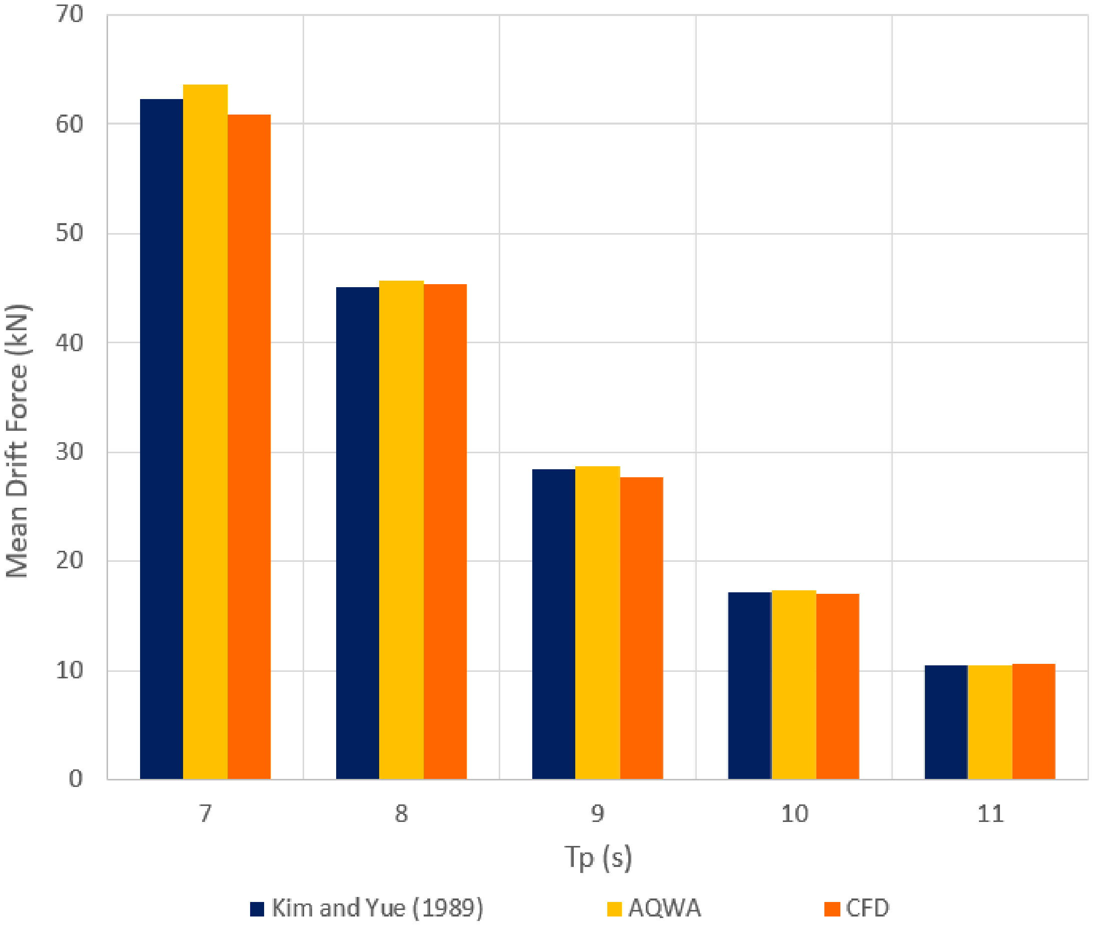

3.7 Viscous damping prediction

Due to the slow-drift being a resonant motion, the prediction of the viscous damping of surge, sway and yaw is always a critical question. In agreement with Nossen, Grue and Palm (1991), the external linearized damping is related to the slow-drift oscillations which is basically composed of skin friction, viscous pressure forces and wave drift damping. Authors as Clauss, Lehmann and Östergaard (2014) have shown that semi-submersible type platforms present damping coefficients dominated mainly by viscous effects which arise from the flow separation due the pontoon and columns. For the present study, the viscous damping will be derived from two different methods: Decay tests experimental results and Morison's elements implemented into AQWA. In Fluent, the RANS method is used, therefore, the viscous damping is already included.

One manner to estimate the viscous damping in surge, sway and yaw is using the decay tests results with the response amplitude of each degree of freedom which has to be known. In other words, for motion prediction purposes without experimental tests this method cannot be used since the user needs to know the real motion response of the vessel at a specific sea state. Another questionable definition regarding obtaining the viscous damping through decay tests is which motions amplitude to use: e.g. would it be the mean, the maximum or the significant amplitude? In this case, the significant amplitude response was used as the input parameter.

Even if having all this information in hands, getting the viscous damping by the decay tests is not a precise procedure since this type of test does not achieve the steady-state, does not take the incident wave into account and does not capture the vortex emissions precisely.

On the other hand, Morison et al. (1950) procedure, based on the slender-body theory, takes the entire flow into consideration. Morison et al. (1950) developed an equation to compute the forces acting towards a circular section vertical pile exposed to waves. Since their original problem involved high KC number, the main idea was to overlap the effects of the inertial force of the waves and viscous force and apply it to each column section. Here, the long-waves regime hypothesis is assumed.

Considering a free-floating vertical cylinder with diameter D at a z depth under sea, where a regular wave with an amplitude A and frequency ω is traveling, the Morison's equation provides the sectional heave force, Eq. 3.72. In which S is the cross sectional cylinder area, C_M is the inertia coefficient and C_D is the drag coefficient of the section, w is the flow velocity and $\dot{w}$ is the flow acceleration in heave direction.

$$f_3(t) = \rho S[C_M + 1]\dot{w}(t) + \frac{1}{2}\rho D C_D w(t)|w(t)| \tag{3.72}$$

The Morison's equation is composed of a linear inertial term and a non-linear drag term, with a 90^o lag between them. The coefficients C_M and C_D can be estimated from the Keulegan and Carpenter (1958) paper, which have been obtained experimentally for many cylinders types under an oscillatory flow, Eq. 3.73.

$$KC = \frac{VT}{D} \tag{3.73}$$

Herein, V is the flow velocity amplitude which, for flows induced by harmonic waves, is given by Eq. 3.74.

$$V = \omega A e^{kz} \tag{3.74}$$

Therefore, basically, the potential code AQWA requires the definition of Morison's elements that represents the columns and pontoons regions of a semi-submersible platform, for example, as well as, respectively C_D for assumed constant for each section. In this way, the software considers the viscous damping based on the Morison's equation at each time-step in the time-domain simulations for each degree of freedom.

4 Case of study: Four-column Large Displacement Semi-Submersible Platform

Aiming at evaluating the challenges and possible discrepancies on the numerical estimation of the second-order forces and slow-drift motions, fundamental wave tests at the TPN were planned, performed and used as a matter of comparison. The basin consists of a 14x14 m and 4.15 m deep tank with wavemakers (which also can absorb incoming wave) surrounding it.

The model chosen for performing the wave tests is a large displacement semi-submersible type platform composed of four columns with blisters and four pontoons in a 1:100 scale and without some appendix and deck features. An image of the model can be seen in Fig. 4.1 and its main dimensions in full and model scale in Tab. 4.1. Four fairleads are positioned at 20.2 m height (full scale) above the base line at the outboard center of each column.

Figure 4.1: Semi-submersible scaled model 1:100.

Table 4.1: Semi-submersible main dimensions.

Item	Full Scale	Unity	Model Scale	Unity
Length	85.00	m	0.85	m
Beam	85.00	m	0.85	m
Pontoons Height	12.00	m	0.12	m
Pontoons Width	17.50	m	0.175	m
Column Length	17.50	m	0.175	m
Column Width	17.50	m	0.175	m
Deck Height	54.00	m	0.54	m
Draft	27.50	m	0.275	m
Displacement	79856.40	ton	79.86	kg
Blister Length	11.25	m	0.112	m
Blister Width	3.50	m	0.035	m

The vertical, longitudinal and transverse positions of the center of gravity, (VCG), (LCG) and (TCG) of the model without any ballast were measured through experimental tests based on forces and moments equilibrium. Afterwards, the model was ballasted to achieve the desired draft and in order to zero LCG and TCG values and set VCG to the designed value. The inertial moments of roll, pitch and yaw were obtained from bifilar tests and are shown in Tab. 4.2. A good calibration of the loading condition is essential to well represent the seakeeping of the platform.

Table 4.2: Ballasted hull centers of gravity and moments of inertia in full scale.

Item	Value	Unity
VCG	25.29	m
LCG	0	m
TCG	0	m
I_{xx}	9.90E+07	t.m^2
I_{yy}	10.90E+07	t.m^2
I_{zz}	10.30E+07	t.m^2

For this loading condition, the natural periods of heave, roll and pitch are introduced in Tab. 4.3. Here it is important to mention that roll and pitch natural periods are considerably high and away above from the typical range of the seas. This is a fundamental and good information since the influence of the viscous damping in these degrees of freedom for the present analyses are minimal, thus the system is more sensitive only to the heave motion. It is due to these high natural periods that previous studies, such as Matos (2009), were focused on the slow vertical motions of this platform.

Table 4.3: Natural periods of heave, roll and pitch with the model moored (values in full scale). Surge, sway and yaw are in agreement with the mooring system selected.

Item	Tn	Unity
Surge	205.00	s
Sway	224.00	s
Heave	23.41	s
Roll	37.83	s
Pitch	35.23	s
Yaw	121.00	s

In the following sections, the numerical modelling and experimental tests will be presented. The model tests campaign was composed of fixed tests for measuring the first and second-order forces directly, and moored model tests for measuring motions directly. The last one was divided into regular wave groups with an horizontal mooring; and irregular waves with a catenary mooring in order to provide a more realistic set-up. The numerical analysis were split into BEM and FVM modelling.

4.1 Experimental tests

With regard to the experimental tests, performing only one type of experiment would not provide detailed and well isolated data to understand the problem. Therefore, this section approaches the three tests set-up necessary to surround possible numerical issues: captive tests and moored model tests with horizontal soft mooring and with catenary mooring lines treated separately. Each case of the first experiments were performed twice, i.e., with repetitions. All of them were performed at head waves (180^o) and some complementary cases were also performed at 157.5^o heading. Hence, surge degree of freedom can be on focus and well evaluated.

The choice of the surge natural period of the system is crucial during the experiment's design stage. This value is essential to define the waves periods and amplitudes, besides to calculate and design the mooring system. The last one had to be defined with regard to fit the objectives of performing large motions amplitudes with the purpose that significant responses can be achieved and without exceeding 250 seconds of natural periods, so that a reasonable number of slow-drift cycles could be captured. In addition, horizontal and catenary mooring systems had to be designed in a dependency of each other, since they have to provide similar horizontal stiffness to the system. The surge natural period achieved and used as a target for the waves selection was 205 s, which will be explained in detail in Sec. 4.1.2.

4.1.1 Captive tests

The main objective here was to measure the mean and difference frequency wave forces for comparing them to those computed by diffraction/radiation code. A major advantage of this test is that the second-order forces can be measured directly and compared to the QTFs without involving uncertainties, such as the damping. Another favorable point is that steady-states are easier to reach; however, as a down side of the test configuration, the influence of the first-order motions on the slow-drift forces is not captured.

By all means, obtaining these forces is not simple since they could be so small that the load cell would not be able to capture them. That is why the wave amplitudes chosen were not smaller than A = 1.0 m. The amplitude values selected were actually previously estimated by the potential code to help in the designing of the experiment. Basically, the load cell records the wave forces time series, then using a FFT routine, the force amplitudes at the low and at high frequencies are obtained.

As the name itself states, the model was rigidly fixed to the bridge of the TPN wave basin in order to provide a natural frequency to the system that is distant from those of all degrees of freedom obtained in the waves tests. Attached to the model deck, there was a load cell which was capable of measuring the wave forces acting on the fixed model. Figure 4.2 illustrates the set-up used to fix the model, which resulted in a natural frequency of the entire system (bridge, model and brackets) of 6 Hz.

Figure 4.2: Set of the model fixed at the bridge.

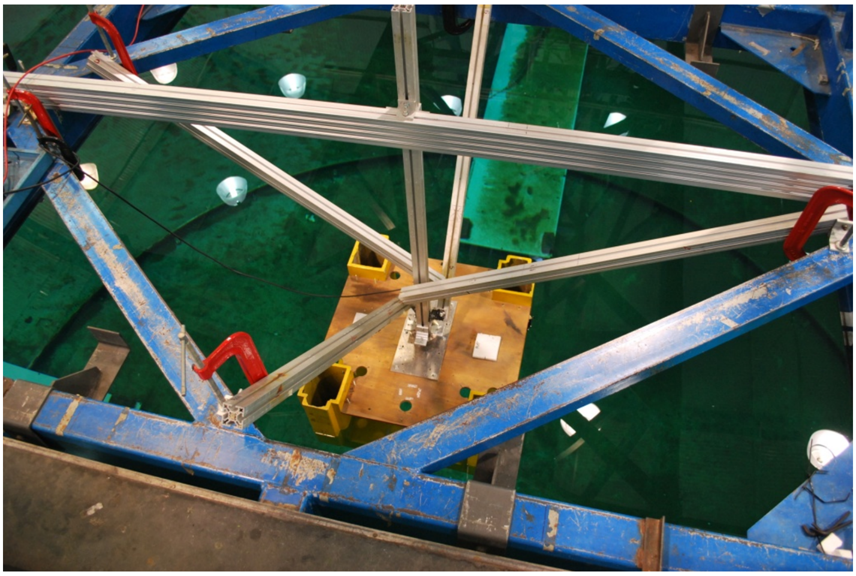

Besides the load measurements, the wave elevation was measured by four wave probes placed in the inner region of the platform closer to the columns for comparison purposes, see Fig. 4.3. The four points were selected taking care not to place them too close to the columns (1.5 m distant from the columns in full scale), in order to avoid a massive influence of wave run-up effects. In general, panel methods codes are used to present issues on the convergence of points too close to the walls.

Figure 4.3: Positions of the four wave probes during the model tests.

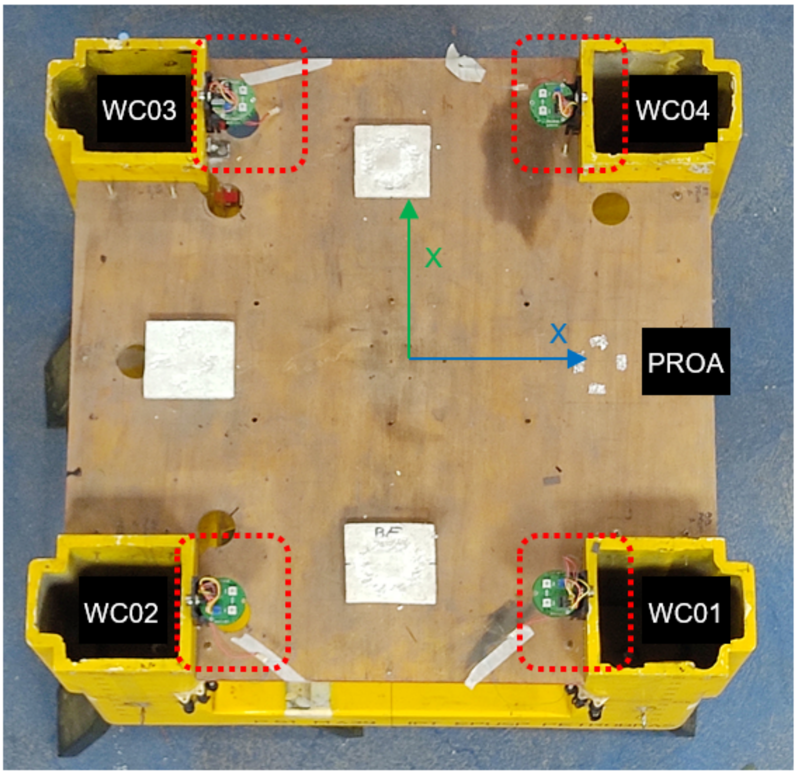

Five regular waves and five bichromatic waves (or regular groups) were tested in this configuration, all of them incoming from a direction of 180^o as Tab. 4.4 and Tab. 4.5 presents. The periods and wave heights chosen were within the typical range of the sea. For the regular waves, their steepness has a large variance between each other due to the periods, but even the largest steepness is still small. Regarding the bichromatic waves, the wave amplitudes of the first two waves were reduced in order to keep the steepness in a small value.

Table 4.4: Regular wave data in prototype scale for the fixed tests.

ID	T (s)	H (m)	Steepness (%)
REG01	7.00	2.0	1.30
REG02	8.00	2.0	1.01
REG03	9.00	2.0	0.79
REG04	10.00	2.0	0.64
REG05	11.00	2.0	0.53

Table 4.5: Bichromatic wave data in prototype scale for the fixed tests.

ID	$T_1(s)$	$T_2(s)$	$A_1/A_2(m)$	Steepness (%)
BIC01	7.00	7.245	1.2	1.52
BIC02	8.00	8.322	1.5	1.44
BIC03	9.00	9.409	2.0	1.51
BIC04	10.00	10.508	2.0	1.22
BIC05	11.00	11.618	2.0	1.00

Figure 4.4 presents a view of one regular wave test, that was conducted after all the waves had been calibrated without the model placed in the basin. After the FFT treatments of the signals, it was expected that the peaks of forces would appear at the frequencies of the two waves and at 0.0049 Hz which corresponds to the difference-frequency of surge, 205 seconds in period terms in full scale, beside of course the energy in the $zero$, 2ω and $\omega_1 + \omega_2$.

Figure 4.4: Fixed tests in waves.

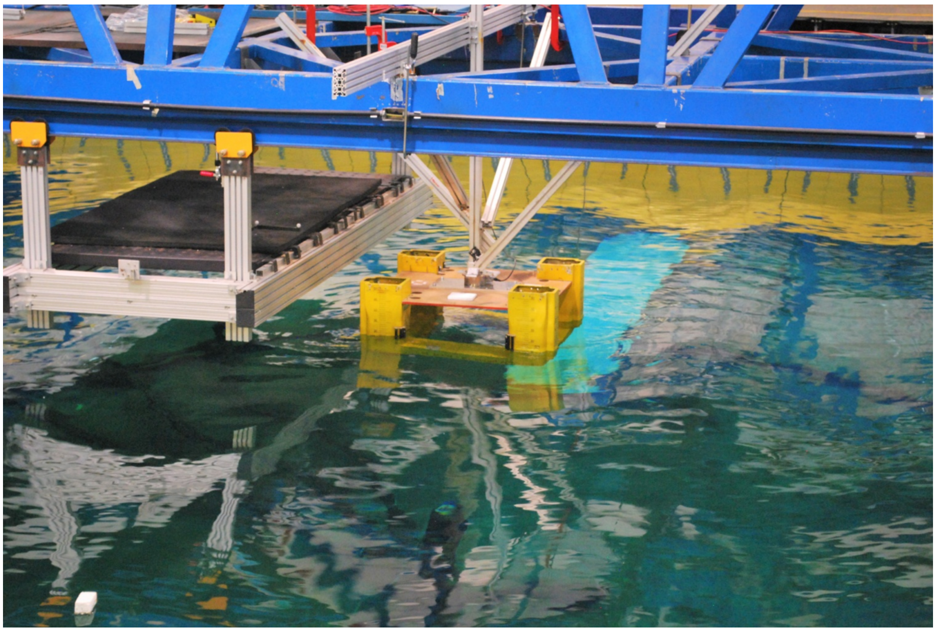

Figure 4.5 shows the FFT plot of the time force series of the BIC04 test in which it is possible to observe the peaks at the high and low frequencies exactly as they are supposed to be.

Figure 4.5: FFT amplitude forces of BIC04 wave.

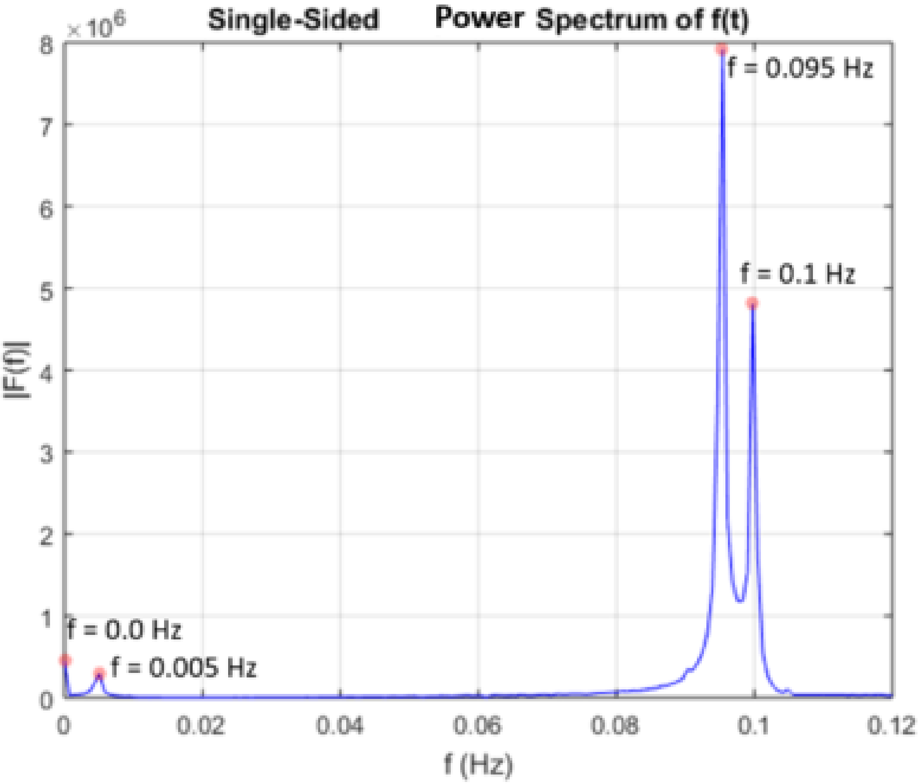

4.1.2 Moored model tests

In addition to the captive tests, tests with the platform free to move with both horizontal mooring and catenary lines were performed. Essentially, four wave probes, placed in the same place as the captive tests, were used for calibrating and measuring the waves, four Qualysis cameras for tracking the targets attached to the model and two video cameras for recording all the tests. The five Qualysis targets were placed on the semi-submersible deck as illustrated in Fig. 4.6.

Figure 4.6: Ballasted platform on water with the five Qualysis targets.

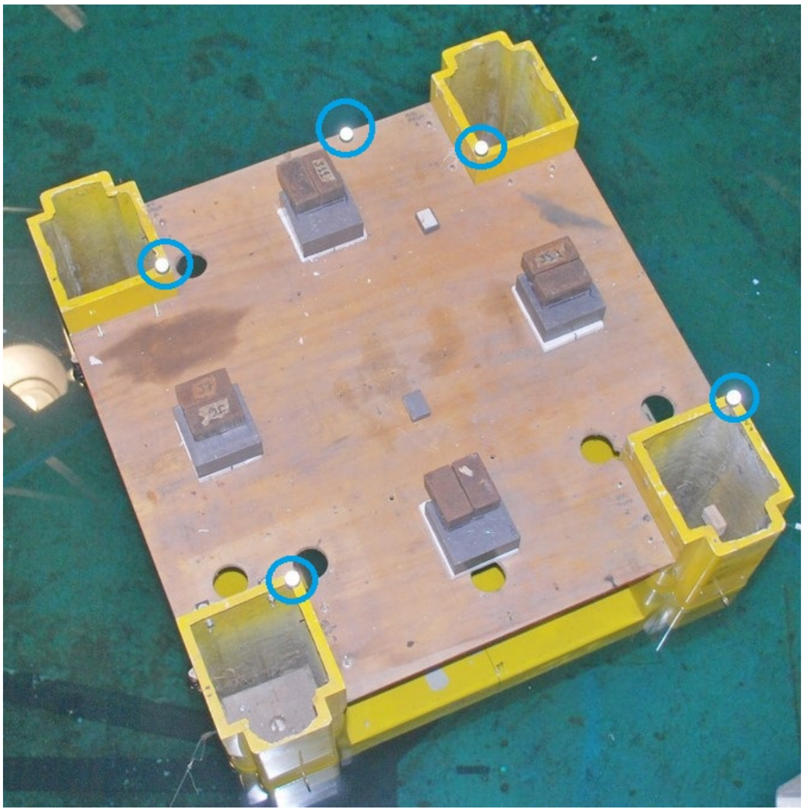

With the model in water and without any restriction feature at first moment, some pre-tests such as decay of heave, roll and pitch have been performed and their natural periods were compared to AQWA results to ensure that the inertia and the mass distribution were correct, as it is detailed in Appendix A.

4.1.2.1 Horizontal Mooring

A soft horizontal mooring system, composed of four lines and four springs, was incorporated to the platform model, as Fig. 4.7 shows. This type of system was used to avoid at maximum the interference of the mooring in the vertical motions of the platform.

Figure 4.7: Mooring arrangement.

For the 180^o heading, the fairleads are positioned on the corners of the columns at the VCG height at the platform in order to reduce its influence on the vertical motions. Figure 4.8 introduces the horizontal mooring set-up sketch.

Figure 4.8: Horizontal mooring set-up sketch in model scale.

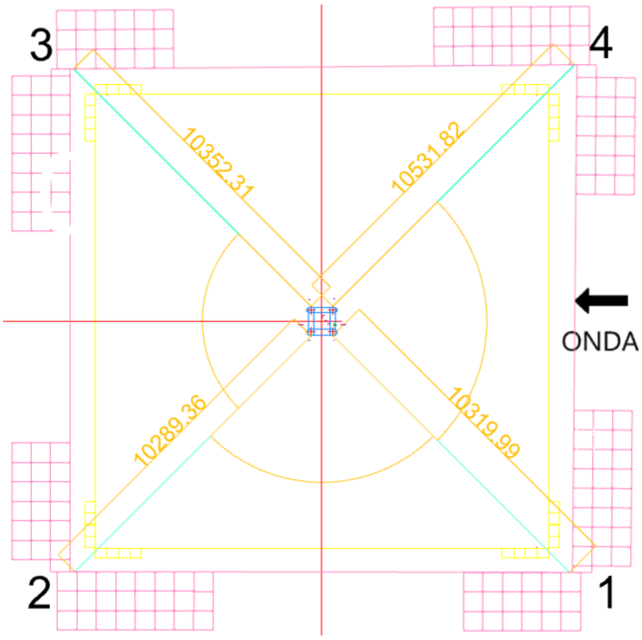

Table 4.6 presents the springs' main characteristics, which were selected to provide a surge natural period around of 205s. For this type of mooring system, the attainment of the springs stiffness to the system is direct, however, the procedure for catenary lines calculation is much more complex. Therefore, the springs' selection were carried out along with the catenary computation, in order to develop a soft system that is possible to be replicated by the second system with the tools and equipment available in the basin.

By the time that the system had been moored, pull-out, inclination and decay tests were also performed in order to ensure that the natural period the platform in all degrees of freedom as well as the stiffness of the system are in agreement with the designed values. The pre-tests description and results are presented in Appendix A.

Table 4.6: Springs main characteristics in full scale.

Location	Spring ID (s)	K (kN/m)	Unformed Length (m)	EA (kN)
FWD	M1	60.8	24.5	1489.60
FWD	M2	60.9	24.5	1492.05
AFT	M3	58.7	20.8	1220.96
AFT	M4	60.1	20.7	1244.07

The same set of regular and bichromatic waves defined for the captive model tests was used in the moored tests (see Tab. 4.5 and 4.4), in order to have enough data to evaluate the first and second-order forces acting on the platform, besides the first-order, mean and drift motions related to them.

4.1.2.2 Catenary Mooring

Further tests with a mooring system with a shape more similar to a real configuration were performed with real sea states (irregular waves) in order to do a sensibility analysis of how substantial the resultant effects of the second-order forces are similar between regular waves groups and real sea states. In addition, having two different mooring systems is a good feature to evaluate if the numerical modeling of the mooring could be a source of error.

The mooring lines configuration was designed into Dynasim, a dynamic simulator jointly developed by USP and Petrobras. WAMIT has provided the added mass, potential damping coefficients, RAOs and the mean drifts for all degrees of freedoms which are the input to Dynasim simulator. This procedure can be done analytically by Pesce, Amaral and Franzini (2018).

Into the second software, the mooring system was computed in accordance with the objective of having natural periods between 200 and 250 s and along with the horizontal mooring system selection, as stated before. In essence, this system is composed of four lines, each one with two different linear weight cables. Figure 4.9 shows the five parameters (left) of the mooring system that can be modified in order to achieve the two goals (right).

Figure 4.9: Five variables of the mooring system and the two objectives.

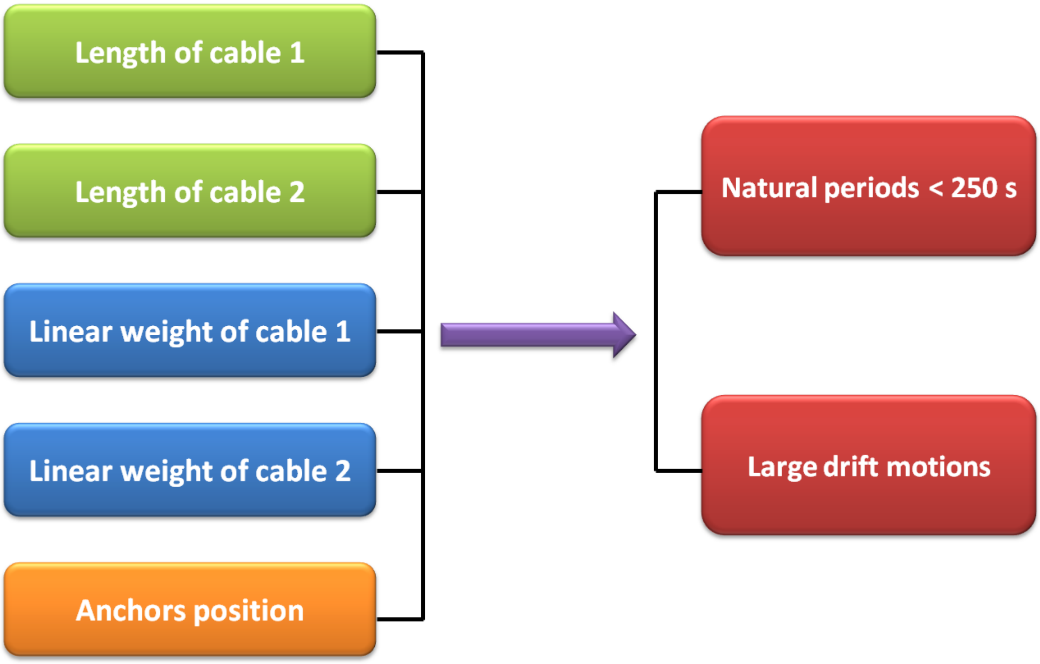

After many configuration evaluations, the one that has better fit the targets is depicted in Fig. 4.10 and Tab. 4.7. The distance between the anchor (green point) and the Touch-Down Point (TDP) (red point) in Fig. 4.10 is 163 m in full scale, large enough to avoid vertical loads in the anchor while the platform is drifting. Figure 4.11 presents the model tests set-up for the same heading.

Figure 4.10: Semi-submersible numerical model.

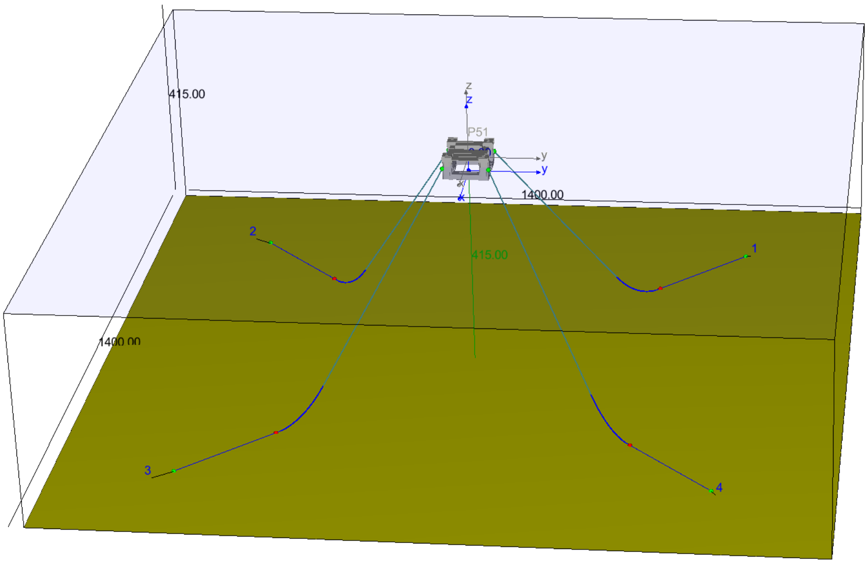

Figure 4.11: 180^o heading mooring system set-up.

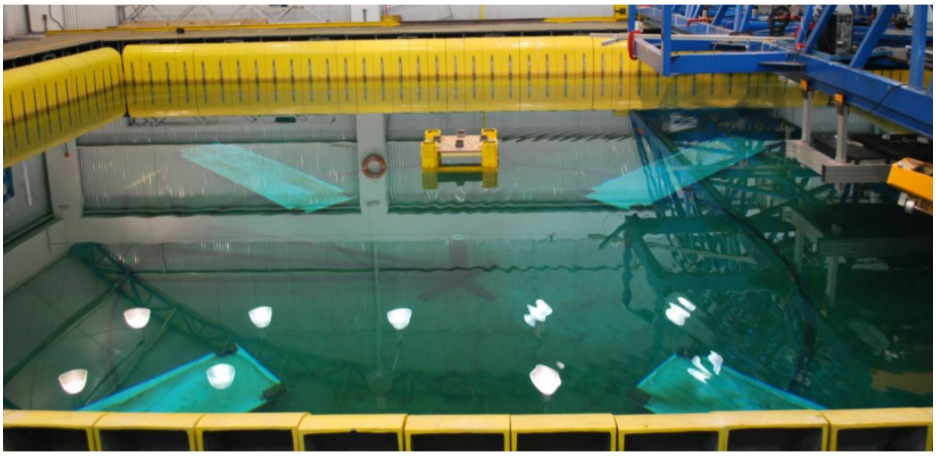

Table 4.7: Mooring system main parameters in model and full scale.

Item	Model Scale	Unity	Full Scale	Unity
Length of the cable attached to the anchor	3.48	m	348.00	m
Length of the cable attached to the fairlead	4.43	m	443.00	m
Weight of the cable attached to the anchor	178.00	g/m	17.50	kN/m
Weight of the cable attached to the fairlead	1.00	g/m	0.10	kN/m
Mooring radius	6.19	m	618.72	m
Surge natural period	20.56	s	205.60	s

Figure 4.12 exemplifies the described set-up for the 180^o wave heading in which the mooring lines are positioned at the diagonals of the platform. The yellow square represents the wave tank, the four gray plates are the anchor supports and the red lines are the cables moored on the end of the plates. The anchors supports were needed for overcoming a hindrance in the bottom of the tank, in that way the exact vertical distance between the anchor and the free surface level was 4 m in model scale (see Fig. 4.13).

Figure 4.12: 180^o catenary mooring set-up sketch.

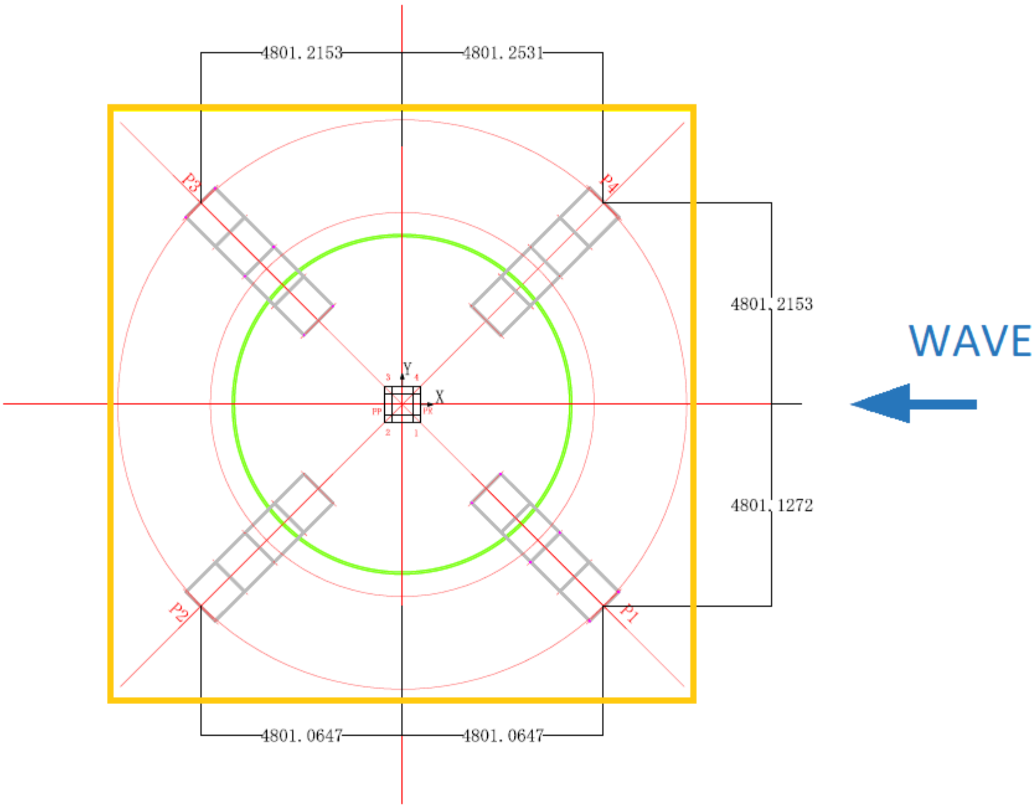

Further, a photo under the water was shot aiming at capturing one of the lines lying down anchor support, Fig. 4.13. Knowing the plate's dimension, it was possible to visually estimate the TDP distance from the anchor. The value estimated was around 1.70 meters at model scale, very close to the one numerically defined.

Figure 4.13: Catenary line under the water.

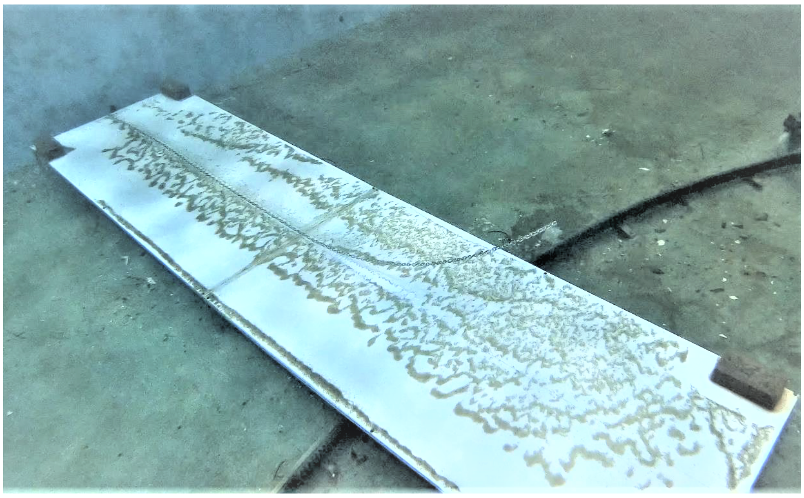

After checking the entire system, sea states with wave peak periods varying from 8 to 12 seconds were defined, with more than one significant wave height for each peak period. Each sea was executed with a different aleatory seed for a duration equivalent to three hours at full scale. At the end of the wave generation, the acquisition system remained turned on for one hour more at full-scale, in order to provide records that support the evaluation of the system natural periods and damping at the end of each run. Table 4.8 shows the main characteristics of the irregular waves.

Table 4.8: Irregular wave data in prototype scale.

ID	$T_p(s)$	$H_s(m)$	Steepness (%)	Duration (s)
IRR01	8.0	1.00	1.00	10800
IRR02	8.0	3.00	3.00	10800
IRR03	10.0	2.00	1.28	10800
IRR04	10.0	4.00	2.56	10800
IRR05	10.0	5.40	3.46	10800
IRR06	12.0	4.00	1.78	10800
IRR07	12.0	6.00	2.67	10800
IRR08	12.0	7.80	3.47	10800

4.2 Numerical modelling

Besides being used into Dynasim, WAMIT was also used to perform further analysis regarding the second order potential. However, the entire problem and comparisons were executed into AQWA due to its ability of performing both frequency and time-domain analysis. All the three experiments (model fixed, free floating with horizontal mooring and free floating with catenary lines) were replicated into the potential code AQWA motivated by getting comparison data such as first and second-order forces and mean and slow-drift motions.

Further analysis were computed in the FVM software, Fluent, from ANSYS as well. For this evaluation, due to the complexity of the simulation, only the fixed tests with regular waves were developed. With the resultant data, the first-order forces in addition to the mean drift forces and wave elevations in the four wave probes could be compared to the model tests.

4.2.1 Boundary Element Method (BEM)

For the computations into the potential code, the 3D numerical model was designed at Rhinoceros, followed by the mesh developed into AQWA, Fig. 4.14, after a complete convergence analysis by comparing the RAOs of heave, roll and pitch, resulting in a 30415 elements mesh. The numerical evaluation of semi-submersible motions, in addition to the added mass, potential damping and mean drift forces, was performed in AQWA 2020R2 as well. Basically, the inputs required are the wetted surface mesh of the hull; the inertia, and a damping matrix; the wave periods; and the wave headings. Further, it was necessary to choose the pairs of frequencies for which the QTFs will be computed. Each pair of frequencies provides a difference frequency of 0.0049 Hz or 205 s which corresponds to the expected natural period of surge. The range covers the typical peak periods of the sea: 3 to 20 s.

Figure 4.14: 3D model of the platform mesh with 30415 elements.

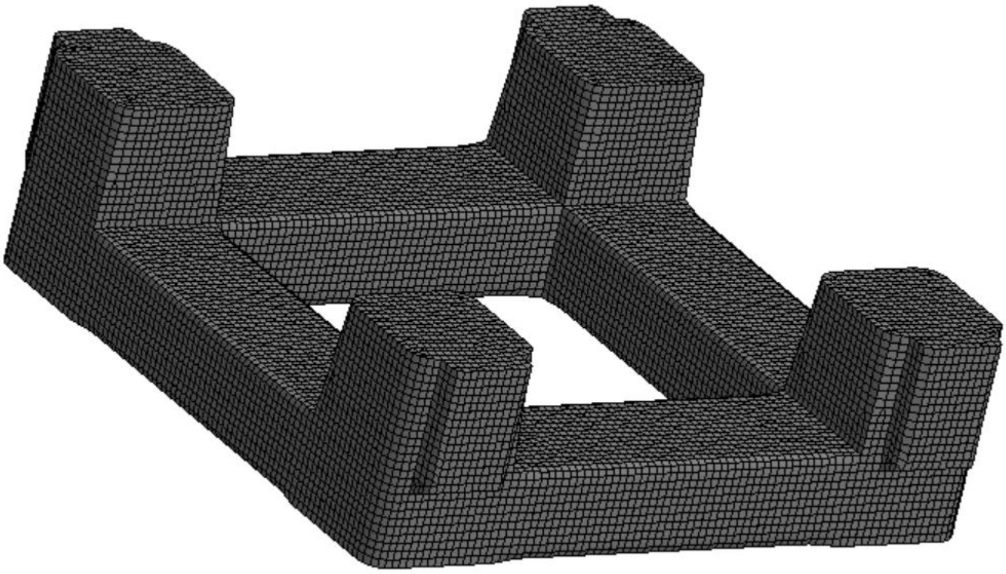

After performing a mesh convergence analysis with the RAOs, another way to check on the consistency and convergence of the first-order numerical model is by comparing the mean drift forces computed through two different methods: momentum integration based on the momentum conservation principle (far field) and the direct integration of the pressure over the body surface (near field). According to Lee and Newman (2005), the pressure integration in general needs a more accurate solution due to possible numerical errors, despite that, Fig. 4.15 shows agreeable results between the two methods.

Figure 4.15: Non-dimensional mean drift forces by momentum and pressure integration.

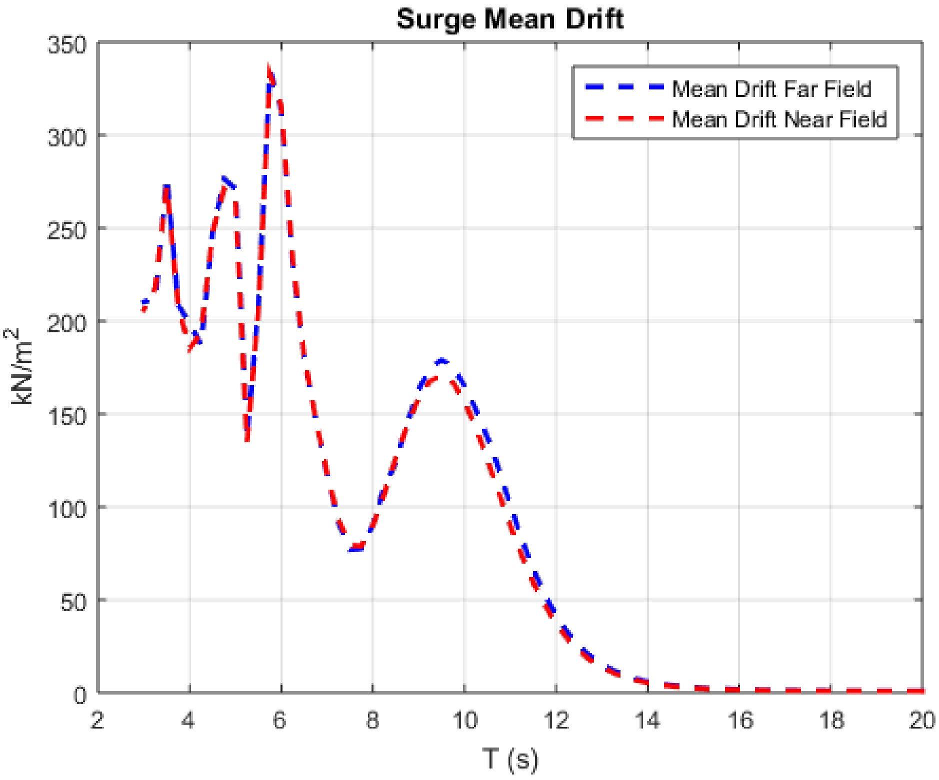

According to Ansys (2013), AQWA does not solve the complete second-order problem since the inclusion of the second-order potential is performed by applying Pinkster's approximation for long crested waves. Some authors, such as Hauteclocque et al. (2012), have indeed noticed that the second-order potential is not significant when compared to the others parcels for semi-submersible in deep waters, for finite depth water this might not be the case. However, in order to investigate the second-order potential influence in this problem, WAMIT 6.1S was used with a mesh similar to that from AQWA. WAMIT divides the second-order computation according to the second-order potential and the quadratic terms of the first-order potential.

This procedure is, for sure, more complex than only obtaining the mean drift forces and first-order dependent terms. The extended Haskind (HASKIND; NEWMAN, 1962) - Hanaoka (HANAOKA, 1959) relations (see also (NEWMAN, 1962)) enable one to determine the second-order potential forces without the need to solve for a free surface mesh field, but for this version of WAMIT, a free surface mesh had to be added into the analyses. The free surface mesh, Fig. 4.16, was also modeled into Rhinoceros, following all the recommendations specified in Wamit (2006) with 32584 panels and a RINNER = 400, which is the radius of the inner circle.

Figure 4.16: Free surface mesh for WAMIT with 32584 panels.

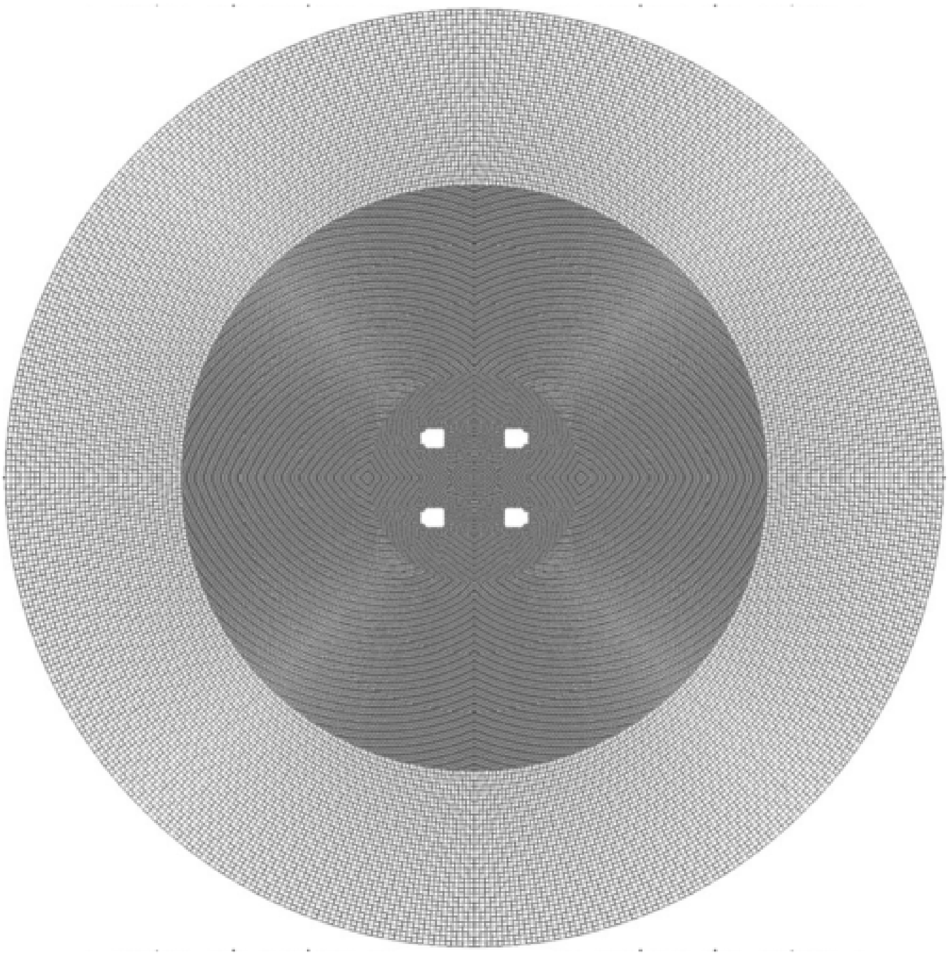

Figure 4.17 compares the QTF computed considering all the terms and the QTF without the second-order potential, which does not use the free surface mesh. No considerable differences are identified. Therefore, the second order potential terms indeed do not interfere significantly on the QTFs results in this case and the quadratic component is the relevant and dominant constituent in this scenario, as it was already noticed in Section 3.6.

Figure 4.17: Non-dimensional computation of complete QTFs and without the second-order potential computed by WAMIT.

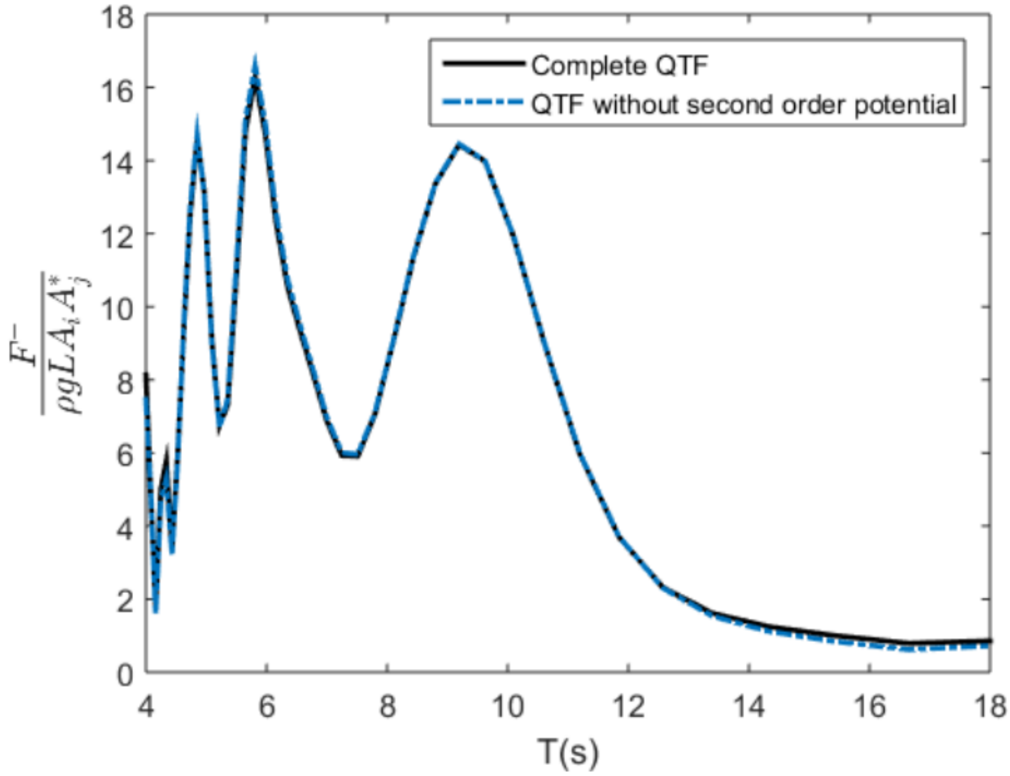

By now knowing that the second-order component is not contributing to this problem, it was decided to keep performing the analysis on AQWA since it has the advantage of the time-domain simulations integrated into it, besides providing the direct and instantaneous visualization of the studies.

A further investigation can be performed in accordance with Chapter 3.5. Both Newman's (NEWMAN, 1974) and White-noise's (ARANHA; FERNANDES, 1995) approximation models consider that when the natural frequency is small enough, the second-order forces can be approximated by a relation with the mean drift forces. For that, in the QTF, the off-diagonal terms which are close to the main diagonal should present similar values to those of the main diagonal in the complete force QTF for the platform, which is presented in Fig. 4.18.

Figure 4.18: Complete force QTF matrix computed by AQWA.

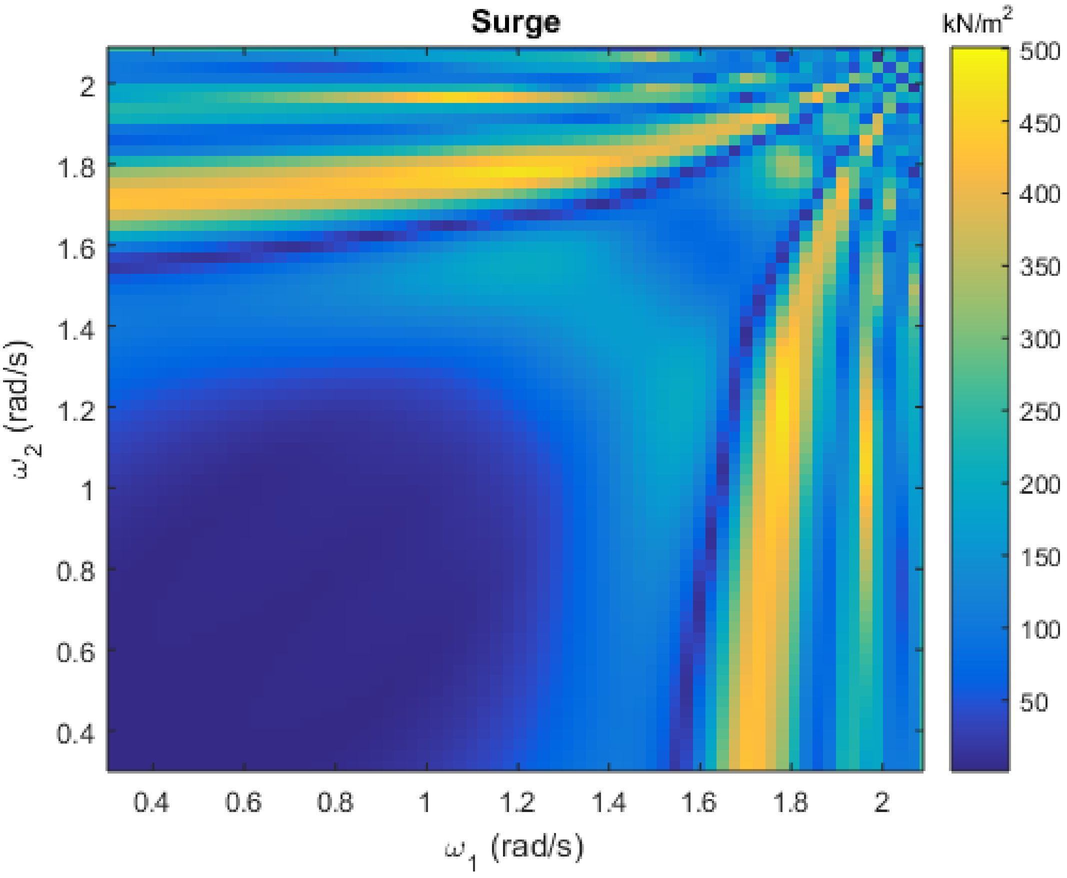

As the scale of Fig. 4.18 is not favoring the visualization of the QTF main diagonal, only the three closer off-diagonal terms were plotted in Fig. 4.19. At the low frequency range, the values of the main and off-diagonal are very close to each other. On the other hand, at the higher frequencies, larger than 1.95 rad/s (3.22 s), the off-diagonal values are not that similar to the main diagonal. However, this is a very low period where few energy waves are found. Therefore, it is expected that both approximation models can represent the second-order forces well, although their performance were not tested in the scope of the present research.

Figure 4.19: QTF computed by WAMIT only at the three off-diagonals closer to the main diagonal.

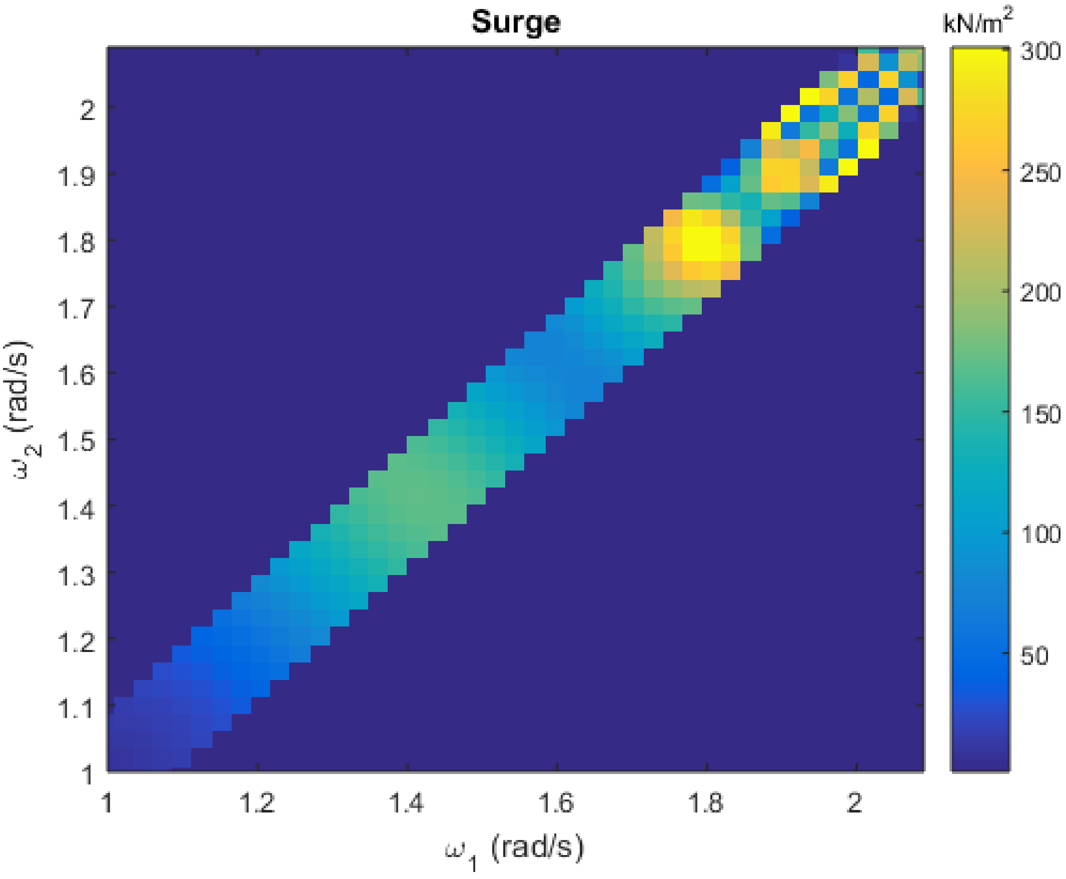

4.2.1.1 Viscous Damping

Two distinct methods were used to represent the viscous damping effects, as stated in Chapter 3.7: decay tests and Morison's elements.

The first method for estimating the viscous damping in surge required having the decay tests results, which depend on the platform displacement $M_{11} = 79856.4$ t, added mass $A_{11} = 47548$ t (at zero frequency limit), natural period $T_n = 205$ s. Further, a ζ value, which is the viscous damping percentage of the critical damping and depends on the surge significant amplitude and the decay tests curve from Fig. 4.20, must be defined.

Figure 4.20: Surge decay test with soft mooring in real scale.

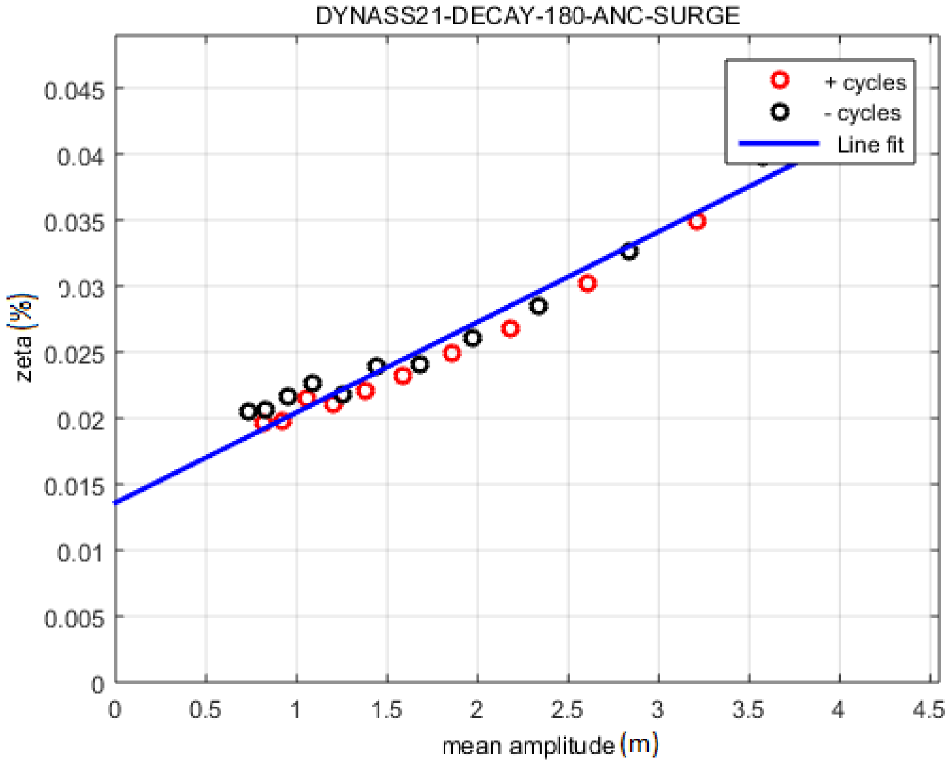

Hence, the external viscous damping, B_{ext}, is given by Eq. 4.1. Knowing that this method is prone to significant uncertainty, an error margin of ±30% of the values resulting from this equation were also used as input values in AQWA.

$$B_{ext} = 2(M_{11} + A_{11})\omega_n\zeta \tag{4.1}$$

Further, still thinking about reducing the error caused by the uncertain process of choosing the external damping values, the motions were computed by another external damping input approach with Morison's elements features which are already incorporated into AQWA. In this case, the only inputs are the drag and inertia coefficients C_D of the columns and pontoons. In accordance with (LÁVIČKA; MATAS, 2012), these values for the dimensions of the columns and pontoons are respectively $C_D = 2.10$ and $C_D = 1.80$.

Figure 4.21 presents the decay test performed into AQWA with the Morison's elements in comparison with the experiments, in which it is possible to notice a good agreement of AQWA both in terms of amplitudes and periods. There is a slight detachment at the end of the time series, where the amplitudes are smaller, but this should not compromise the results.

Figure 4.21: Surge decay comparison between experiments and AQWA with Morison elements.

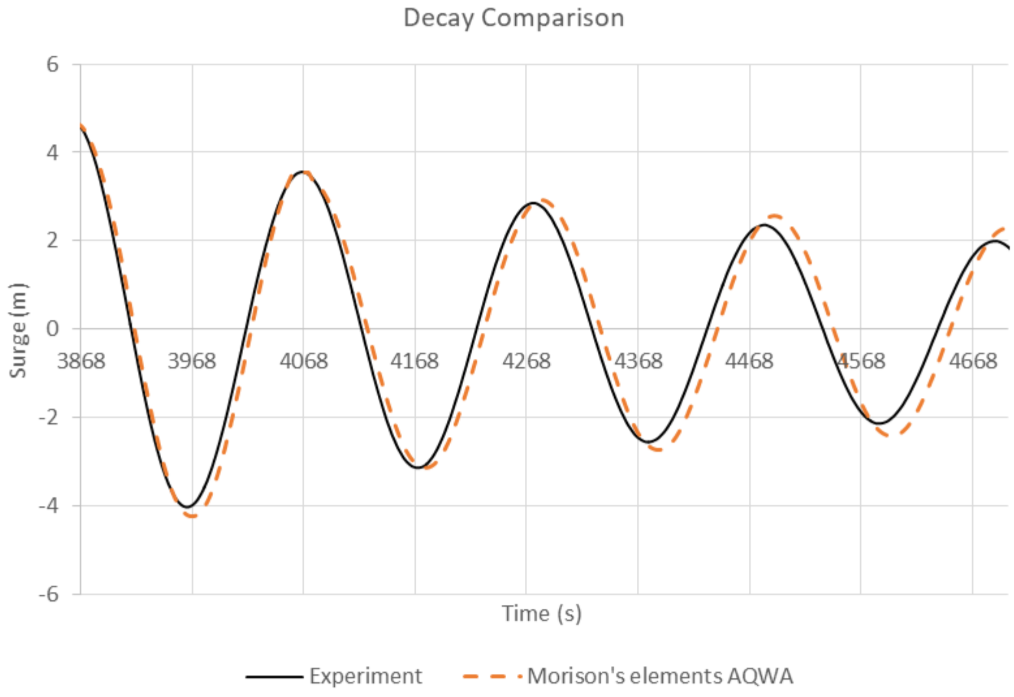

4.2.2 Finite Volume Method (FVM)

The implementation of a numerical technique, such as CFD based on FVM in this instance, is a complex process that demands a thorough comprehension and analysis of numerous variables. As previously noted, Fluent 2020R2 from ANSYS which is based on the Reynolds-averaged Navier–Stokes equations (RANS) was selected as the preferred program, and this section presents the parameters and models utilized in the construction and execution of the simulations. The fundamental process in any CFD tool based on FVM is partitioned as illustrated in Fig. 4.22, and the subsequent subsections provide a brief summary of each of these phases.

Figure 4.22: CFD development structure.

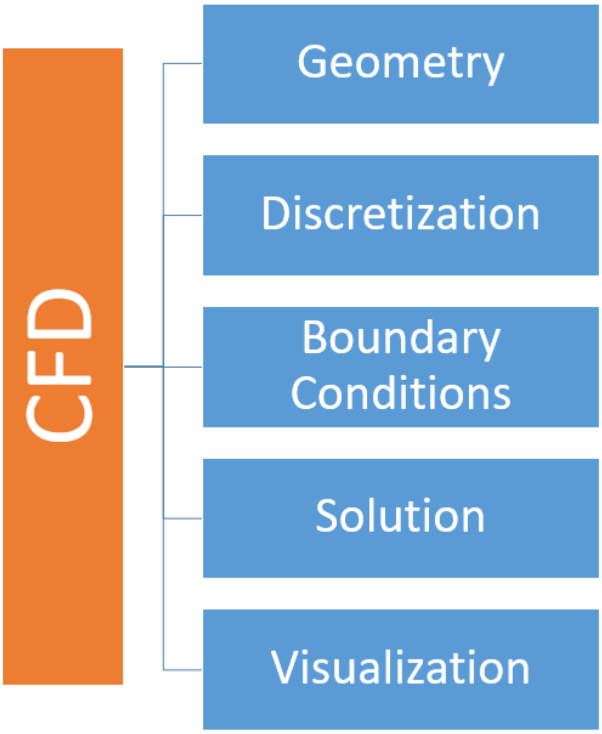

Besides respecting this development structure, verification and validations procedures must be performed. Mesh convergence analysis, Courant-number evaluation, boundary conditions and solutions parameters selection were all chosen carefully and analysed via verification procedures. For the validation, the wave elevation at the four probes and both first order and mean drift forces from the model tests were used.

4.2.2.1 Geometry

As the flow occurs around the hull, which is an external flow, it is necessary to limit the region of the same through a domain. In the literature there are many authors, such as Bućan, Buča and Ružić (2008), that suggest the size of the computational domain for a hull resistance simulation, however, no waves are involved. Hence, for the case in question a type of size domain analysis was performed with some main restrictions: At least one wavelength from the inlet boundary to the model; the bottom should be deep enough to avoid shallow water; the sides and outlet region should be far enough to avoid reflection effects. After some iterations, all these criteria were met and the resultant domain is introduced in Fig. 4.23. In addition, a virtual beach for damping the waves and for avoiding reflections was placed at the aft region.

Figure 4.23: Computational domain size for CFD simulations in model scale (1/100) with the dimensions in mm.

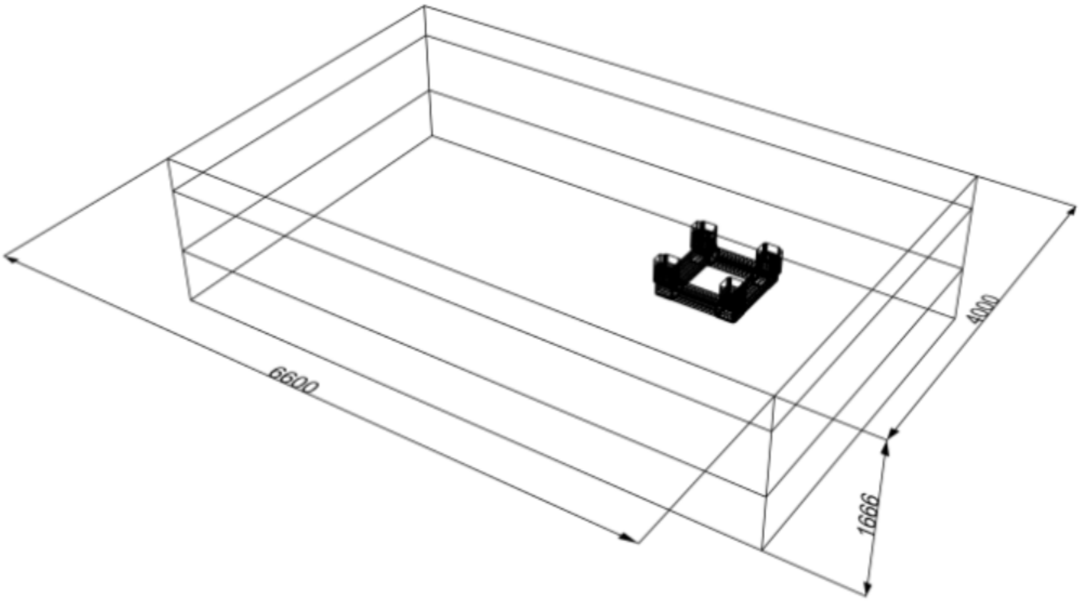

4.2.2.2 Discretization

The generation of the mesh is divided into surface mesh and volumetric mesh. The unstructured surface mesh is applied on the surface of the hull and the volumetric, structured, on the computational volume domain. Structured meshes are generated from surface meshes, providing continuity in the computational domain Lira et al. (2002). To save computational time, some regions of lesser interest received a different discretization, while regions of greater interest were more refined. The region that matters most for this simulation is the hull, of course, followed by the waterline, due to the water-air interface waves, thus generating three refining different mesh regions. Further, inflation layers were created all over the hull by following all the recommendations from ANSYS, as Fig. 4.24 presents.

Figure 4.24: Inflation layer and volumetric mesh.

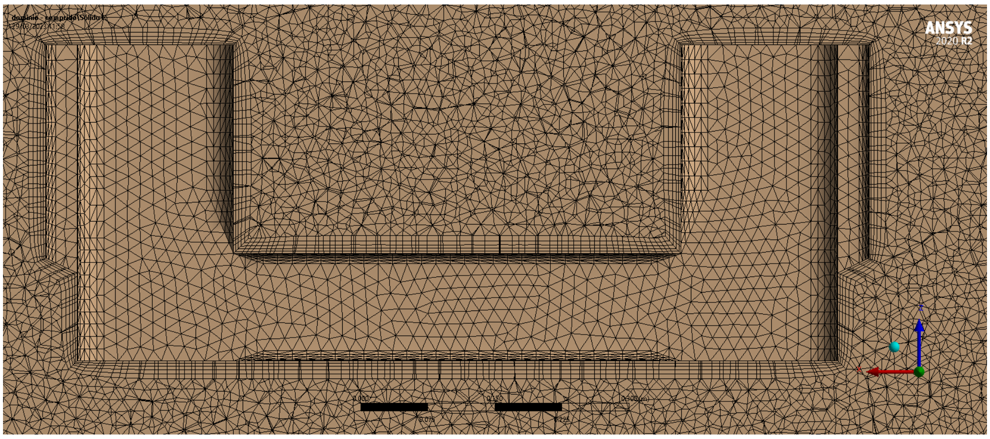

A convergence analysis of the mesh, which is a verification procedure, was conducted by varying the element base size, resulting in a change in the number of model elements and by comparing the surge mean drift forces responses. The mesh refinement process continued until the results exhibited minimal variation. This analysis considered both the longest and shortest wave periods, T = 7 s and T = 11 s, and their respective mean drift forces. In practice, the entire process was conducted only for T = 11 s, and the results were subsequently verified for T = 7 s, as depicted in Fig. 4.25.

Figure 4.25: Mesh convergence analysis.

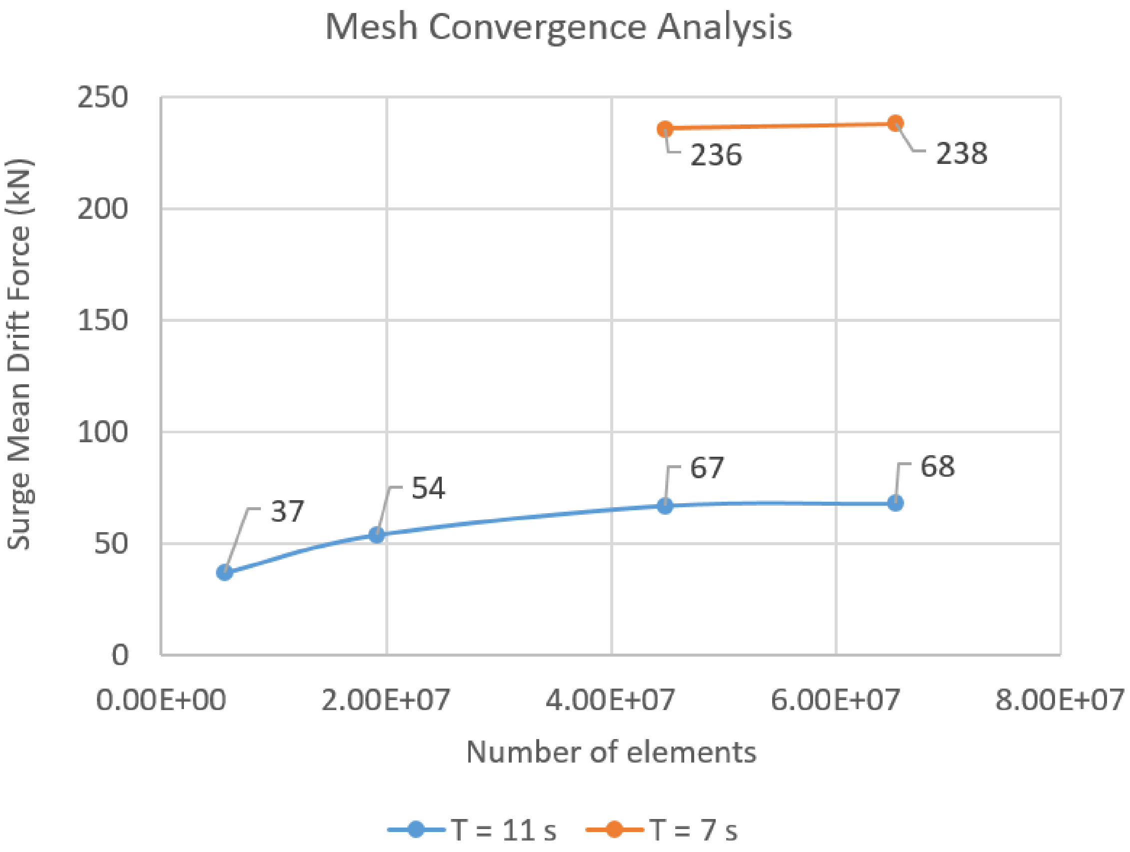

The mesh with $44.8E + 06$ elements yielded less than 2% difference from the mesh with $65.3E + 06$ elements for both extreme periods examined, and thus, it was selected for conducting the analysis, as depicted in Fig. 4.26. Notably, this is a significantly refined mesh that results in substantial computational expenses, requiring 2 to 3 weeks for convergence of at least five cycles in a workstation with 94GB of RAM memory and 24 cores. The high level of refinement is necessary to accurately represent waves in the computational domain, as inadequate mesh refinement may lead to wave damping along the x-axis. This highlights the considerable time and computational expenses associated with this type of analysis.

Figure 4.26: Part of the final mesh configuration with $44.8E + 06$ elements.

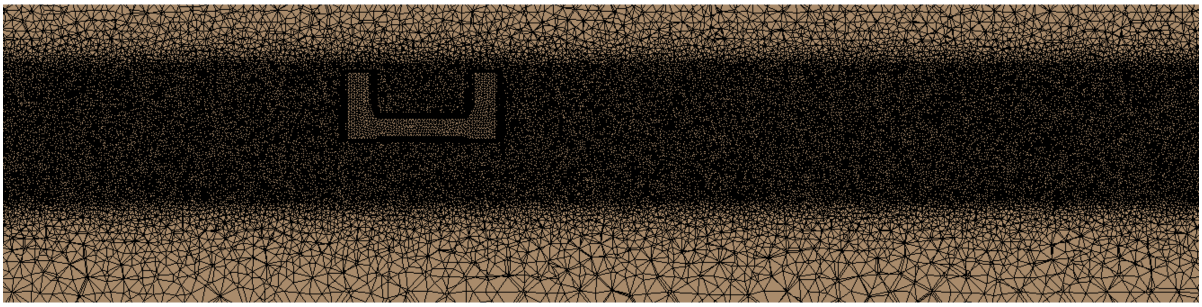

4.2.2.3 Boundary Conditions

It is necessary to define a boundary condition for each face that delimits the computational domain. The front region of the domain is defined as velocity inlet with open channel waves, that is, they refer to the input of the fluid into the control volume following the Airy wave theory. The aft face is the pressure outlet in function of the hydrostatic pressure of the generated wave. The top, bottom and sides are defined as walls with a slip condition, while the hull surface refers to a non-slip condition of the fluid next to the surface.

4.2.2.4 Solution

For the solution set-up, Manual (2009) was used in addition to the ESSS support (ANSYS representation in Brazil) during the entire process. The RANS (Reynolds-Averaged Navier-Stokes) method was used with a $k\omega$-SST viscous model with a transient formulation that is defined as bounded second-order implicit. This model is essential to obtain a good representation of the inlet wave along the domain. The Volume of Fluid (VOF) model with an implicit approach was used as the multiphase model and the time step was chosen to meet the Courant Number criteria. The incident waves were modelled through Airy first-order models, but just for evaluation purposes, the case of T = 10s was also run with a 2^{nd} Stokes wave model, and the differences in the free surface elevations have not exceeded 3%. This small difference was already expected due to the small steepness of the incident waves.

The simulation concludes after five complete cycles of the surge first-order forces along the time without significant variation in the force amplitude (±2%) from peak to peak. Figure 4.27 shows the complete force time-series for the simulations of T = 10 s, in which the orange section represents the converged region.

Figure 4.27: Surge force time series for T = 10 s.

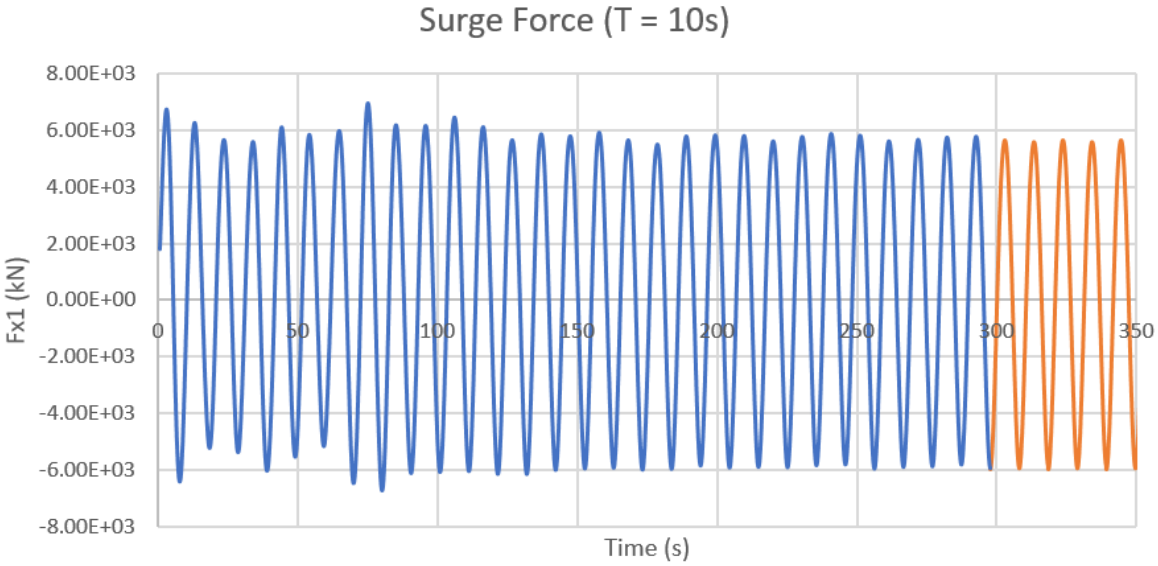

The procedure performed for treating the results from the experiment was exactly the same for the CFD. The mean of the positive and negative maximum peaks are taken to get the first-order force amplitude. For the mean drift forces, the mean of all the points in those five cycles are calculated. Fig. 4.28 exemplifies surge forces records for REG02 (H = 2m and T = 8s) obtained thought Experiments and CFD in which it is observed that the CFD needs time to converge, but a very good agreement between the numerical and model tests results is achieved.

Figure 4.28: Surge force time series for T = 8 s (Experiment x CFD).

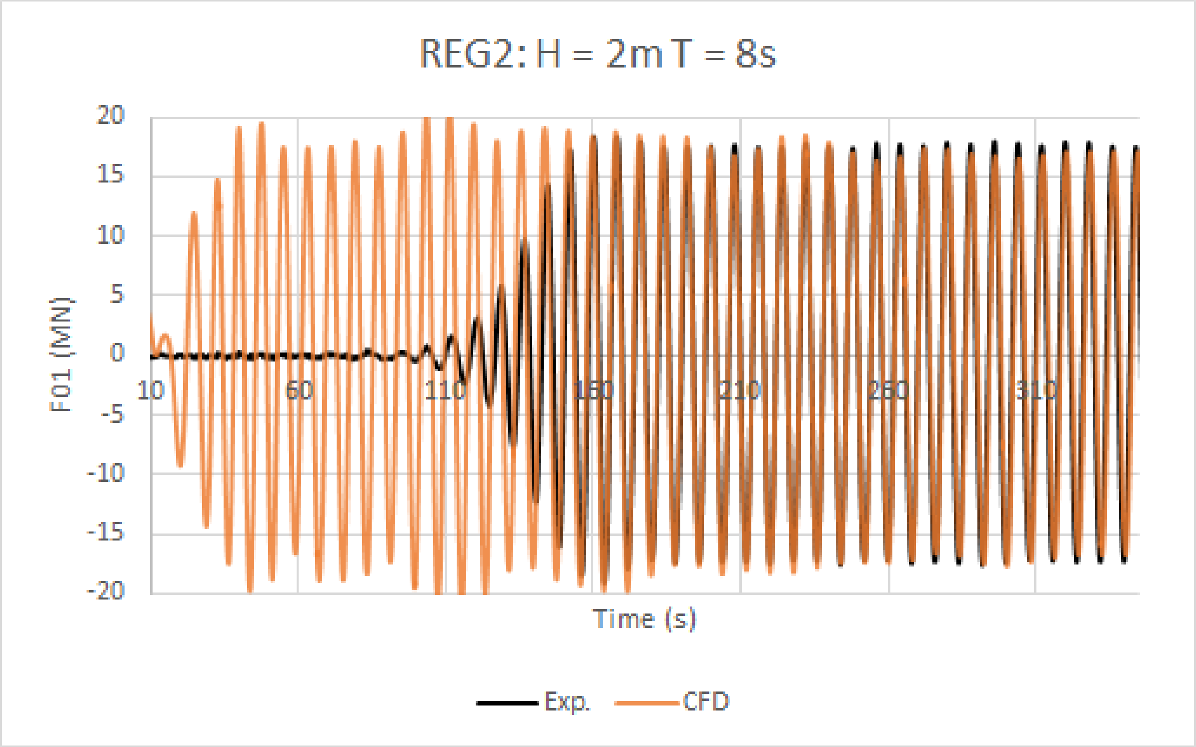

Another essential step to analyse the CFD solution is to compare the free surface elevation at the wave probes. Figure 4.29 presents the comparison of the wave elevation at wave probes 1 and 2 only, since 3 and 4 are similar. The first step is to confirm the phase and wavelength size for the CFD in relation to experiments, which are one more time in accordance with the experiments. The second step is to compare the wave amplitudes. For this case, the CFD prediction is about 4 to 7% larger than the experimental wave amplitudes, which is considered reasonable for this analysis. Actually, this was the case with the largest difference between the CFD and model tests, as it is going to be discussed ahead, in Sec. 5.3.2.

Figure 4.29: Wave elevation at the wave probes 1 and 2 for T = 8 s (Experiment x CFD).

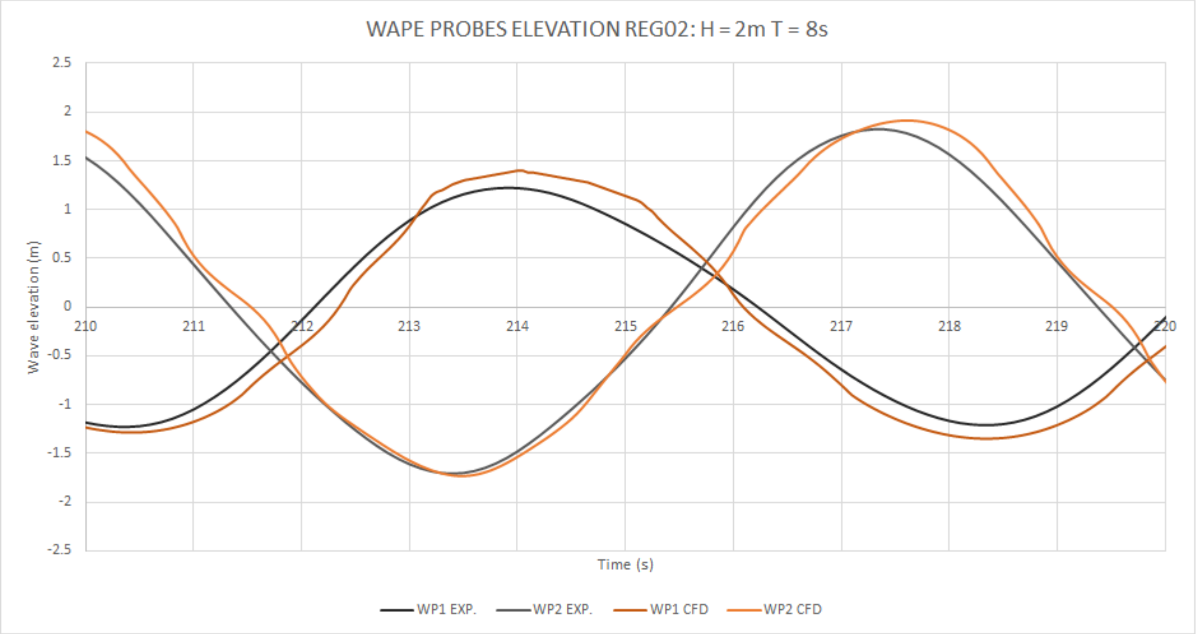

4.2.2.5 Visualization

Visualization features are also beneficial for providing data to verify the accuracy of numerical simulations. Fluent includes a visualization tool that enables the flow to be displayed at each time step, as depicted in Fig. 4.30 and 4.31. This provides a means of ensuring that the simulations are being solved correctly. Moreover, the wave height and wavelength were monitored throughout the duration of the five cycles.

Figure 4.30: CFD visualization for T = 9 s simulation.

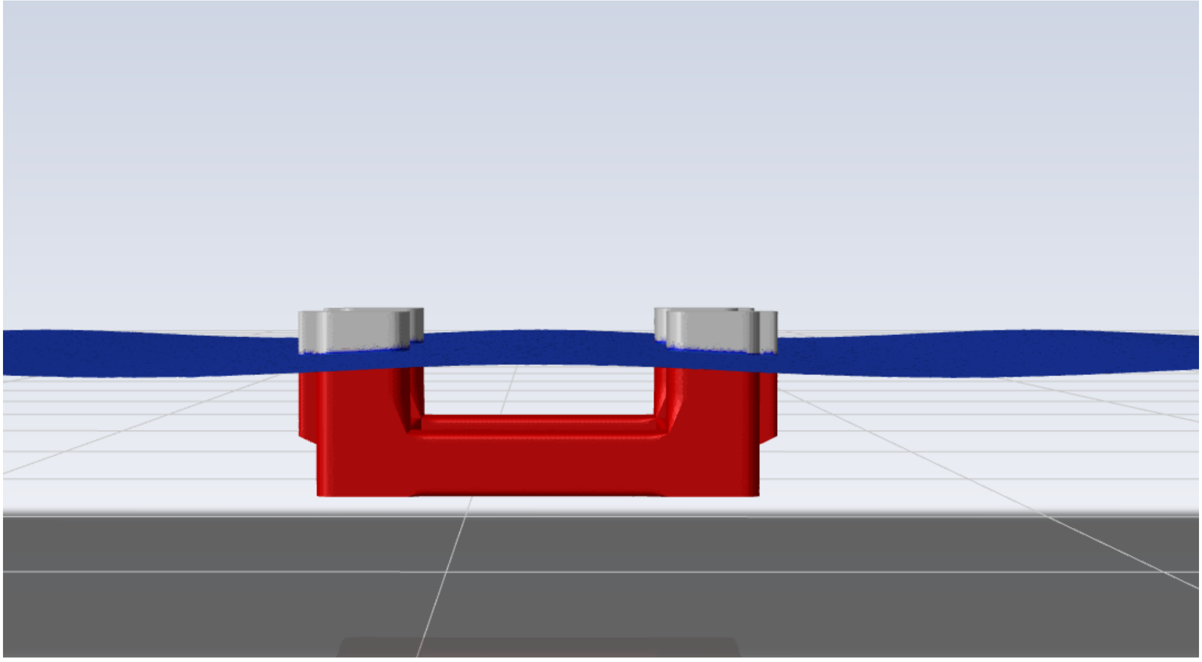

Figure 4.31: CFD visualization for T = 9 s simulation perspective view.

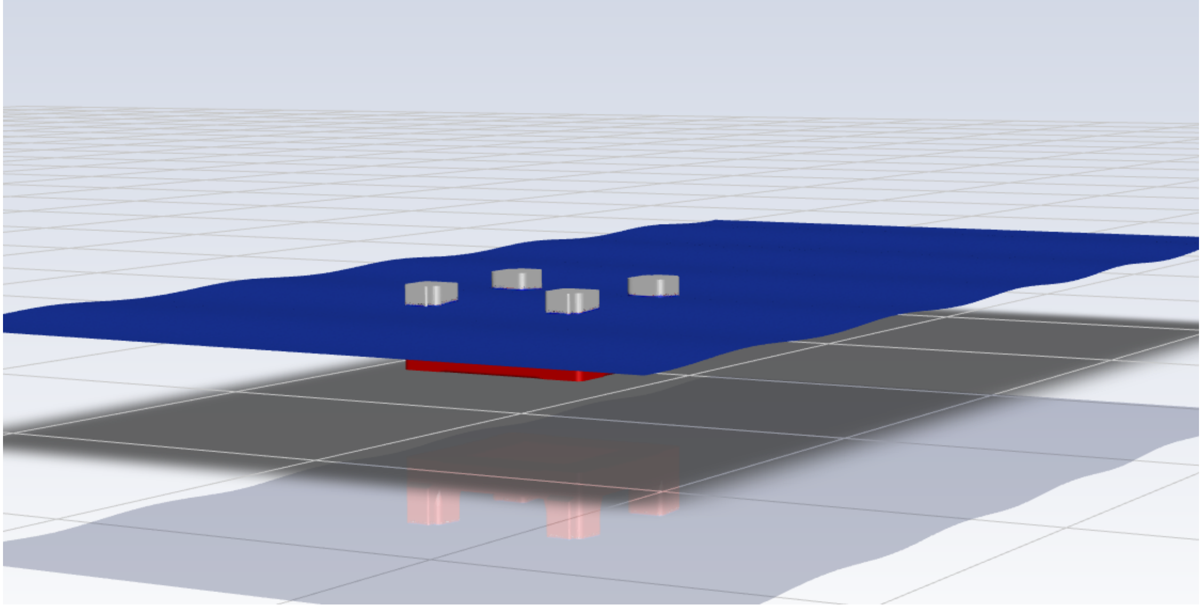

In addition to the simulation itself, another verification procedure is to examine residuals, as they indicate how accurately the simulation converged to an acceptable approximation of the real flow. If the values are high, it suggests that the mesh was not well-suited or that instabilities occurred during the process. Residuals can be defined as the difference between the last iteration of the algorithm and its penultimate iteration.

By Tab. 4.9, it is observed that the most important residuals were those of turbulence, continuity, and the moment at x, all of which were less than 0.001 at the conclusion of the simulation, indicating a good convergence of the flow. In addition to these verification procedures, validation procedures were also conducted, and their values will be presented along with the results in the following chapter.

Table 4.9: Residuals values for T = 10 s.

Residuals	Value
Continuity	$\leq E-03$
x-velocity	$\leq E-04$
y-velocity	$\leq E-04$
z-velocity	$\leq E-04$
k	$\leq E-05$
ω	$\leq E-06$
vf-water	$\leq E-05$

5 Main results

In this chapter, the agreement between the predictions made by the computational methods (BEM/AQWA and FVM/Fluent) and the experimental results is illustrated and discussed (all results are in full scale). The analysis of the different tests also allows one to infer the possible sources of errors involved. The results are split into first and second-order forces and motions generated by regular and bichromatic waves, in which steady-states and frequencies of oscillation are well defined. Irregular waves experiments and evaluations with the outcomes from BEM code are also presented at the end of the chapter. Both numerical and experimental uncertainty ranges were not measured in this work due to time restrictions. However, the repetition of the captive model tests under regular waves provides an indication of how the experimental uncertainty range would behave.

5.1 Free floating tests in bichromatic waves with horizontal mooring

The first step was investigating whether or not there is a problem presented by the potential codes in predicting the slow-drift motions for this platform. With the aim of evaluating this problem, BEM code results under bichromatic waves were taken from AQWA and plotted against the corresponding values derived from the experiments.

As stated before, performing this analysis with bichromatic waves has the advantages of achieving the steady-state faster and being able to isolate the natural frequency of the motions. Figure 5.1 introduces the comparison for the mean drift in surge direction in 180^o heading. Here, it is important to highlight that the external damping does not interfere in the values. Results show reasonably good agreements between AQWA and the experiments for all the periods, except for BIC04 (T = 10 s and T = 10.51 s) in which the BEM code underestimated the experimental mean offset by about 35%. Even if there was a quantitative uncertainty bar range, such a large difference would improbably be within the numerical results.

Figure 5.1: Mean drift motions in bichromatic waves comparison between BEM and the the experiments.

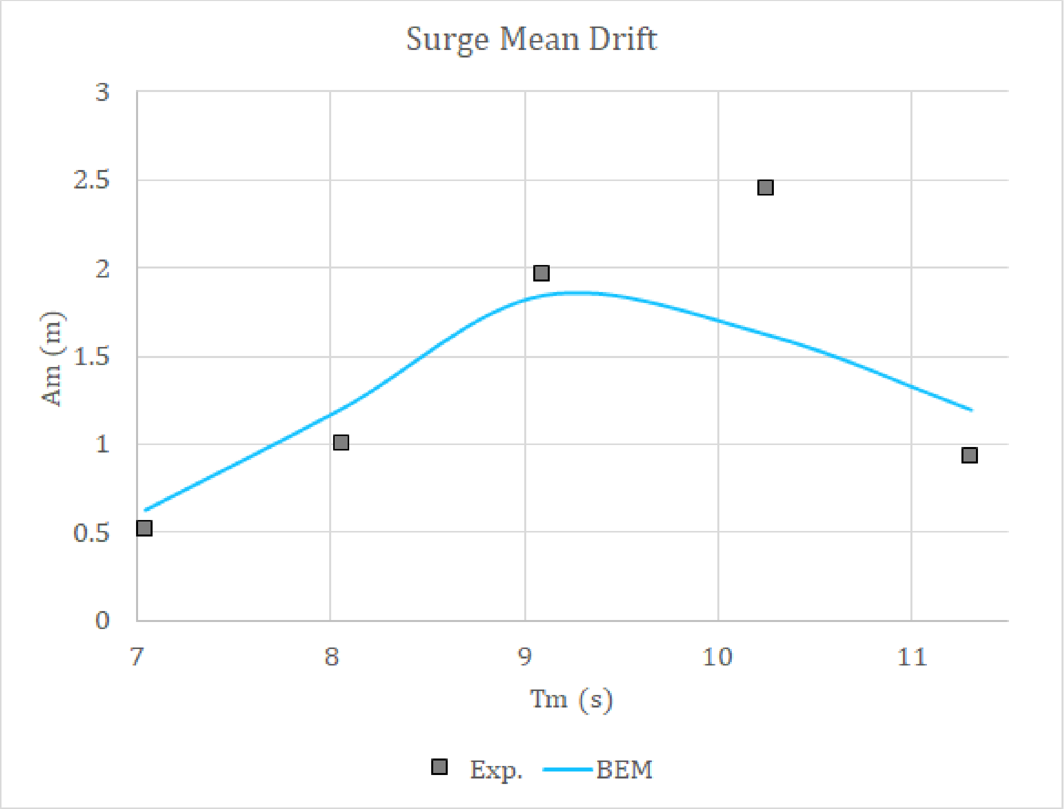

Figure 5.2 introduces the comparisons for the significant surge slow-drift amplitudes A_s, which on the other hand, are dependent on the viscous damping input. For these comparisons, the procedures described in Section 4.2.1.1 were used: AQWA computations with the decay values and ±30% of the decay values, in addition to the simulations using the Morison's elements. The decay results provide a margin in which it is expected that the experiment values are within.

The output remarks that the simulations with the Morison's elements are in an excellent agreement with the experiments, although differences are found for one run. Once again, the only case that shows a pronounced deviation between the experiments and the predictions is BIC04, whose results are being underestimated by AQWA irrespectively of which damping method is being used.

Figure 5.2: Slow-drift motions in bichromatic waves comparison between BEM and the the experiments.

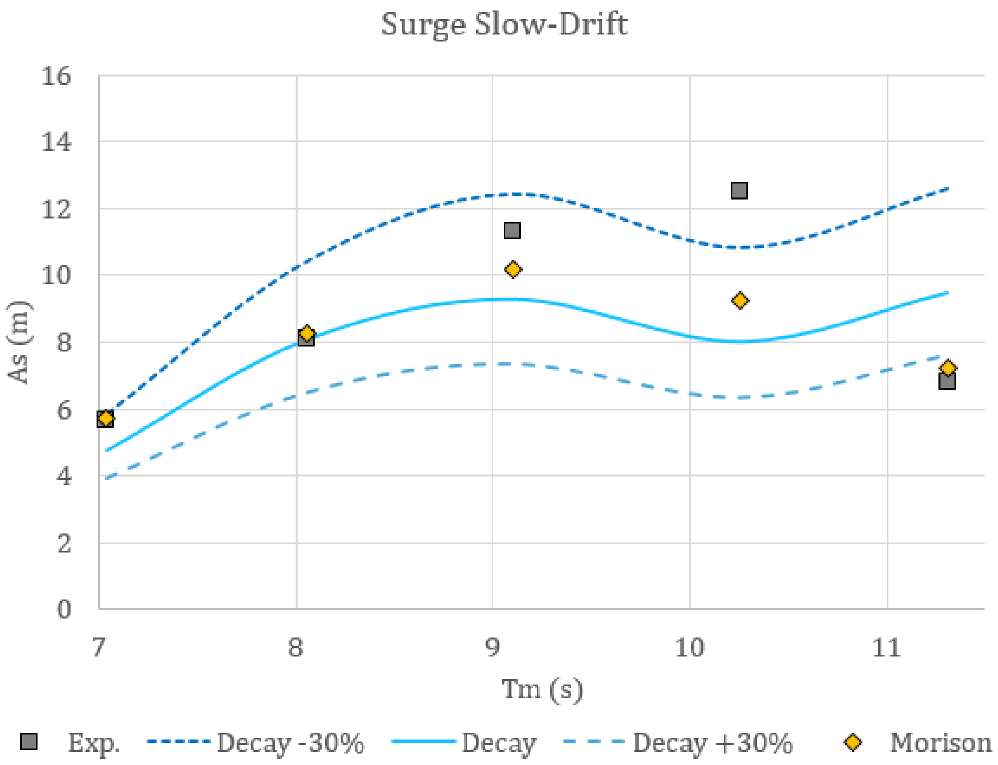

Having these results in hand, it is possible to infer that there is indeed an underestimation in the mean and slow-drift motions for BIC04 with a $T_m = 10.25$ s period and which are probably correlated with each other. For the other periods, the results are in accordance with the experiments.

The next sections will decompose the problem in force components in order to try to isolate and identify the source of this issue.

5.2 Captive tests in regular and bichromatic waves

The first-order results are segregated in first-order forces, having as benchmark the fixed model tests with regular and bichromatic waves; and RAOs based on free model tests in the same bichromatic waves. As stated earlier, the captive tests are capable of providing the direct measurements of the forces acting on the platform, both for first and second-order components. Due to their small magnitudes, the expected second-order forces were restricted to the loading cell limitations. These forces for smaller wave amplitudes, such as A = 0.5 m in real scale, could not be captured during the experiments at some periods.

5.2.1 First-order Forces

The second step was to be sure that there are no significant errors in the BEM code prediction regarding the first order forces that could be carried to mean and slow-drift results. As stated in Chapter 4, five regular waves with periods from 7 to 11 s were tested with the model fixed to the tank bridge. Figure 5.3 shows the first-order forces comparison between FVM and BEM results against the experimental measurements. For the captive tests, a repetition of each experiment run was carried out, therefore they are represented by Exp.1 and Exp. 2. therefore Fluent matched the forces very well for all periods, while AQWA has slightly underestimated the forces amplitudes at 10 and 11 s of period.

Figure 5.3: Surge forces in regular waves at 180^o (Captive tests).

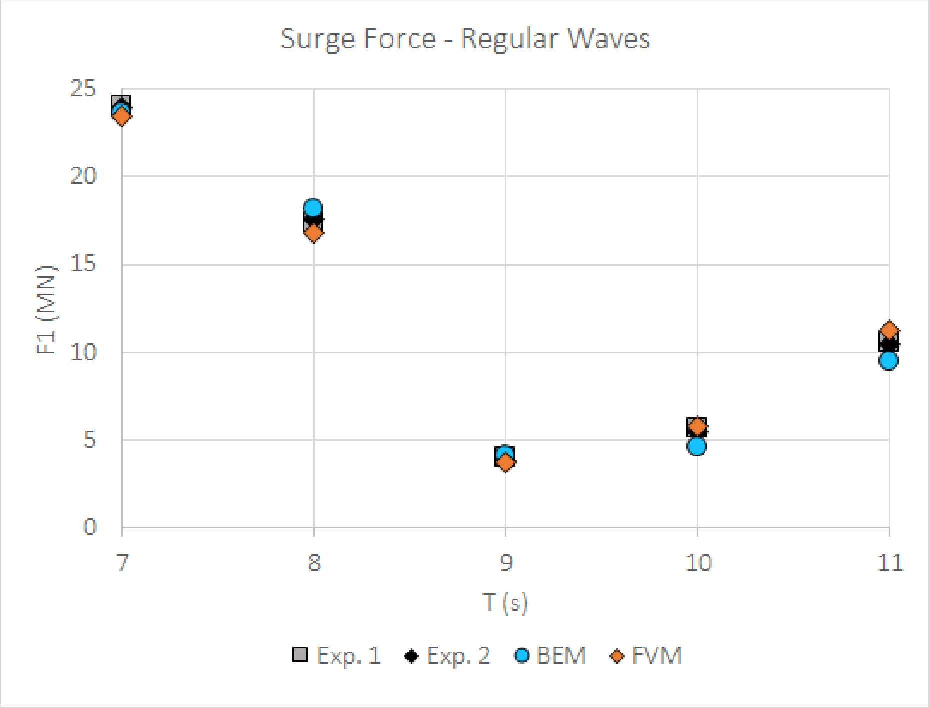

Regarding the bichromatic waves forces, captive model tests with similar period ranges were conducted as well. For treating the data, the wave amplitudes from the first converged cycles are taken, in order to avoid transient effects. Thus, the amplitude time series is transformed into a spectrum to define how much energy is at each frequency and then the wave amplitudes $A1$ and $A2$ are related to the amount of energy at each frequency. Figure 5.4 shows the wave elevation time series of the experiment and Fig. 5.5 introduces the spectrum for the BIC04 case. All the experimental wave series were input into AQWA and the same procedure to treat the results was performed.

Figure 5.4: Wave elevation in the bichromatic (BIC04) experiment (Captive tests).

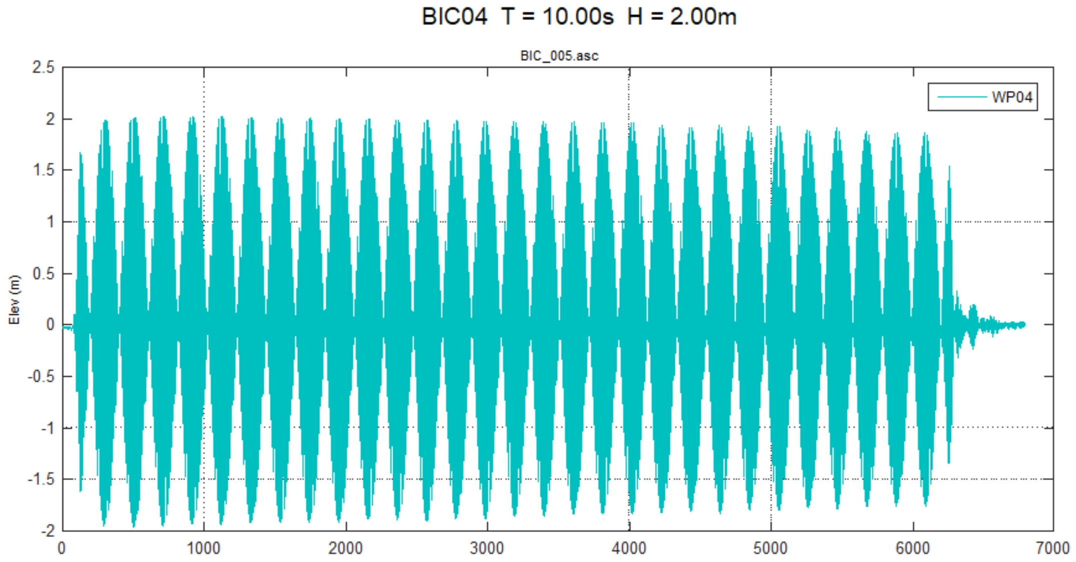

By knowing how much energy is at each period (Fig. 5.5) and by the total amplitude at each case (A = 1.98 m for BIC04), with a simple percentage account, the amplitudes achieved were A1 = 1.10 m and A2 = 0.88 m for this case.

Figure 5.5: Wave elevation spectrum for bichromatic (BIC04) experiment (Captive tests).

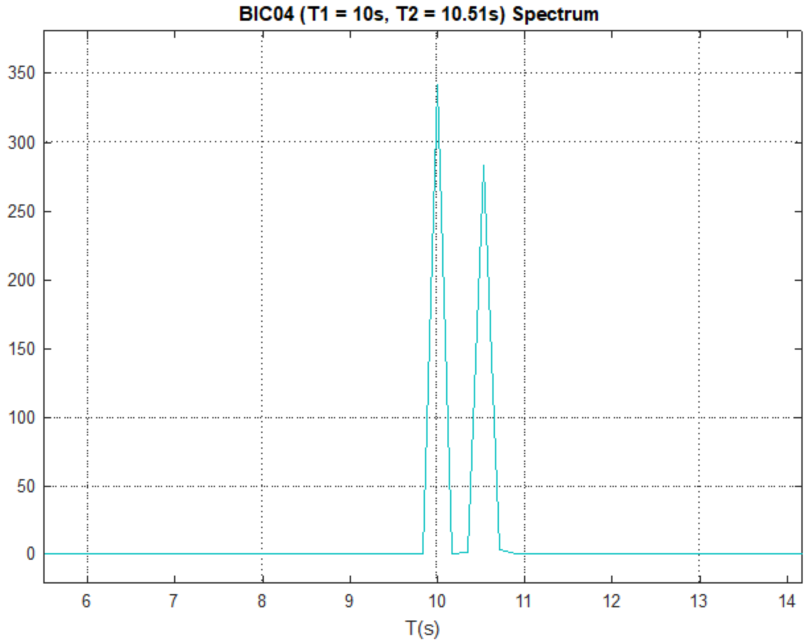

Having the wave amplitudes of the two components of the bichromatic waves, the low-frequency forces can be normalized by the product $A1.A2$. In this case, it is necessary to use a filter for getting higher periods than 200 s. One more time, the mean of the maximum and minimum peaks of the initial steady cycles are taken from Fig. 5.6, for example, which presents the first-order force and the low-frequency force for the BIC04 time series.

Figure 5.6: First-order and low-frequency force in surge in bichromatic (BIC04) experiment (Captive tests).

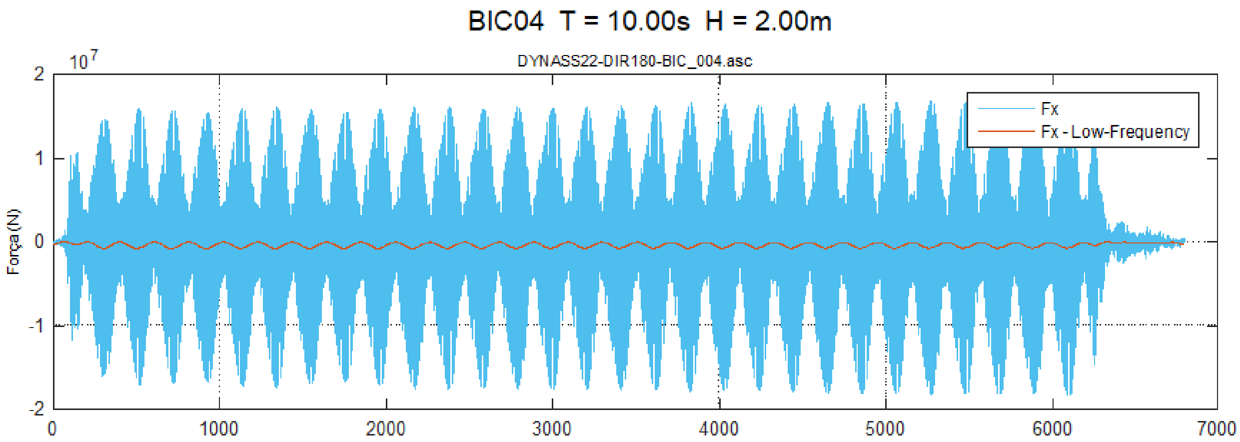

For the bichromatic waves, the first-order forces numerical results are restricted only to the potential code AQWA, which has captured the results reasonably well for all periods, except for BIC03, in which the force response is small and BEM has overestimated it, as Fig. 5.7 presents.

Figure 5.7: Surge forces in bichromatic waves at 180^o (Captive tests).

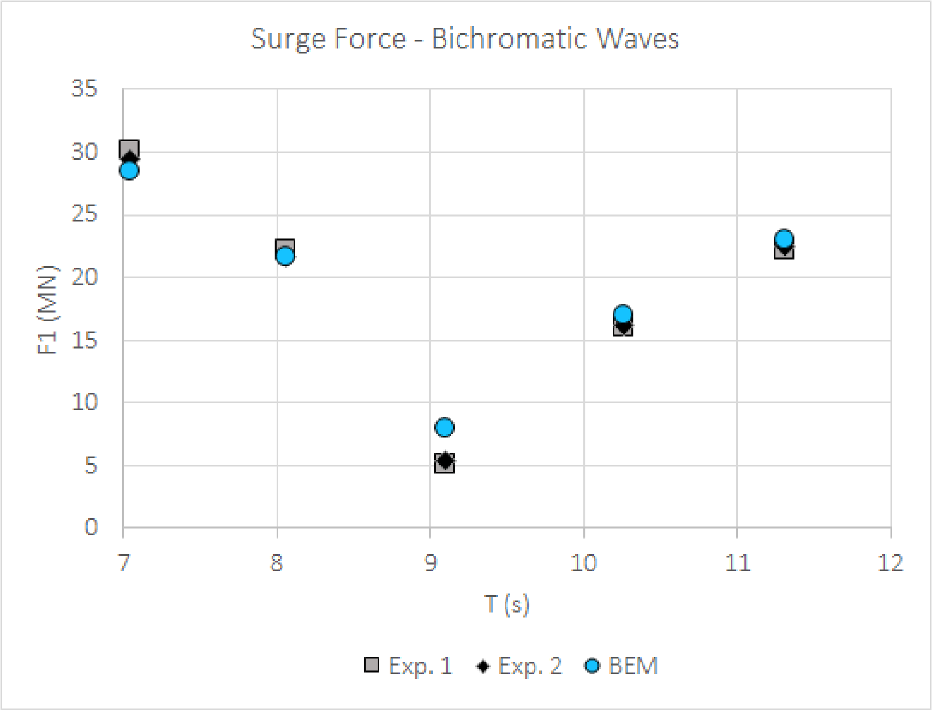

Having both regular and bichromatic results, it can be stated that the first-order forces are being well estimated by the BEM code in general. Then, next it is possible to check if the first-order motions are being well reproduced by the numerical code as well.

5.2.2 First-order Motions

The third procedure was to verify the representation of the BEM code regarding the first-order motions since slow-drift motions are dependent on them. The experimental first-order motions were only compared to AQWA results since this type of simulations are extremely complex CFD. Results in Fig. 5.8 and 5.9 show the good agreement obtained for the surge and heave RAOs between the potential code and the experiments. Nonetheless, as Fig. 5.10 illustrates, the reproduction of the pitch motions were subjected to more significant deviations, especially around the period of 10 s, which represents the wavelength with twice the columns spacing, thus the fore and aft columns are in opposite wave-induce locations, maximizing the pitch wave excitation moment.

Indeed, this motion is directly correlated to surge motions of both first and second-orders, so it rests to know if the pitch motions are being influenced by surge motions or if the opposite is true. But actually, the difference between the pitch numerical and experiments corresponds to a 0.06° difference. If we consider a regular wave of A = 1.0 m and the half length of the platform, L/2 = 42.5 m, the resultant vertical difference at the very forward edge of the platform is in an order of less than 1 centimeter, which is a negligible deviation. Here, it is also important to notice that the pitch natural period is 35 s, and hence the damping factor input is not interfering in the results.

Figure 5.8: Surge RAOs in bichromatic waves at 180^o.

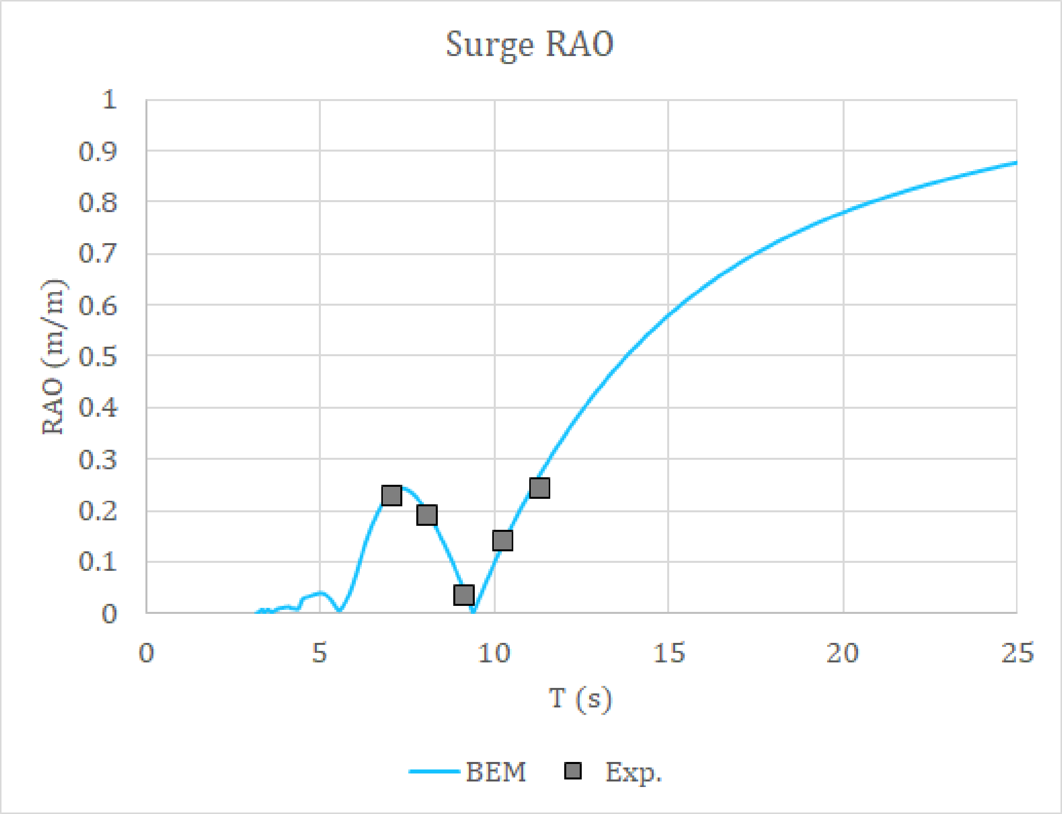

Figure 5.9: Heave RAOs in bichromatic waves at 180^o.

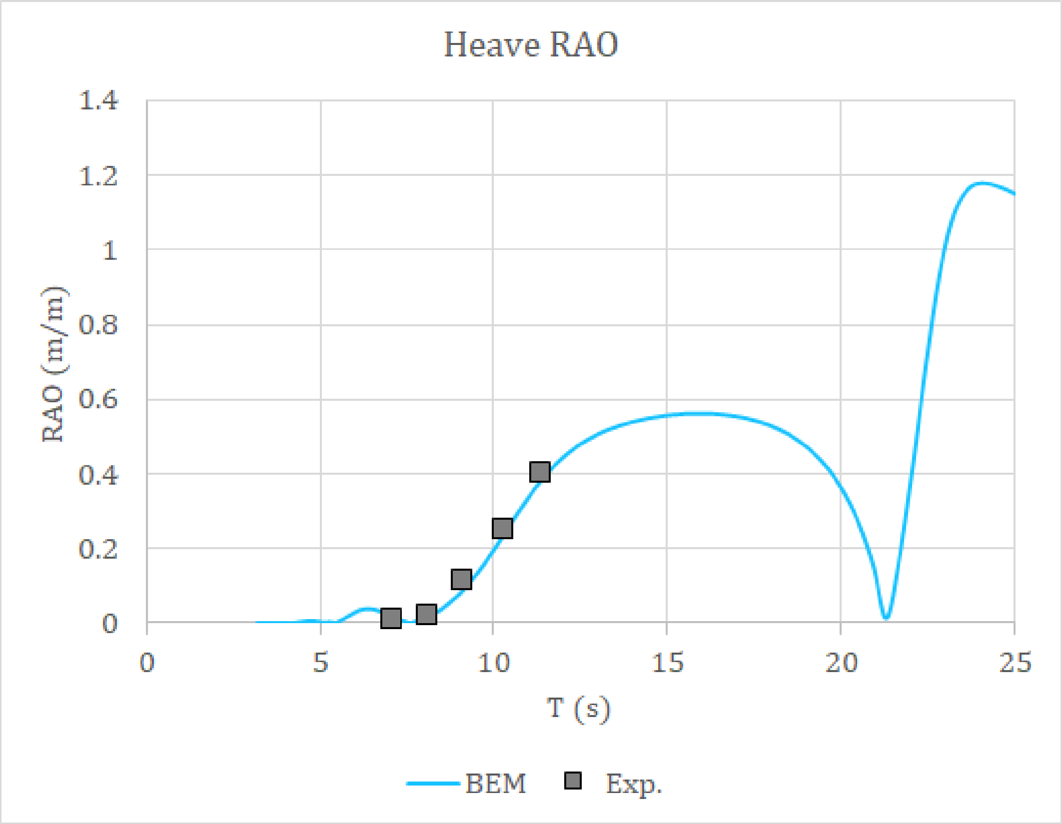

Figure 5.10: Pitch RAOs in bichromatic waves at 180^o.

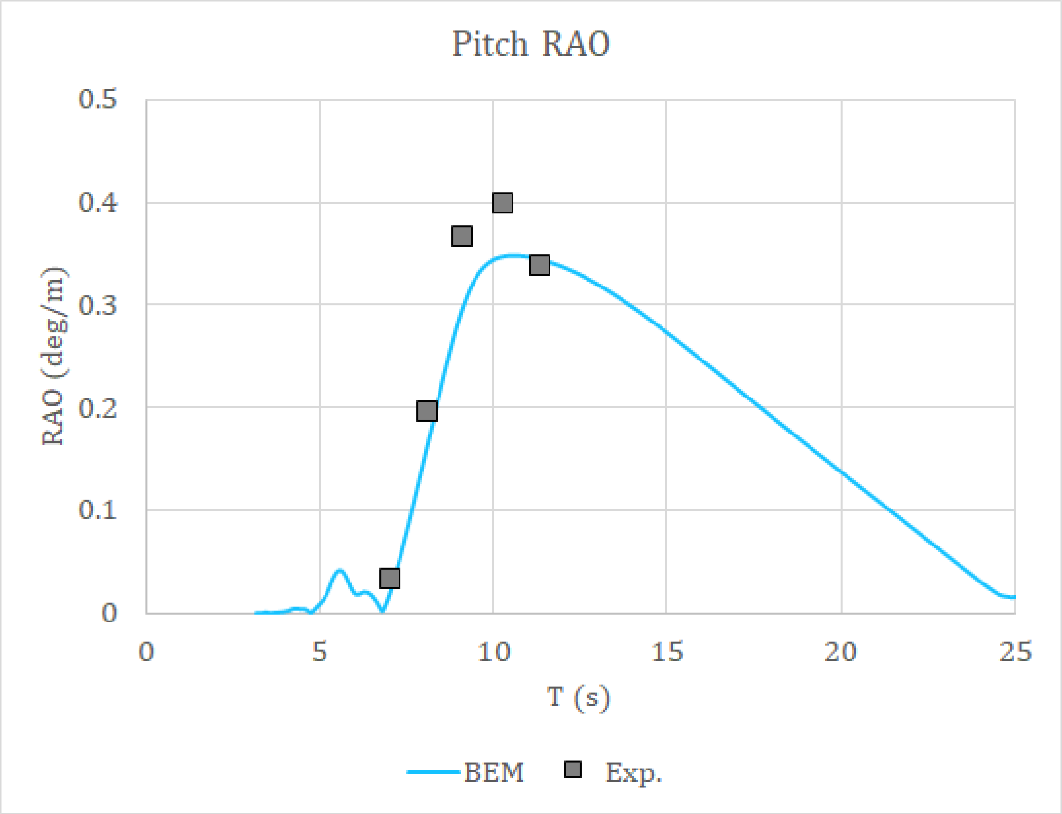

Once again, the comparisons between the numerical code and the experiment's results are satisfactory and so far, the source of the underestimation on the slow-drift responses for T = 10 s has not been identified yet.

5.3 Second-order Results

In this section, the most sensible results regarding forces and motions are presented in terms of mean and low-frequency forces.

5.3.1 Mean and Low-Frequency Forces

The fourth step was to compare the mean drift forces, which are crucial for the motions results. Regarding these comparisons, from Fig. 5.11, it can be inferred that FVM has presented very accurate results in relation to the fixed model tests, while, BEM results show larger deviations. The most critical one being observed for the wave period of, again, 10 s, when the predictions underestimate the measured loads in about 41% . On the other hand, at 11 s, the BEM code has overestimated the result by 78%.

It is important to notice that, qualitatively, these results, obtained from load cell measurements in captive model tests, are consistent with the differences noted in the mean offsets and slow-drift amplitudes in tests with moored models, as those already presented in Fig. 5.1 and 5.2. An advantage of the FVM features is that the forces can be divided into viscous and pressure parcels and the outcome is that the viscous parcels represent only 0.5% at maximum in these five simulations, hence, the viscous forces are not contributing for the mean drift forces values. This was expected due to the small steepness and KC numbers for these five waves. In fact, taking the column length as the reference for the KC, the higher waves in these tests corresponds to a KC of only 0.72.

Figure 5.11: Mean drift forces comparisons from regular waves at 180^o (Captive tests).

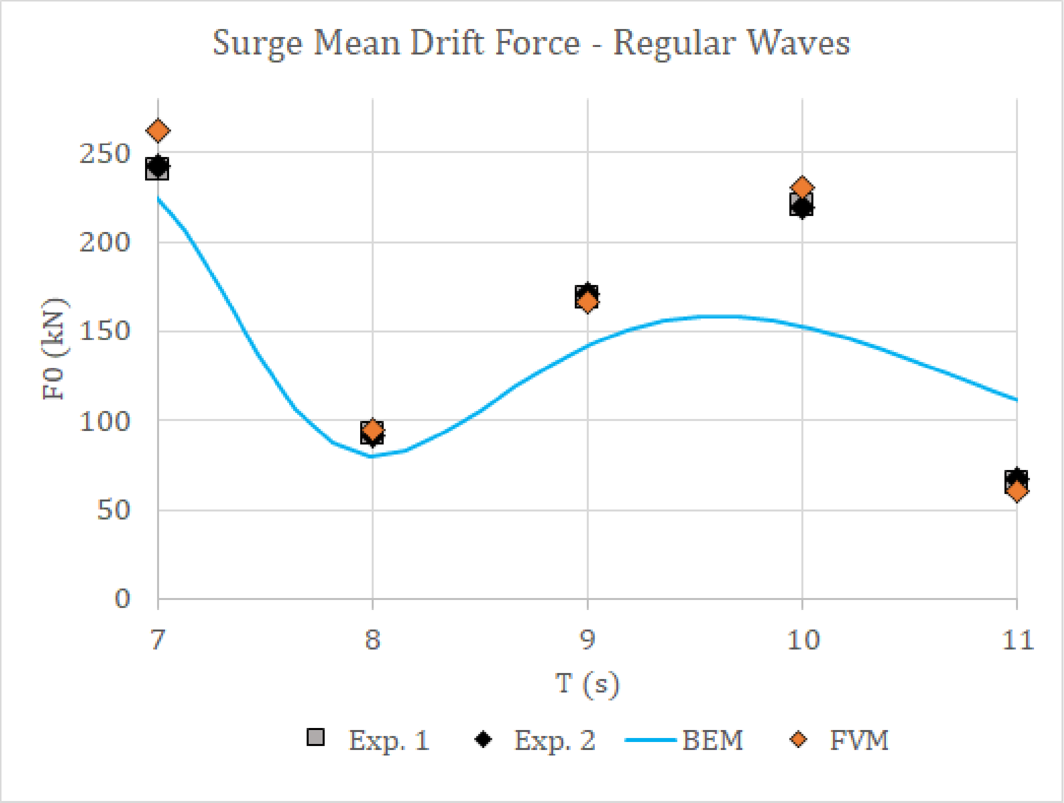

Regarding the low-frequency forces, they were obtained through the bichromatic waves described in Tab. 4.5. Figure 5.12 shows a similar behaviour to those from the mean drift forces in the regular waves, but with larger deviations at periods around BIC03 (Tm = 9.2 s). This is probably caused by this pair of periods having the component of 9.41 s that is closer to the 10 s period, and which is now known by having a numerical issue. In addition, for the period of 11 s, which was being overestimated by AQWA in the regular waves, is still overestimated, but with a smaller deviation.

Figure 5.12: Mean drift forces comparisons from bichromatics waves at 180^o (Captive tests).

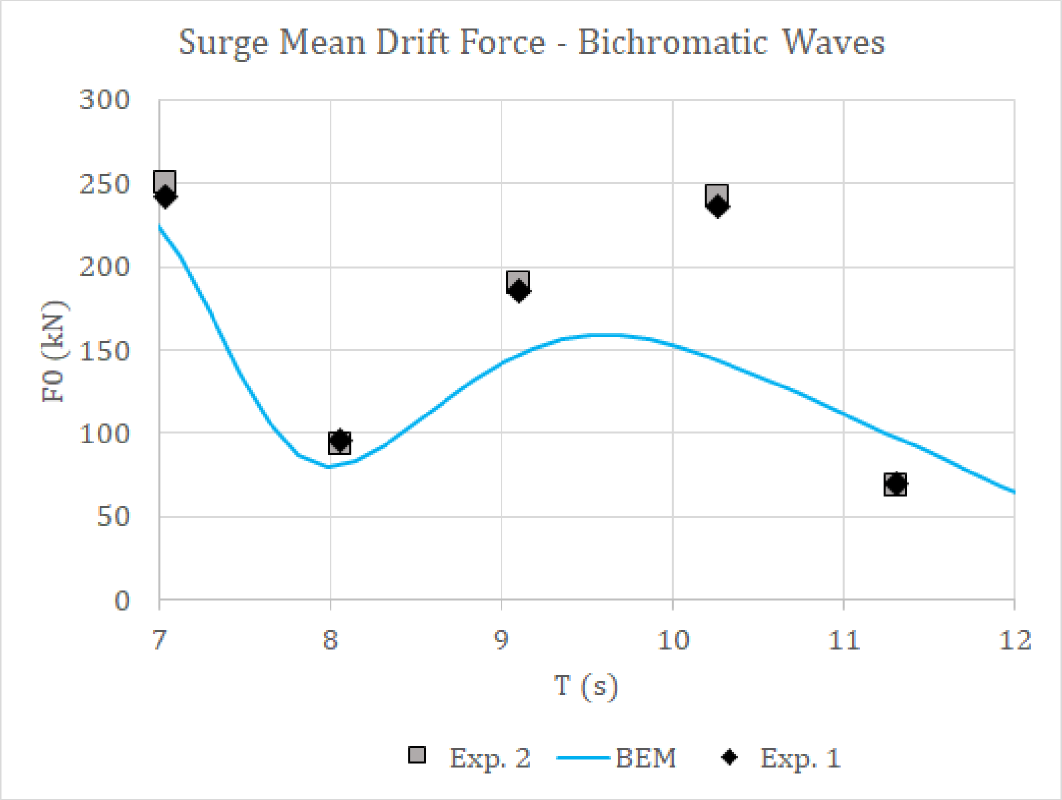

A remark regarding the previous section should be made here by stating that the differences presented in the fixed tests reinforce that the discrepancies observed in the first-order pitch motions are not the main source of errors in the mean and slow-drift force results, since even with the model fixed, large differences in the forces are observed. However, it is important to have in mind that along to the differences in first-order motions, the difference may increase further.

Now it is known that the deviation in the mean and slow-drift responses for T = 10 s is caused by the underestimation of the mean drift forces by the BEM code. But now, it rests to understand: why? The cylinder analysis performed on Section 3.6 may have provided a clue.

5.3.2 Free Surface Elevation Component

The fifth procedure was to isolate the forces components of the mean drift force. In order to understand why the potential code is presenting these errors, the free surface force parcel was computed as presented in Section 3.6. To guarantee the validity of this procedure, the first step was to compare the free surface elevations at the wave probes obtained from the experiments and by both numerical software, as Fig. 5.14 to 5.17 introduced by having Fig.

5.13 as reference. A fundamental information is that the same wave elevation analysis was performed with WAMIT and compared to AQWA, and the largest discrepancies between them was only 3% in the wave elevation amplitude.

Figure 5.13: Columns number representation.

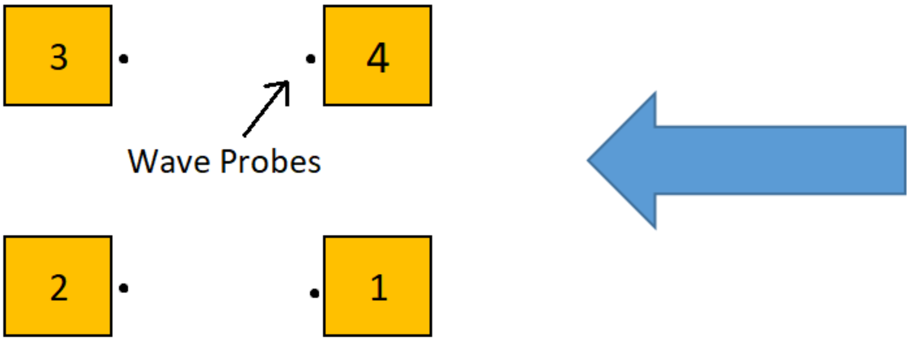

Figure 5.14: Columns number 1 wave elevation comparison in regular waves at 180^o (Captive tests).

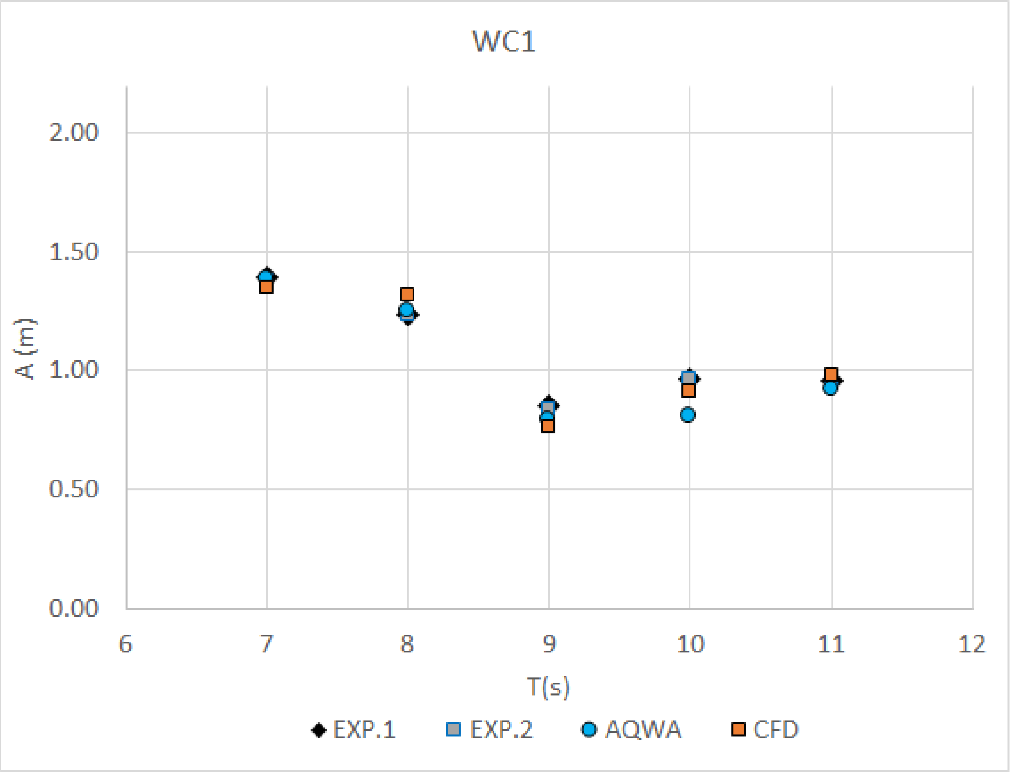

Figure 5.15: Columns number 2 wave elevation comparison in regular waves at 180^o (Captive tests).

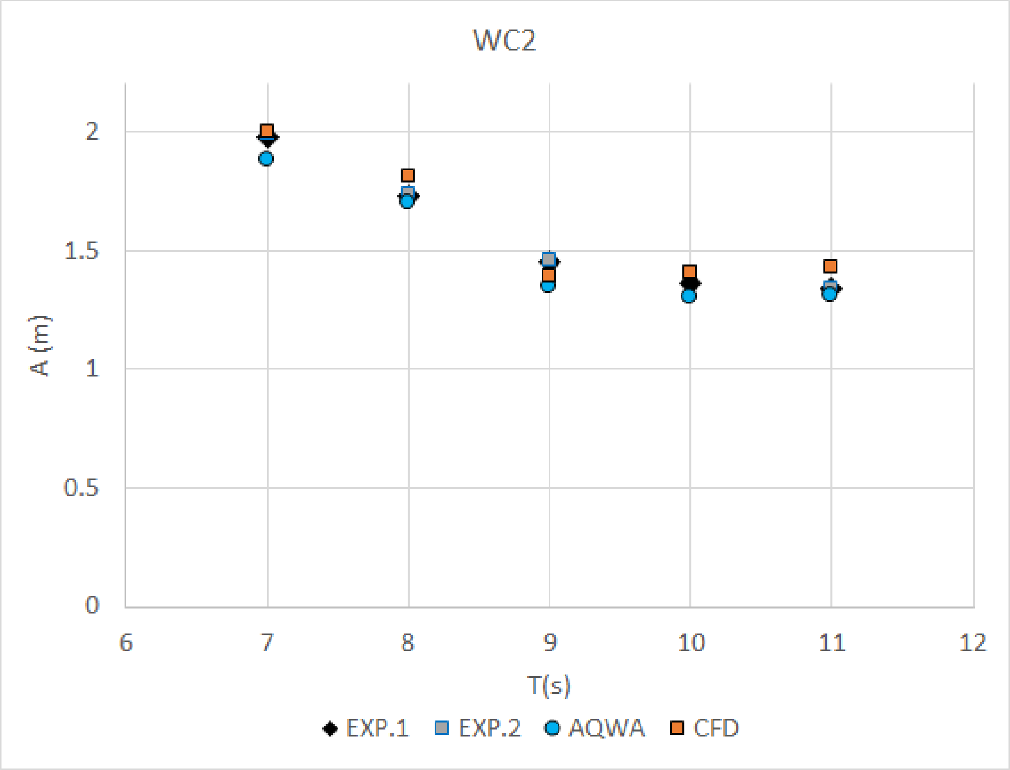

Figure 5.16: Columns number 3 wave elevation comparison in regular waves at 180^o (Captive tests).

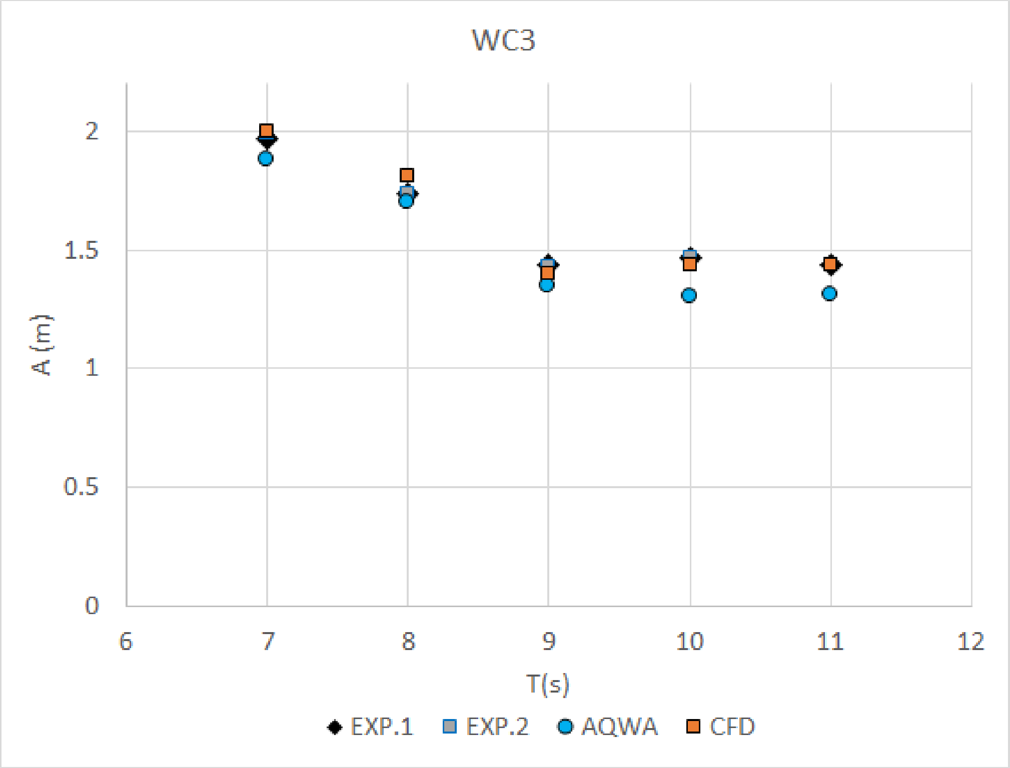

Figure 5.17: Columns number 4 wave elevation comparison in regular waves at 180^o (Captive tests).

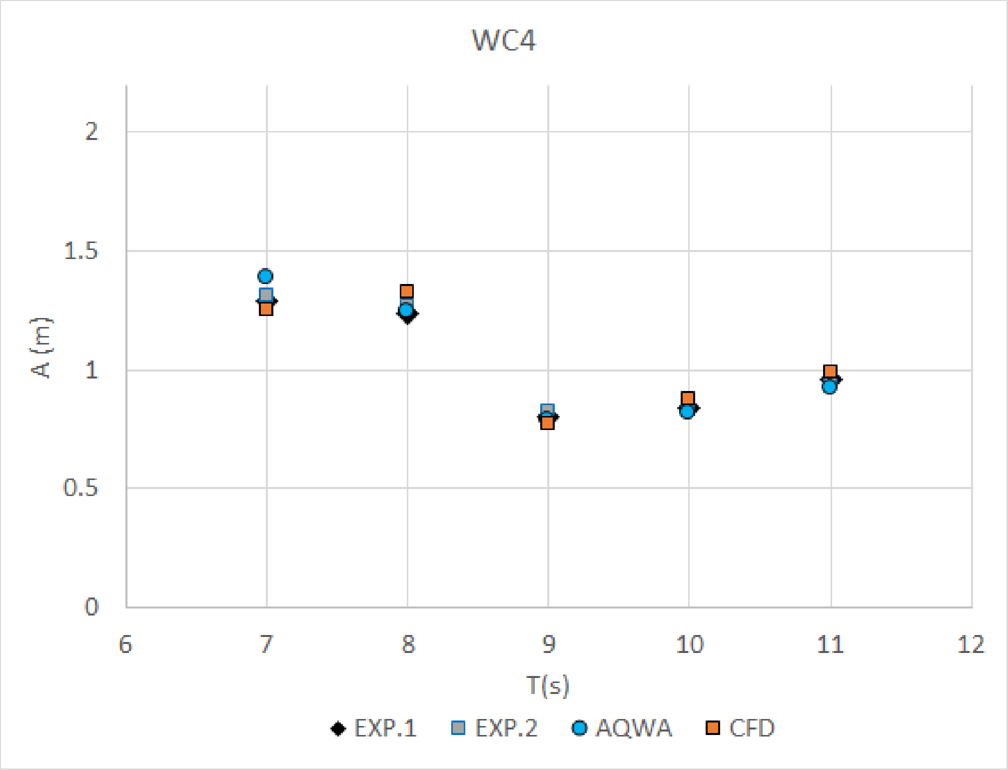

Two main points are noticed in these figures. The first remark is that the experiments are not symmetric at, again, 10 s period with respect to the y axis as it was supposed to be. These differences, that can reach 24%, might be caused by slightly asymmetries during the model set-up, however, they also appear in the FVM results, which have a perfect symmetric geometry. A second point is that AQWA outcomes are totally symmetric, as expected, but it is not representing the results well precisely at 10s, where the prediction is smaller than the experiments in two diagonally positioned probes (WP1 and WP3). On the other hand, Fluent results have presented very good agreements with the experiments.

An example of the wave field comparison between AQWA and Fluent is provided for H = 2 m, T = 8 s and 157.5^o in Fig. 5.18, in which it is possible to observe that the wave field between both numerical codes are very similar in general, but mainly at column number 3, the BEM code is not recovering the wave amplitudes well enough.

Figure 5.18: Wave elevation field comparison between FVM (Fluent) and BEM (AQWA) for H = 2 m, T = 8 s and 157.5^o (Captive tests).

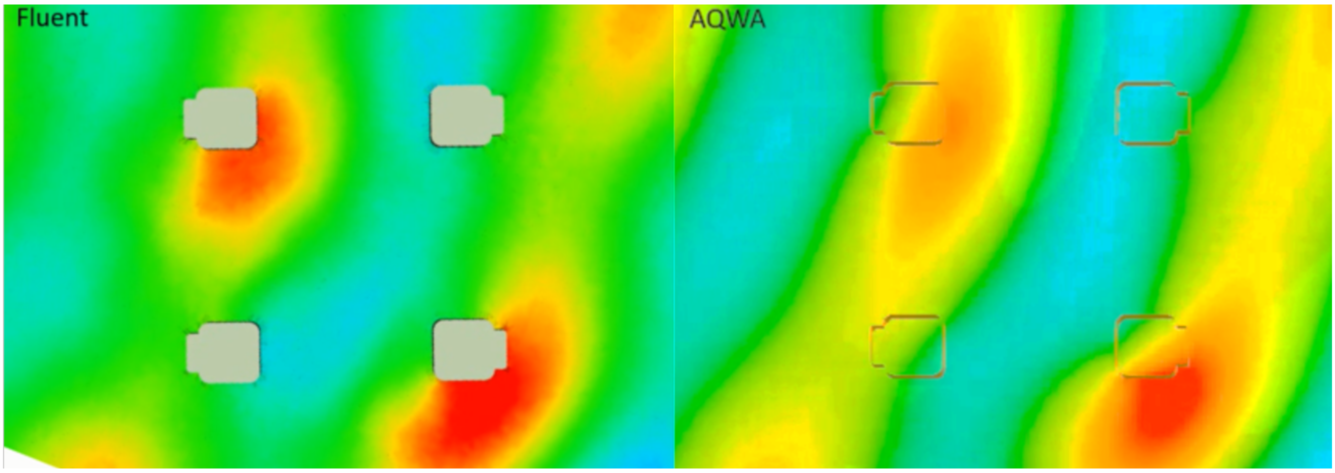

With the FVM results validated, 16 points per column, in addition to four central points between the columns (Fig. 5.19) were taken both in Fluent and AQWA codes and compared against each other. Then, the free surface elevation component of the mean drift forces could be computed through results from each software following a post-processing procedure as presented in Section 3.6 with adaptations for this geometry.

Figure 5.19: Wave probes comparison in the columns and centers.

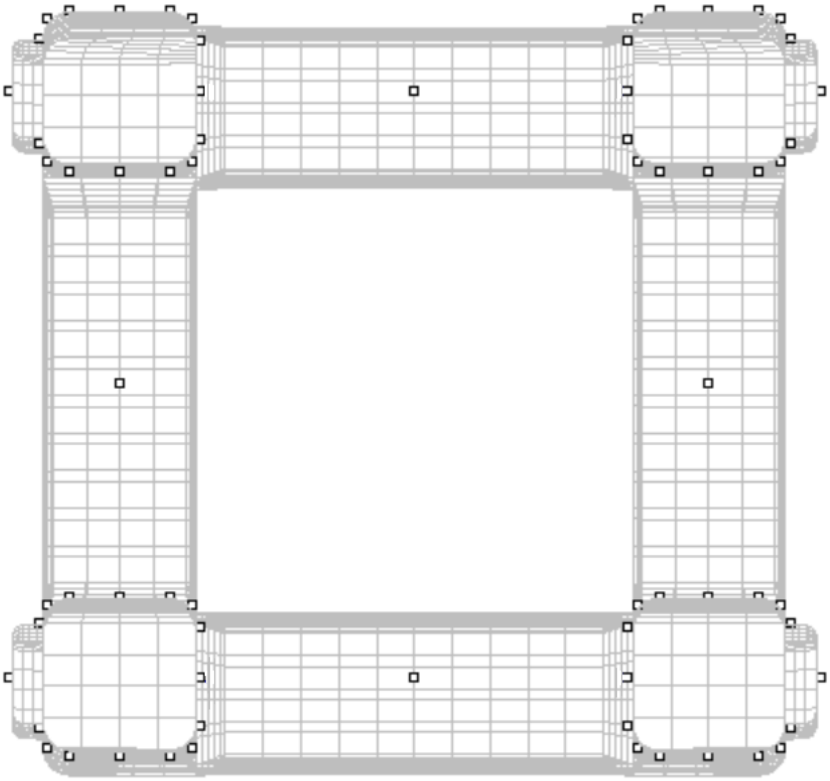

Figures 5.20 to 5.31 present the free surface elevation around the columns, at the centers between the columns and at the wave probes by AQWA and by the Fluent. In addition, the magnitude of free surface elevation component of the mean drift force is presented on the center of each column. The differences in terms of percentage of the FVM values in relation to the BEM values are also presented.

Figure 5.20: Wave elevation amplitude (in m) and force parcel comparison between FVM and BEM for a regular wave with T = 7 s and 180^o heading.

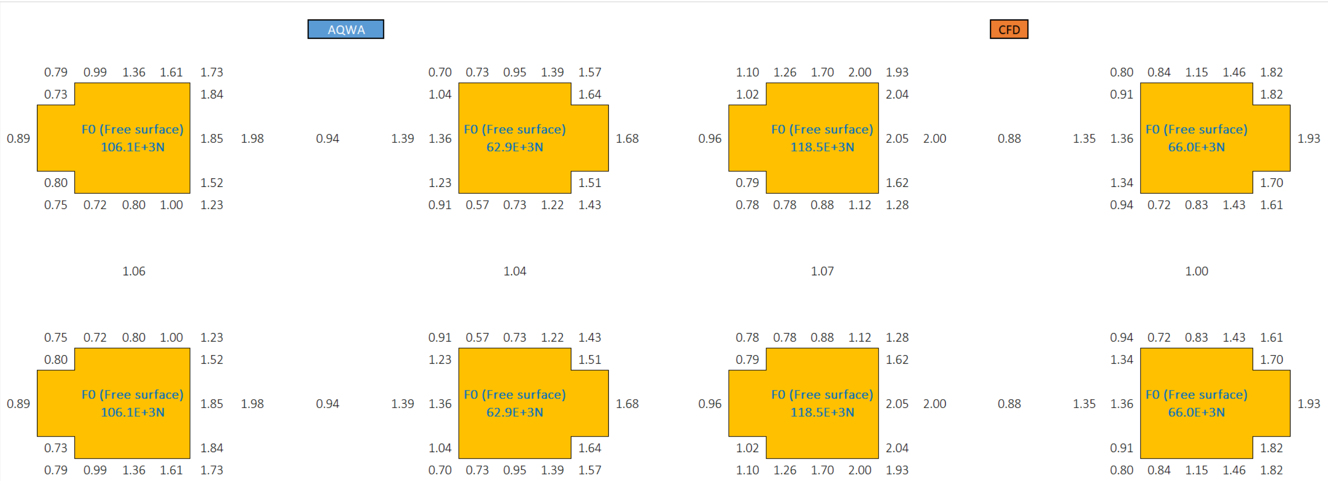

Figure 5.21: Percentual differences in wave elevation amplitude and force parcel from FVM in relation to BEM with T = 7 s and 180^o heading.

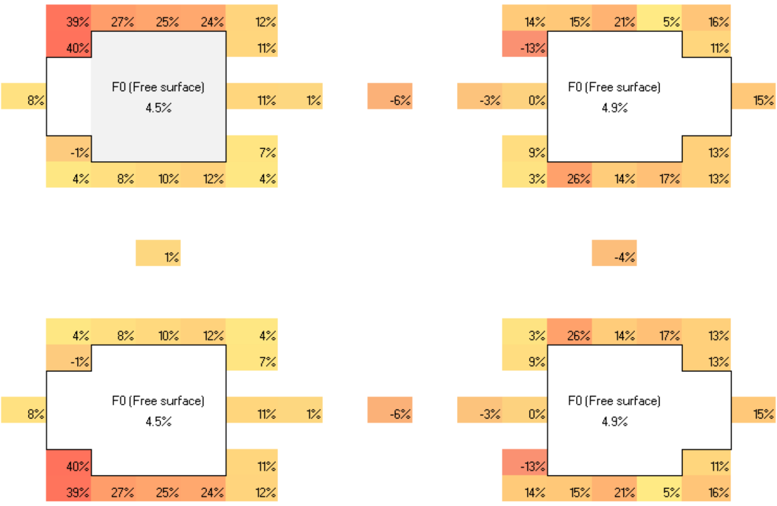

For the T = 7 s case, there are large differences in the outboard aft columns near to the blisters; however, at the wave probes and the centers between the columns, there are no significant divergences. Even with these differences in the wave field, the forces at each column are only 5% higher in the FVM than BEM, due to the larger deviations are located in regions that are less important to the surge forces.

Figure 5.22: Wave elevation amplitude (in m) and force parcel comparison between FVM and BEM for a regular wave with T = 8 s and 180^o heading.

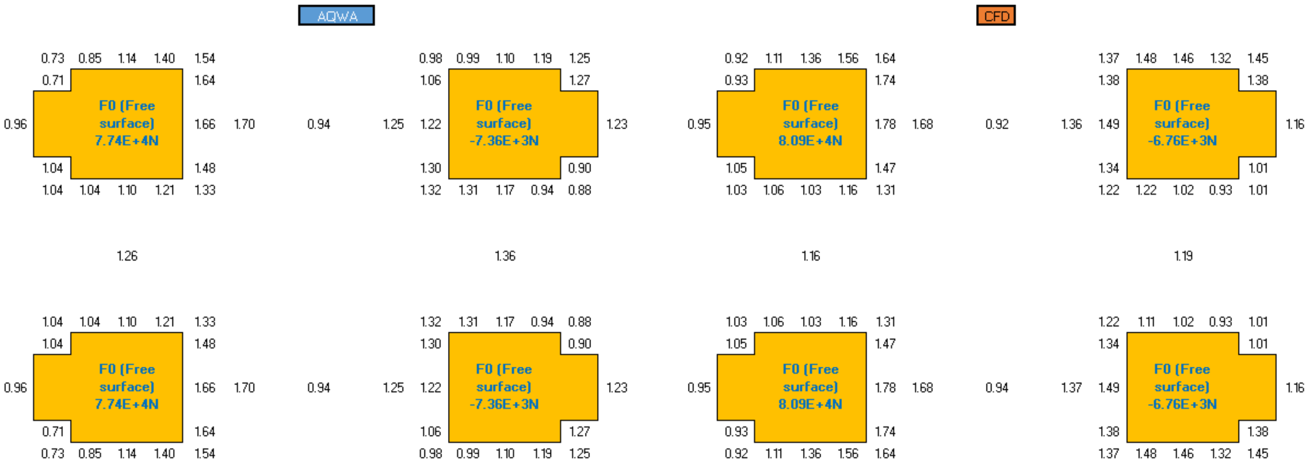

Figure 5.23: Percentual differences in wave elevation amplitude and force parcel from FVM in relation to BEM with T = 8 s and 180^o heading.

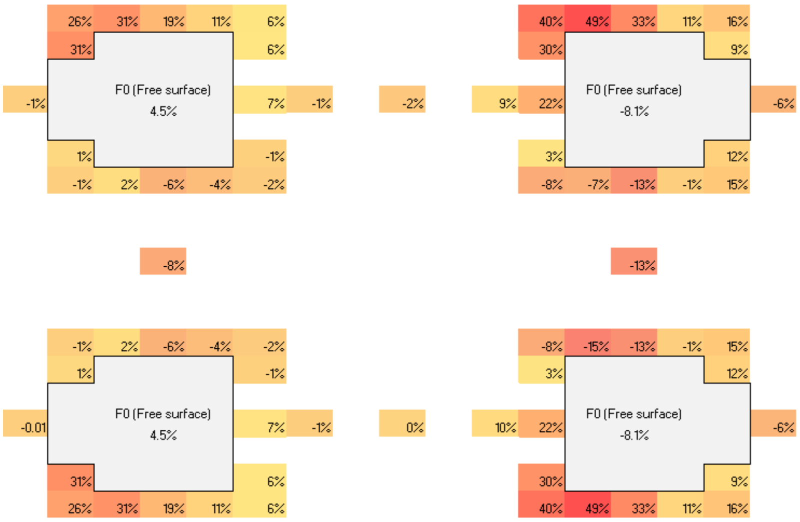

For the regular wave of T = 8 s, the differences in the wave probes and centers regions are not that large, nevertheless, at the outboard columns the differences can achieve up to 49%. Even with these large differences in the free surface elevations, the AQWA values are much smaller in some regions and larger in others, which provides a compensation in the force parcel. Hence, for this period the free surface force parcel in the mean drift force is not compromised by the wave elevation not being well estimated by BEM.

With the purpose of evaluating how much the steepness of the wave interferes on the wave field prediction, the same T = 8 s wave was computed with a H = 1 m instead of H = 2 m as before. Basically, the assessment here is the direct comparison between a 1.01% and 0.50% steepness numerical scenario. Figure 5.24 and 5.25 provides Fluent and AQWA wave elevation prediction for the smaller steepness case and shows that the differences which were up to 49% before are 24% in maximum now. The differences in the total free surface parcel force was small as well, only about 4.0%. Therefore, it can be concluded that there is dependence on the steepness of the numerical codes on the wave field computation. Even 1% being considered a small steepness, the numerical results were significantly closer when the steepness was reduced by half.

Figure 5.24: Wave elevation amplitude (in m) and force parcel comparison between FVM and BEM for a regular wave with T = 8 s and 180^o heading (half steepness).

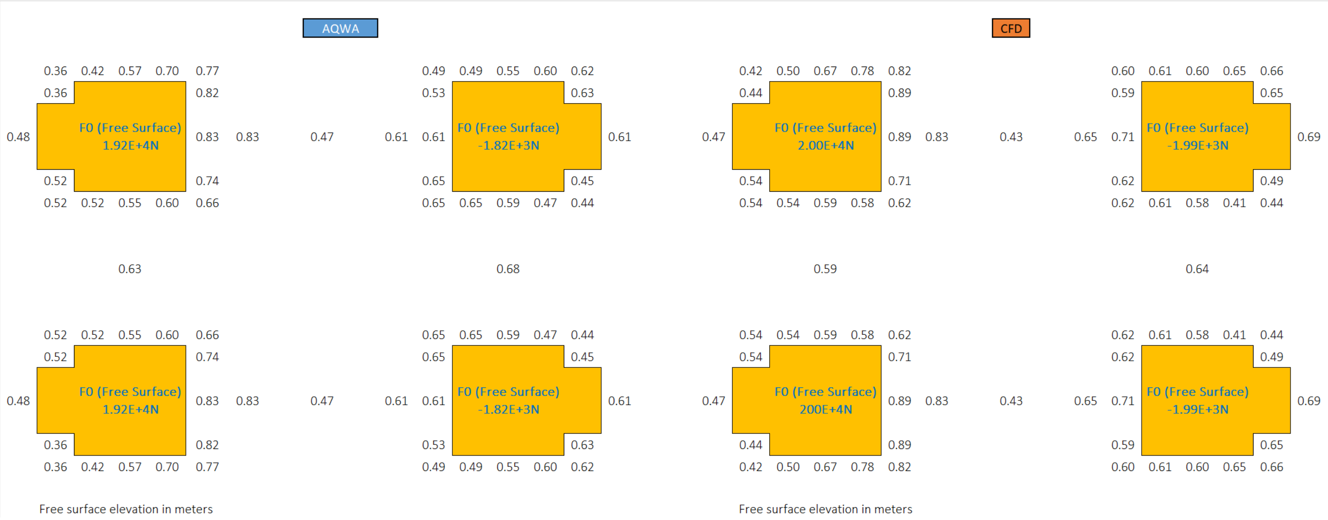

Figure 5.25: Percentual differences in wave elevation amplitude and force parcel from FVM in relation to BEM with T = 8 s and 180^o heading (half steepness).

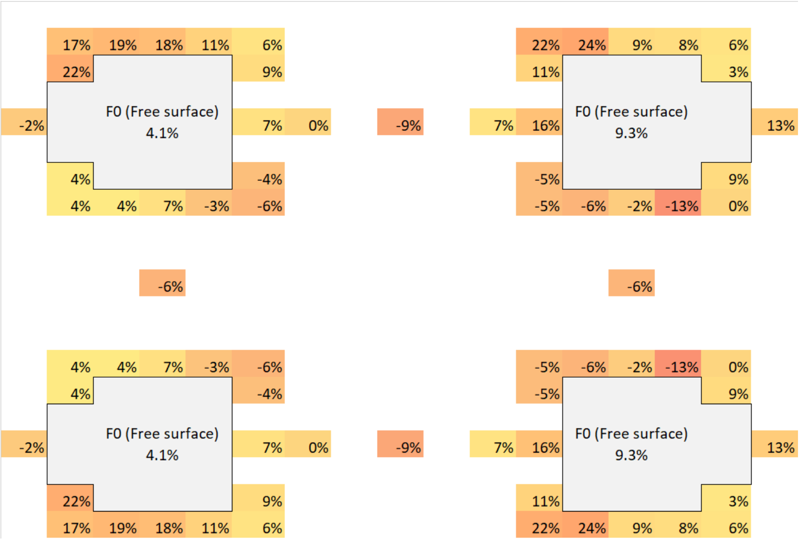

Figure 5.26: Wave elevation amplitude (in m) and force parcel comparison between FVM and BEM for a regular wave with T = 9 s and 180^o heading.

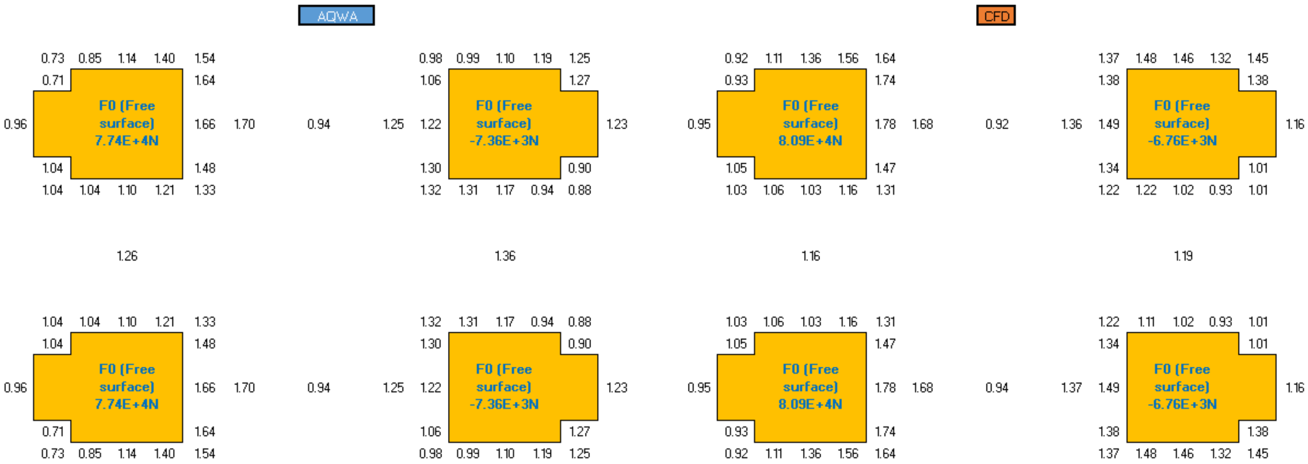

Figure 5.27: Percentual differences in wave elevation amplitude and force parcel from FVM in relation to BEM with T = 9 s and 180^o heading.

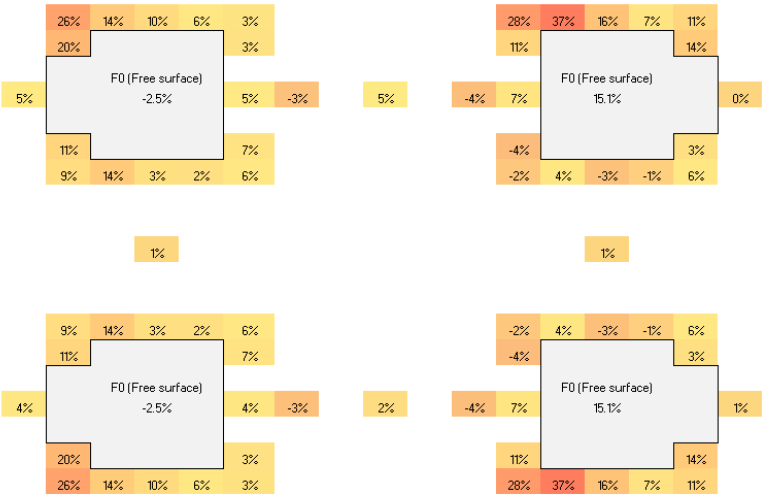

Regarding the case with regular wave T = 9 s, the differences in the wave elevation are smaller than for the T = 8 s, but they are still significant in the regions near to the outboard of the blister. The differences in the forces caused by the divergences in the wave surface levels are about −2% in the aft columns and 15% in the forward columns.

Figure 5.28: Wave elevation amplitude (in m) and force parcel comparison between FVM and BEM for a regular wave with T = 10 s and 180^o heading.

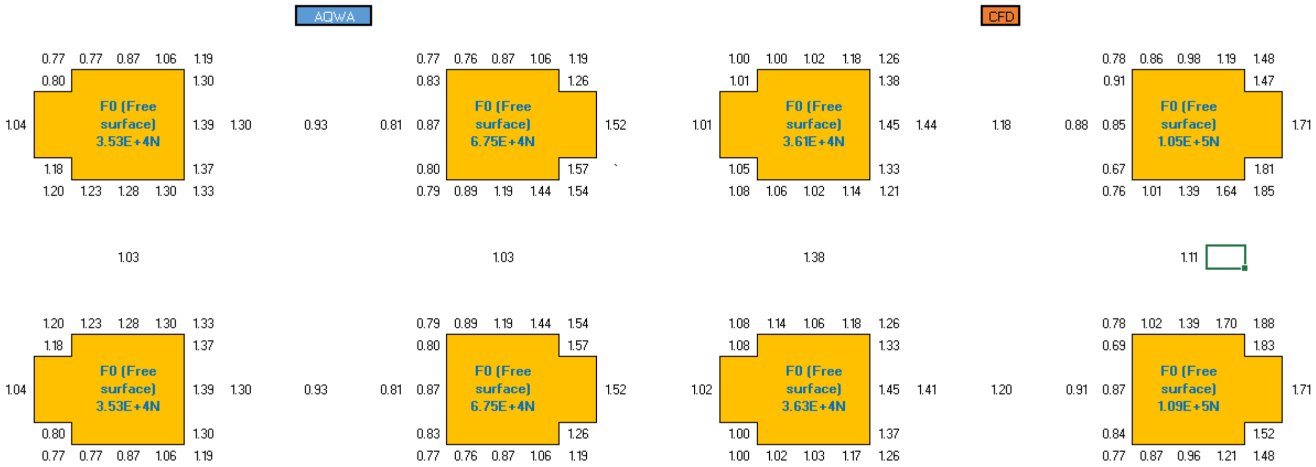

Figure 5.29: Percentual differences in wave elevation amplitude and force parcel from FVM in relation to BEM with T = 10 s and 180^o heading.

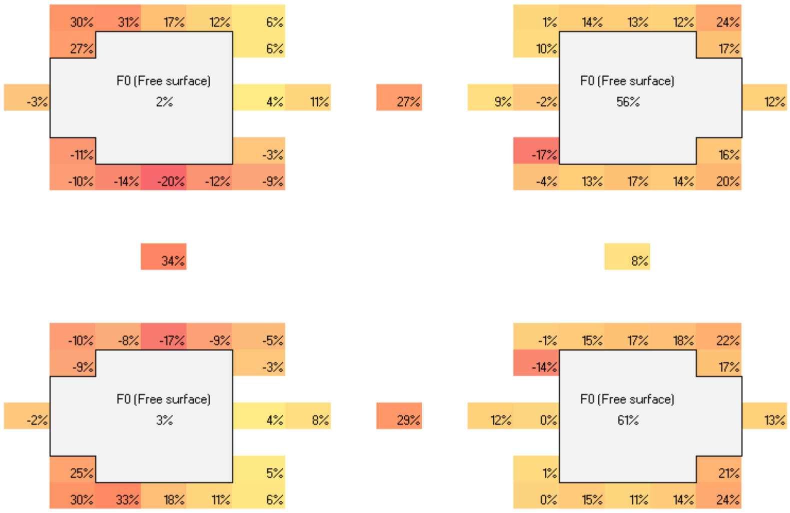

For the T = 10 s case, FVM values are larger in most of the regions around the bow columns, which are actually the biggest contributors to the force parcel, resulting in a force contribution 56% and 61% larger than the one provided by BEM. Another interesting point is that not only are the elevation around the columns divergent, the elevations between the columns along the wave direction are also very large, about 30%. These results actually raise the supposition that a near-trapped wave may be occurring at this period. Another sign that this phenomenon may be appearing is that the wavelength at this period is similar to the distance between the platform columns (outboard borders).

Figure 5.30: Wave elevation amplitude (in m) and force parcel comparison between FVM and BEM for a regular wave with T = 11 s and 180^o heading.

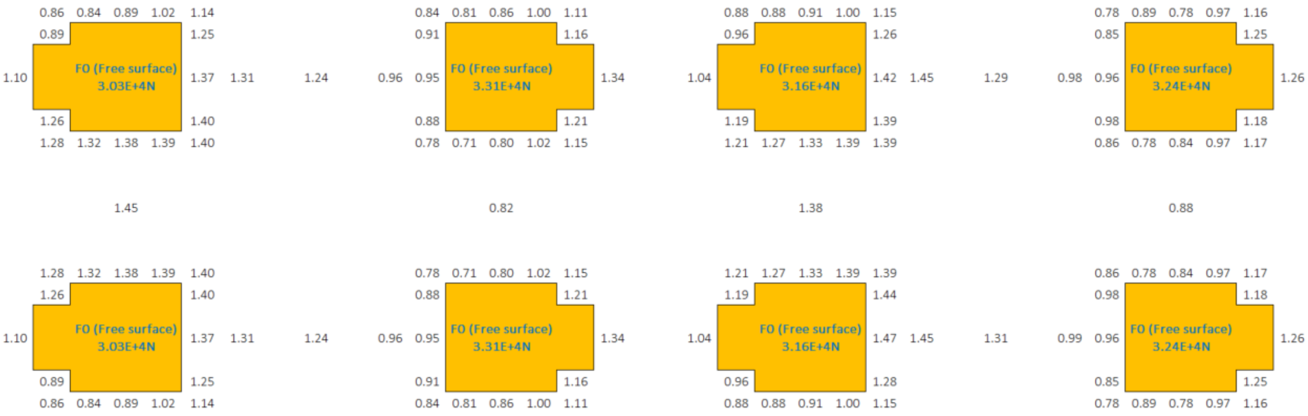

Figure 5.31: Percentual differences in wave elevation amplitude and force parcel from FVM in relation to BEM with T = 11 s and 180^o heading.

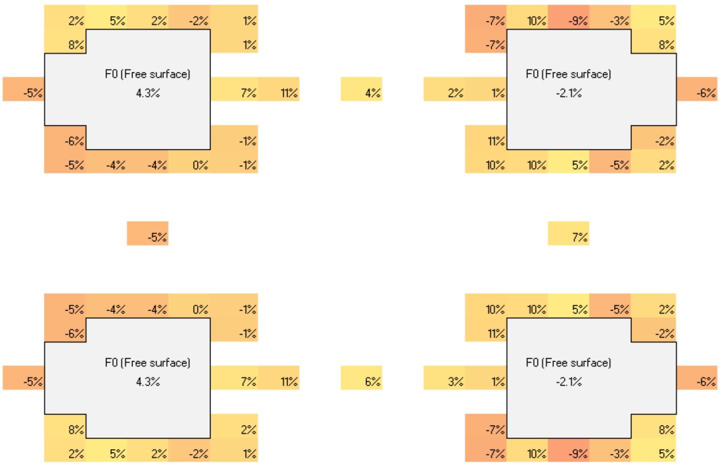

Regarding the T = 11 s case, all the differences between AQWA and Fluent are considerably smaller, less than 10% around the columns, as well as the differences in the force parcel in each column. The differences in the probes between the columns are practically null as well. A possibility for these good pictures is related to the small steepness of this case, however, the case of T = 10 s also presents a small steepness and the results are not good, which again indicates that something else is occurring in that period.

In general, BEM codes present difficulties in estimating the wave field in this platform. Nevertheless, in the majority of the periods, these differences are not large enough to compromise the mean drift forces and mean and slow-drift motions of it.

Table 5.1 summarizes the mean drift total forces results from Fig. 5.11 with the mean drift (free surface parcel) from Fig. 5.20 to 5.30 for AQWA and Fluent results. This table also presents the difference on the load when the free surface component is computed with the elevations obtained from both software the results and how correlated they are with the deviations on the total mean drift forces. In almost all cases, the divergence in the free surface elevation component is almost the same as the total mean drift. The only case that does not imply that the wave elevations at the columns are causing the differences in the total mean drift forces is T = 11 s, in which BEM is providing larger results. Once again, it is important to have in mind both numerical and experimental should account for uncertainties ranges around the resultant values.

Table 5.1: Force elevation parcel and total mean drift force for the regular waves at 180^o.

ID	T (s)	AQWA	CFD	Difference (kN)
Force Elevation Parcel (kN)	7.0	338	369	31
Total Mean Drift (kN)	7.0	230	262	32
Force Elevation Parcel (kN)	8.0	83	95	12
Total Mean Drift (kN)	8.0	140	148	8
Force Elevation Parcel (kN)	9.0	203	216	13
Total Mean Drift (kN)	9.0	143	166	23
Force Elevation Parcel (kN)	10.0	205	288	83
Total Mean Drift (kN)	10.0	151	235	84
Force Elevation Parcel (kN)	11.0	127	128	1
Total Mean Drift (kN)	11.0	90	61	-29

Therefore, it is possible to conclude that the BEM code is not able to capture the mean drift loads for T = 10 s mainly due to a poor estimation of the free surface elevation field that carry out to the underestimation of the free surface component, which, in its turn, is the dominant component in this force (as it was already discussed in Section 3.6). In order to provide more details for this particular wave period, the wave elevation field from Fluent and AQWA were taken along one complete cycle of the regular wave, in time-steps of 1 s, as it is presented in Fig. 5.32 to 5.41.

Figure 5.32: Wave elevation field comparison between BEM and the FVM for a regular wave with T = 10 s and 180^o heading at 1s time step.

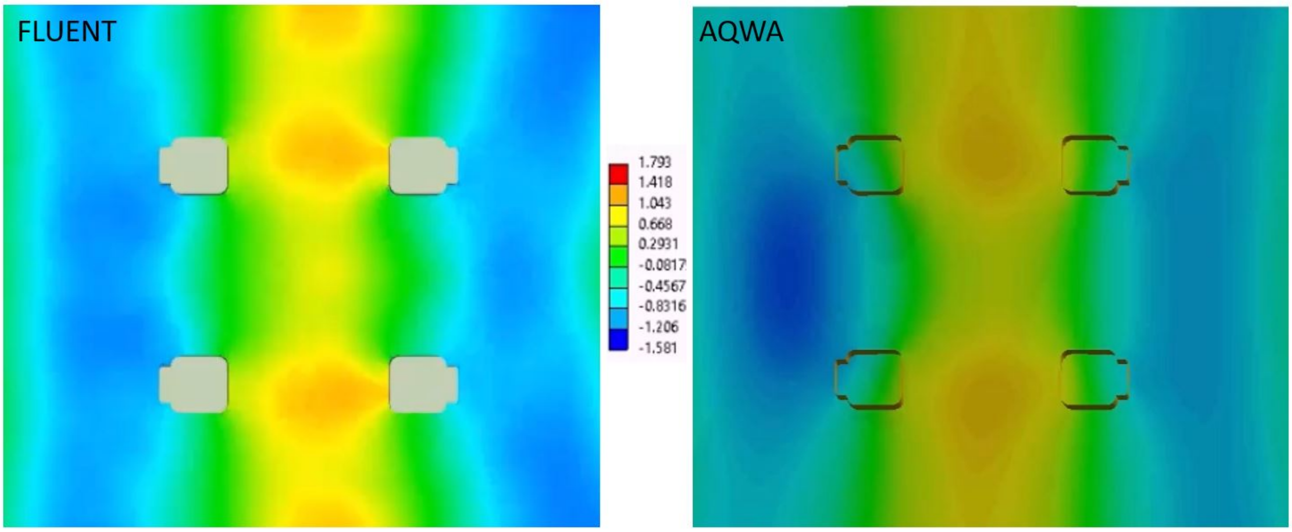

Figure 5.33: Wave elevation field comparison between tBEM and the FVM for a regular wave with T = 10 s and 180^o heading at 2s time step.

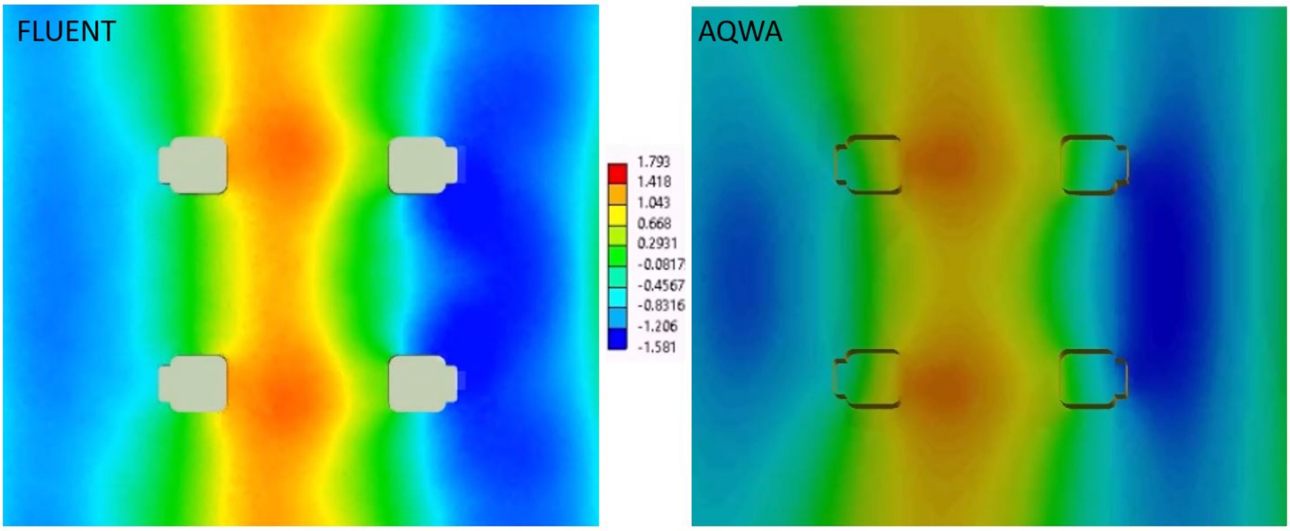

Figure 5.34: Wave elevation field comparison between BEM and the FVM for a regular wave with T = 10 s and 180^o heading at 3s time step.

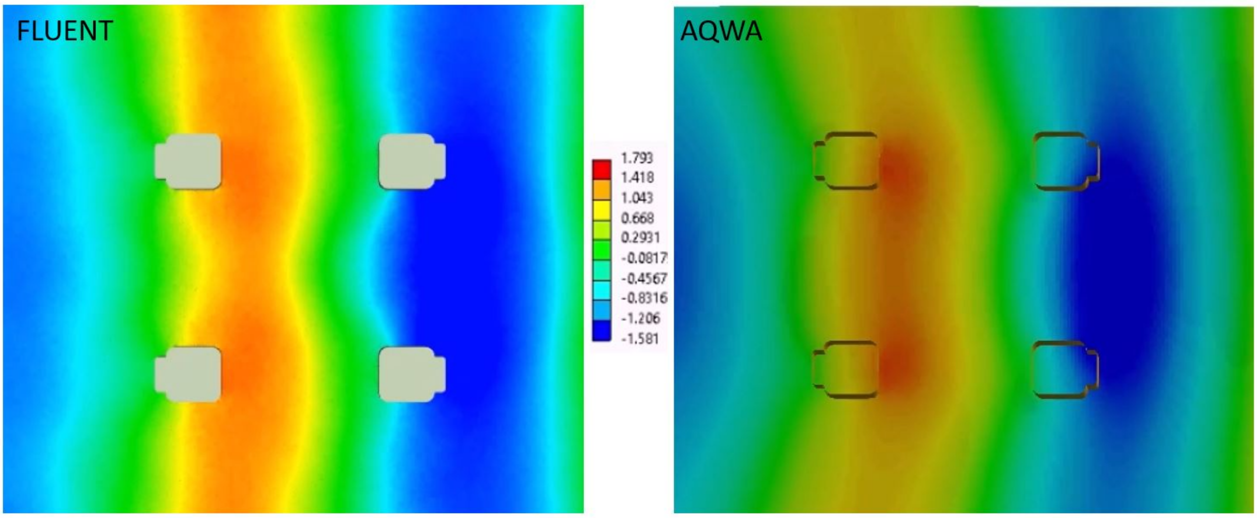

Figure 5.35: Wave elevation field comparison between BEM and the FVM for a regular wave with T = 10 s and 180^o heading at 4s time step.

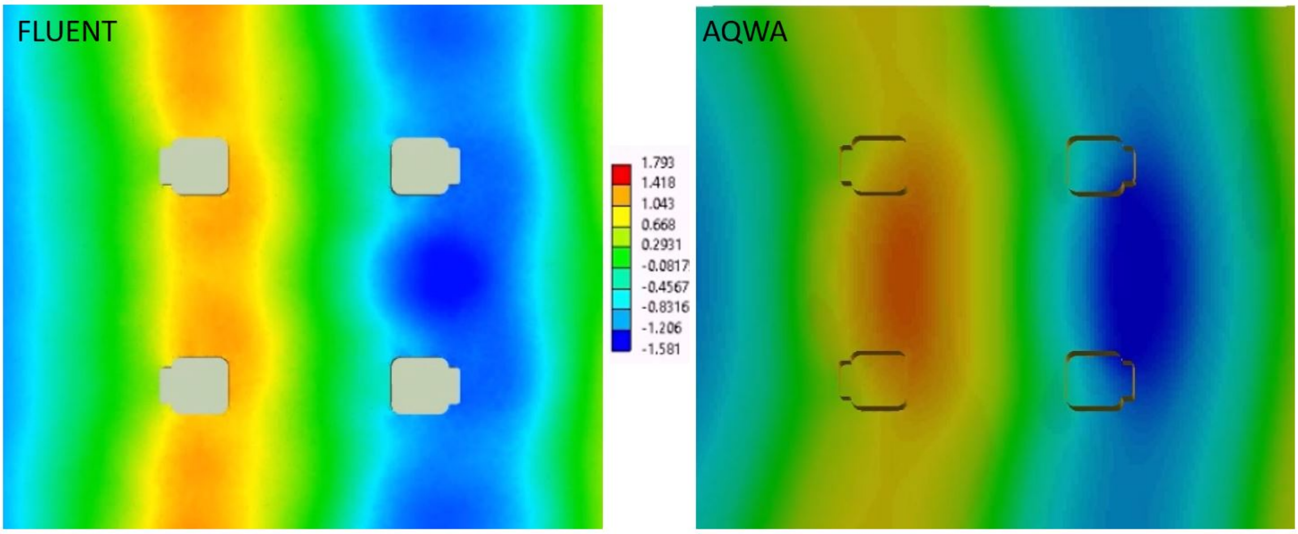

Figure 5.36: Wave elevation field comparison between BEM and the FVM for a regular wave with T = 10 s and 180^o heading at 5s time step.

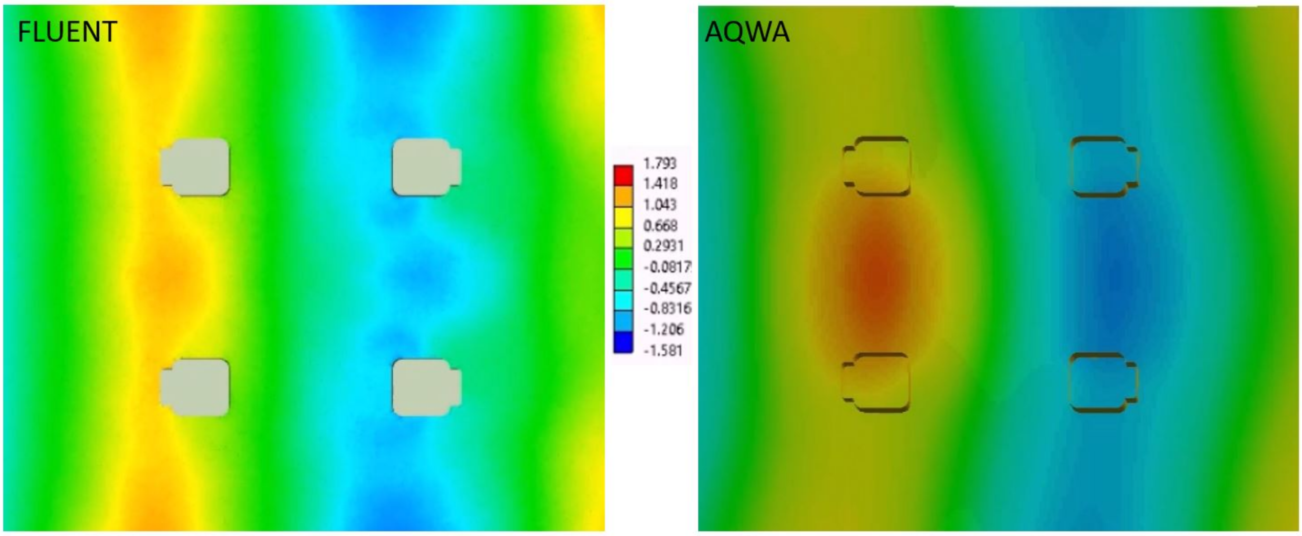

Figure 5.37: Wave elevation field comparison between BEM and the FVM for a regular wave with T = 10 s and 180^o heading at 6s time step.

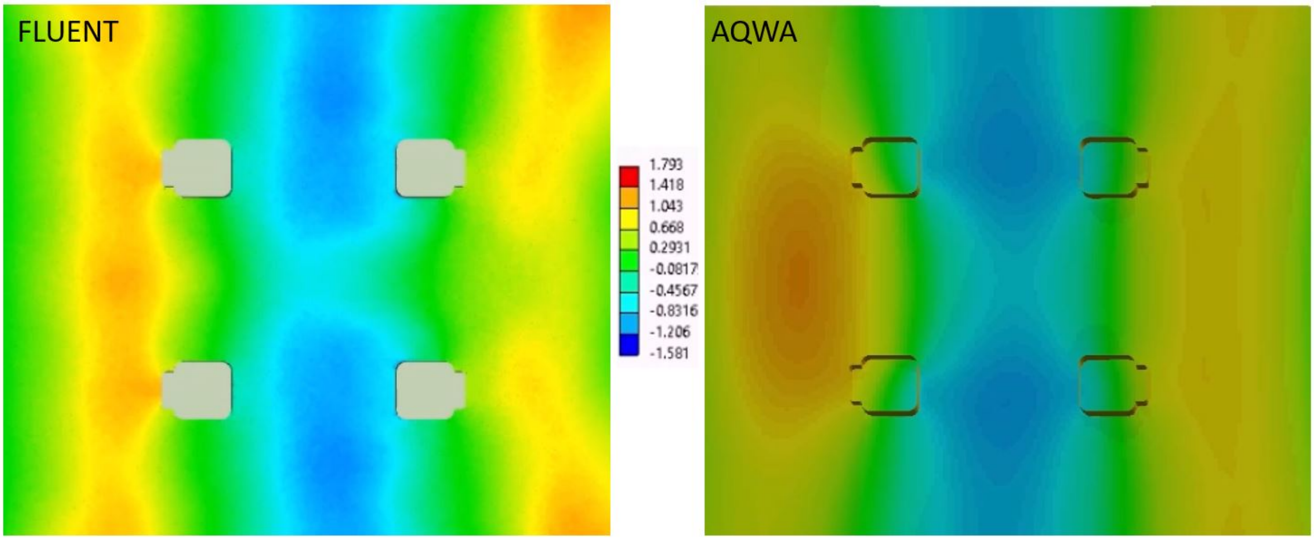

Figure 5.38: Wave elevation field comparison between BEM and the FVM for a regular wave with T = 10 s and 180^o heading at 7s time step.

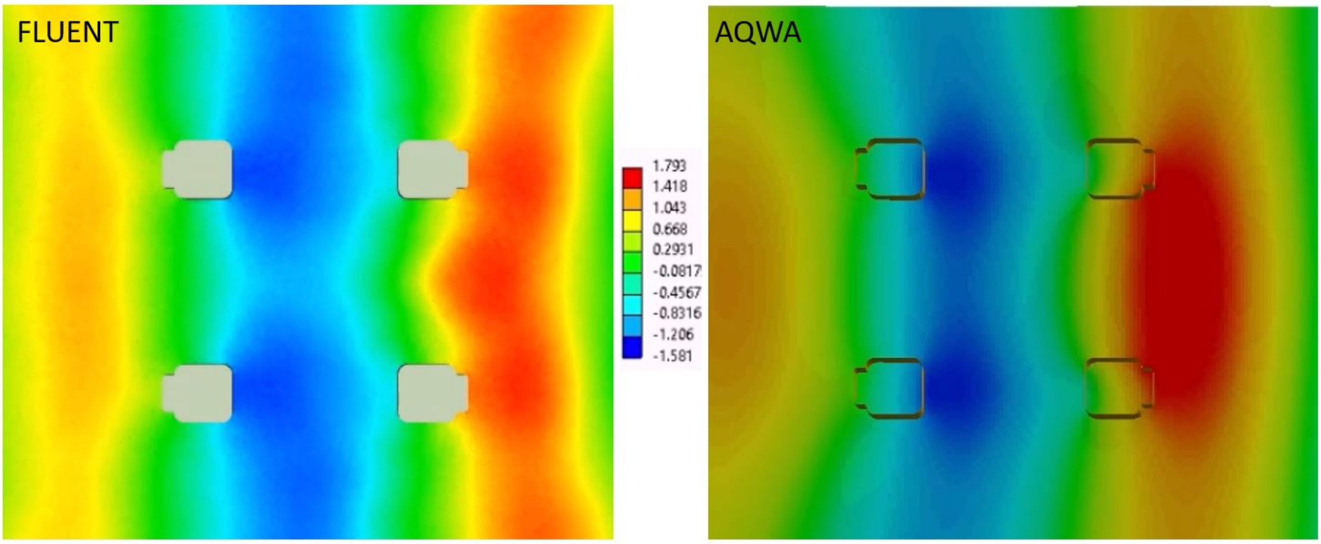

Figure 5.39: Wave elevation field comparison between BEM and the FVM for a regular wave with T = 10 s and 180^o heading at 8s time step.

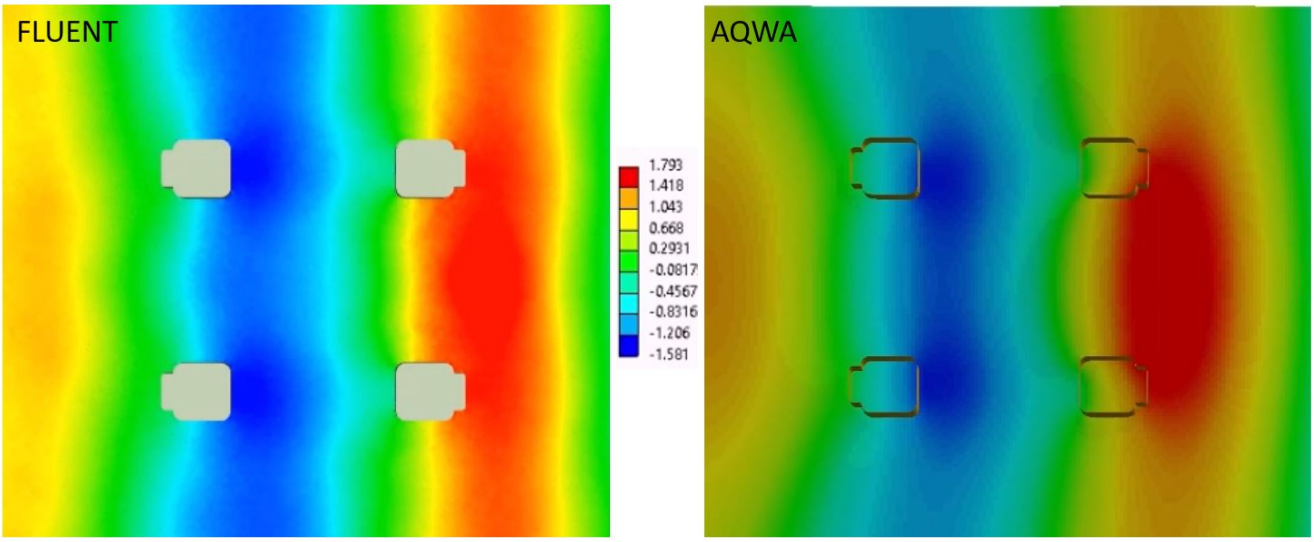

Figure 5.40: Wave elevation field comparison between BEM and the FVM for a regular wave with T = 10 s and 180^o heading at 9s time step.

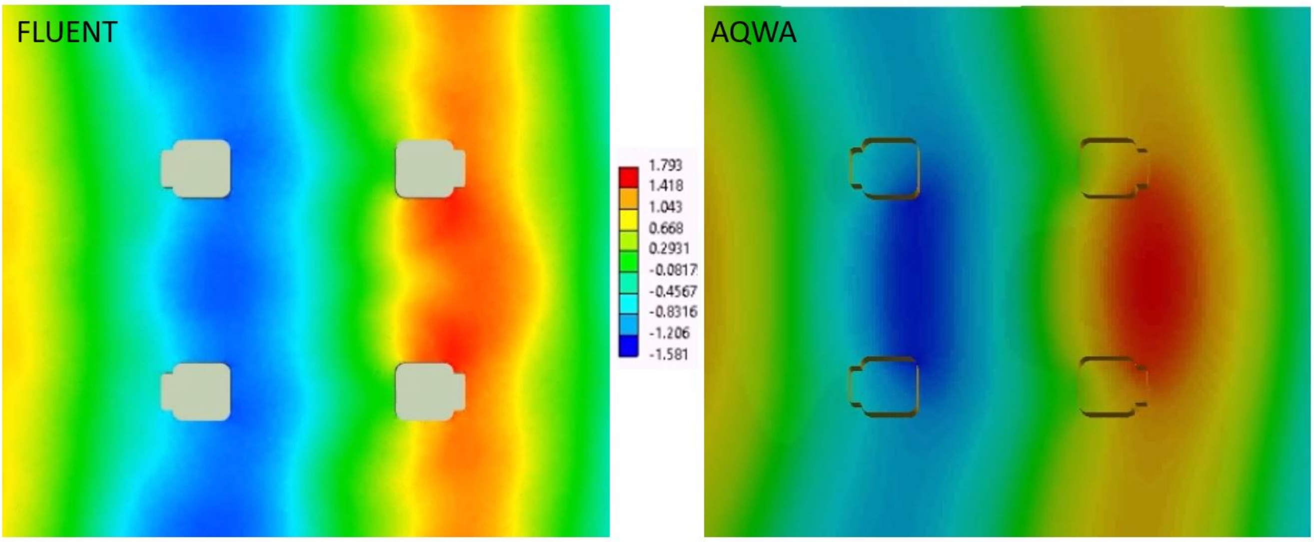

Figure 5.41: Wave elevation field comparison between BEM and the FVM for a regular wave with T = 10 s and 180^o heading at 10s time step.

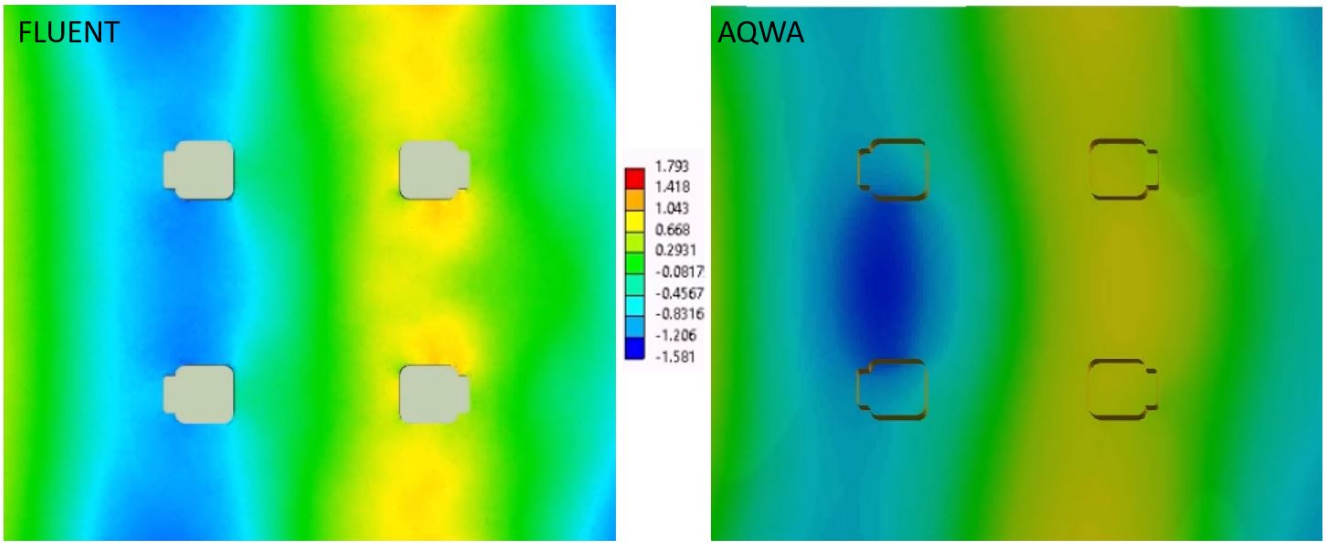

A first aspect to be noticed is that the waves crests and troughs in Fluent are pronounced not only between the columns as it is on AQWA, but also outboard the columns as it is shown in all the 10 time steps. Another point is that in Fig. 5.32 and 5.33, the wave elevation in the center of the figures is higher in Fluent than in AQWA. Further in Fig. 5.37 and 5.38, it is possible to notice that the valley in the center of the figures is larger in AQWA than in Fluent, as if there was a more intense wave interference effect in that region. Fig. 5.34, Fig. 5.35, Fig. 5.36, Fig. 5.37, Fig. 5.38 and Fig. 5.40 shows a more pronounced wave along the x-axis between the starboard/portside columns in Fluent than in the potential code. The last observation is that the wave elevation is also more pronounced along the x-axis between the aft/bow starboard and portside columns.

Going further into the investigation of the errors in the T = 10 s and 180^o case, the same period and wave height were also evaluated for the 157.5^o heading scenario. Figure 5.42 introduces the comparisons between the experiments and AQWA for the five periods and an additional Fluent run was performed for T = 10 s. For this heading, all the AQWA results are in much better agreement with the experiment.

Figure 5.42: Mean drift forces comparisons from regular waves at 157.5^o (Captive tests).

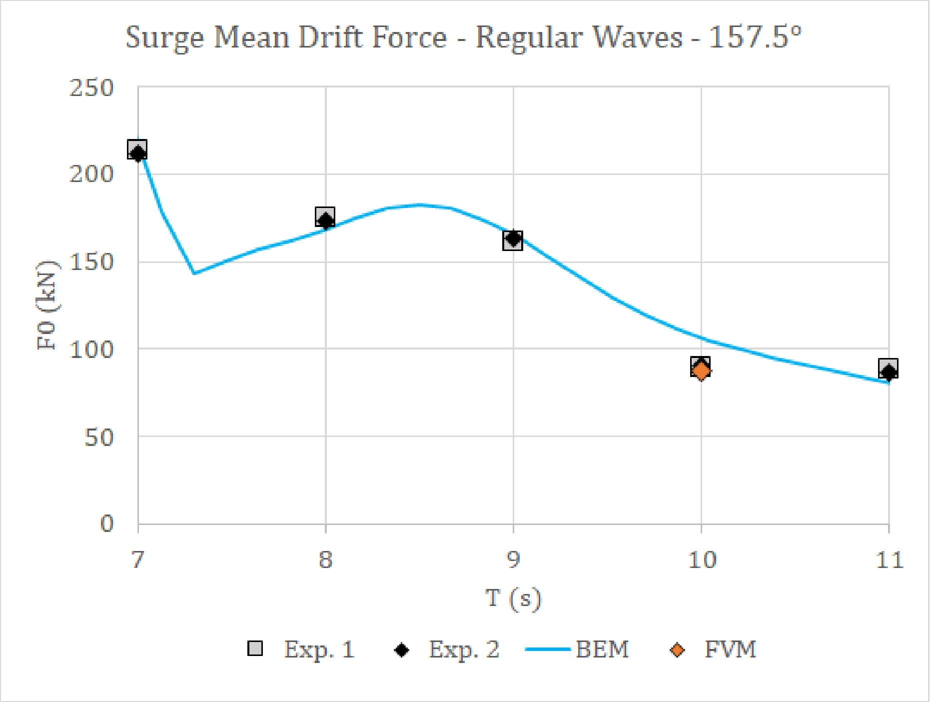

Even deeper analysis were performed with the wave elevations from AQWA and FVM were also compared at the 157.5^o heading, see Fig. 5.43 and **??**.

Figure 5.43: Wave elevation amplitude and force parcel from BEM and FVM with T = 10 s and 157.5^o heading.

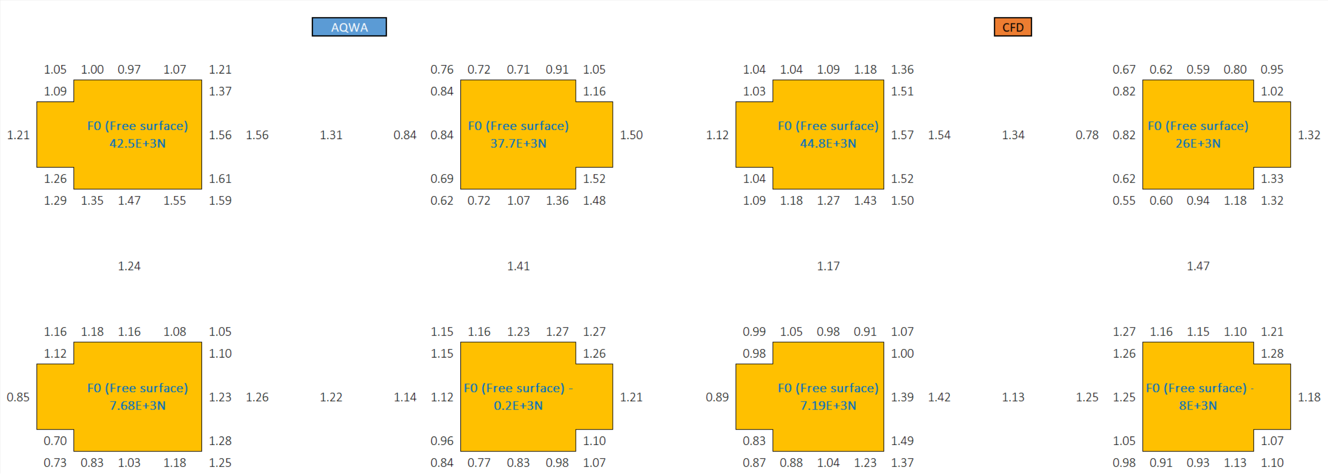

Around the columns the greater difference is 17% at maximum, however, this represents considerable differences in the free surface force elevation parcel column 1 and 4, but which do not interfere much in the whole picture.

Figure 5.44: Wave elevation amplitude and force parcel from FVM in relation to BEM with T = 10 s and 157.5^o heading.

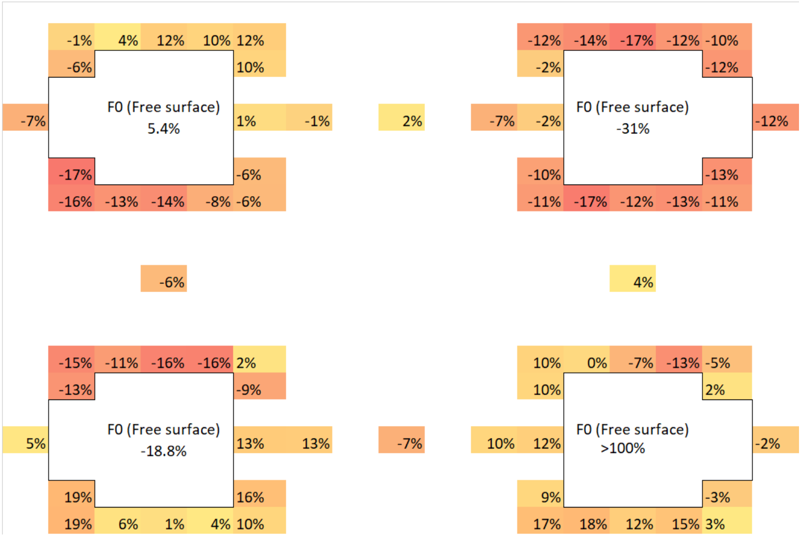

One more time, as it is presented on Tab. 5.2, the difference between AQWA, CFD and experiments are in agreement with the wave elevation contribution to the mean drift forces.

Table 5.2: Force elevation parcel and total mean drift force for the regular waves at 157.5^o.

ID	T (s)	AQWA	CFD	Difference (kN)
Force Elevation Parcel (kN)	10.0	88	70	-18
Total Mean Drift (kN)	10.0	105	88	-17

Regarding the 157.5^o heading results, no large differences in the centers between the columns are found. This leads again to a thinking that for the 180^o heading case may was indeed a near-trapped wave mode for this period, since the wave height and steepness are the same and the only thing that changed is the apparent distance between the columns.

At this point, it is worth it to evaluate the likelihood of a trapped mode excitation according to Aranha and Pesce (1988). In their work, the authors have provided the results for a bi-dimensional body with a beam (B)/height (D) = 2. The analyses were performed for a bidimensional submerged body with infinite length, in which transverse waves were acting on. The (λ_o/k_o) parameter controls the likelihood of a trapped mode being excited, but it is not a probability measurement. As it is shown in Fig. 5.45, the (λ_o/k_o) parameter for a rectangle, depends on the body vertical distance from the free surface (S), besides its main dimensions and the wave number of the incoming wave (k_o). Using the main dimensions of the semi-submersible of this thesis (Tab. 4.1), the relation B/D results in 1.46, but Fig. 5.45 values will be used as a quantitative analysis. The outcomes for the semi-submersible in question are represented by the red dashed lines in Fig. 5.45. It is possible to notice that the (λ_o/k_o) parameter, for the correspondent S/D, is maximum exactly for the wave period region around 10 s. Therefore, this analysis indicates that for this wave period range, it is possible the occurrence of trapped wave mode related to the pontoons.

Figure 5.45: Likelihood of a trapped mode excitation for a rectangle.

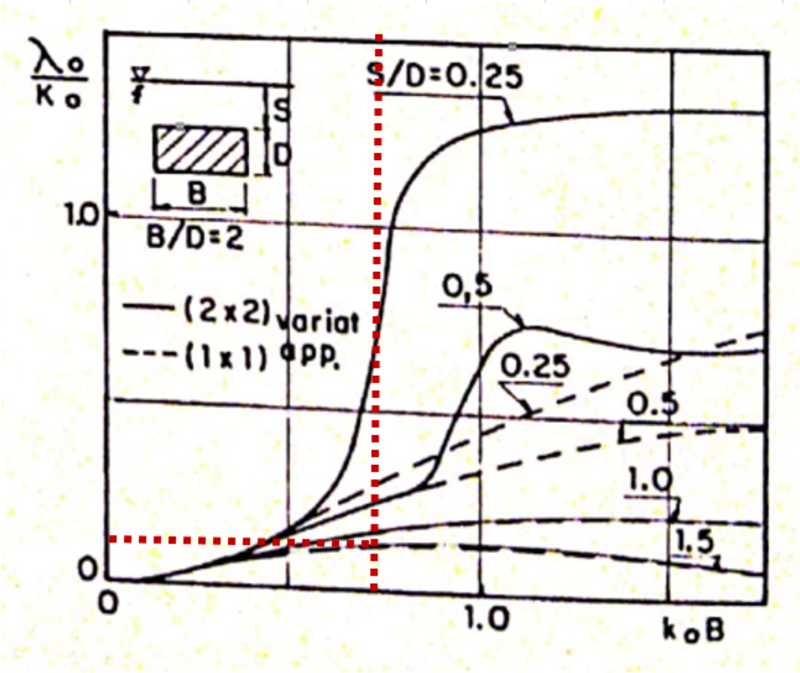

Adapted from Aranha and Pesce (1988).

5.4 Free floating tests in irregular waves with catenary mooring lines

Before presenting the results regarding this section, it is fundamental to inform that surge, heave, pitch RAOs; and surge mean and slow-drift for REG04, REG05, BIC04 and BIC05 were also experimentally investigated with the catenary lines and the motions results were in ±3% agreement with those from the horizontal system.

In order to understand whether the deviations observed in the ideal cases of regular and bichromatic waves would affect the predictions for real sea states with a catenary mooring system, some irregular sea states, described in Tab. 4.8, were evaluated in the model basin and compared to the BEM code. For these cases, the wave drift damping was and was not accounted for in the analysis, as Fig. 5.46 presents. The external damping was imposed by Morison's elements into AQWA just as it was done for the bichromatic waves.

A parallel investigation regarding the second-order approximation model was performed by computing the surge standard deviation with the full QTF computation and with Newman's approximation, see Fig. 5.46. As expected and as demonstrated by Fig. 4.19, Newman's approximation has recovered the complete results very well, no significant deviation was found at all the periods and wave heights evaluated.

Figure 5.46: Slow-drift standard deviation in irregular waves at 180^o heading comparisons between experimental tests and BEM code with wave drift damping and without wave drift damping.

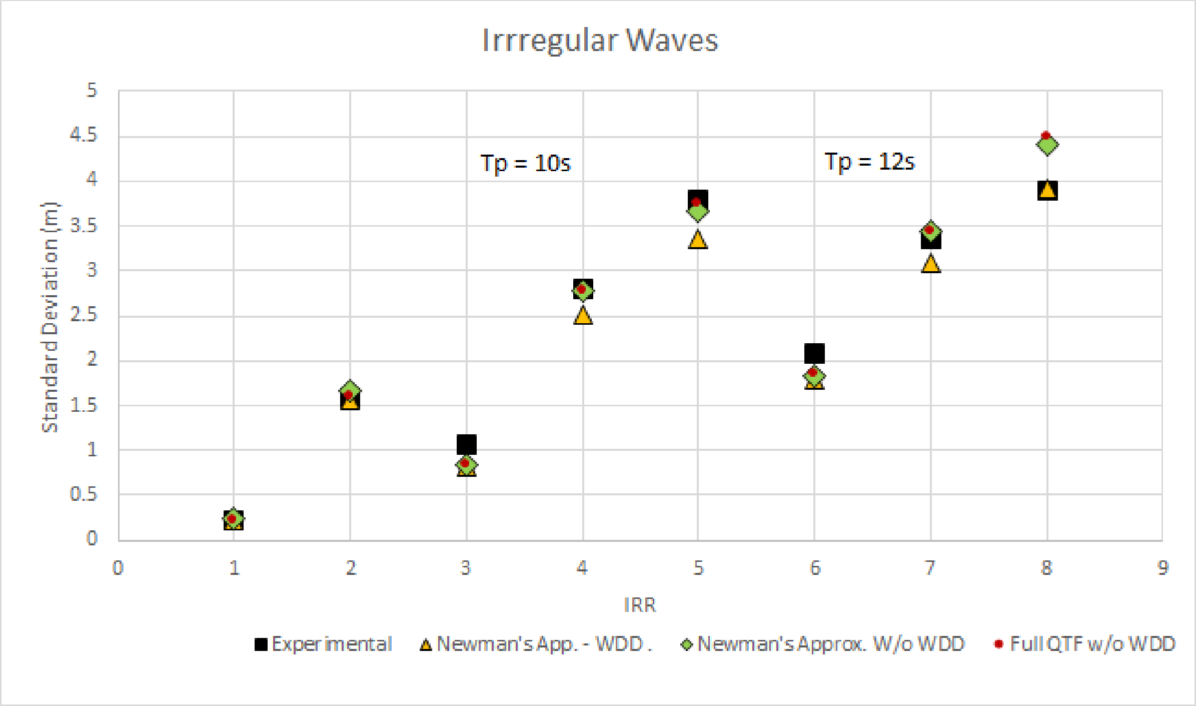

For real sea state, it is possible to notice that the BEM code was able to recover the slow-drift amplitudes relatively well, irrespective of the peak period. In particular, no evidence of larger errors is observed when for the peak period of 10 s, if compared to the other cases. Therefore, these results indicate that the pronounced differences observed in steady-state wave conditions are significantly attenuated in irregular waves, even for very high sea states such as IRR05 and IRR08 with Hs = 5.4 m and Hs = 7.8 m respectively. In addition, the wave drift damping is being captured as positive in all cases and it is not causing any considerable difference in the results. Probably, the more acute differences occur in the regular tests because they provide sufficient time for the phenomenon to evolve and reach its maximum intensity, something that does not occur in the irregular wave tests. At least, this is an important observation that should be kept in mind when analyzing regular wave tests that are frequently made as part of the dynamic characterization of the floating unit.

6 Conclusions

Given the observed aspects, obtaining good results of low-frequency forces and slow-drift motions of non-ship shaped platforms is challenging. Essentially, all types of offshore floating systems, which are moored in the ocean, may witness the presence of second-order wave forces, and the study of motions related to these forces is relatively recent in the hydrodynamic field. On account of that, the present work has demonstrated that the procedure of estimating them is not yet fully consolidated yet and there are still a variety of obstacles to overcome. For offshore industries, not defining slow-drift motions correctly can mean financial loss and other injuries.

Many authors such as Berthelsen et al. (2009), Lopez-Pavon et al. (2015), Wang et al. (2021) and Wang et al. (2022) have noticed that potential codes may not reproduce well the experiments in some cases. In general, these authors have focused on severe and extreme wave conditions, in which the viscous forces are more present. Usually, these viscous forces are considered responsible for the potential codes underestimating the forces and slow-drift motions of platforms in some heavy sea state conditions. Indeed, in conditions where the steepness is significantly large, the viscous effects become an important factor/variable in the estimation of the second-order loads. Nevertheless, it is also shown in this work that, even for mild sea states Hs = 2 m, remarkable divergences in the slow-drift motions between potential codes and model tests can be found.

In this thesis, a four-column large displacement semi-submersible platform was used as an object of study. Wave tests, in which the model-scaled was fixed to the bridge, moored with soft lines, and further with catenary lines, were performed in order to measure platform motions in a variety of regular, bichromatic, and irregular waves. The first two types of waves were fundamental to help substantiate the problem, as their steady-state is easily achieved, and also because they offer the possibility of isolating the natural frequency. However, irregular sea states are really what matters for practical and real-life industrial/offshore problems.

As part of the characterization of the problem, the well-known bottom-mounted fixed circular cylinder, which has an analytical solution provided by MacCamy and Fuchs (1954) for the first-order forces and by Kim and Yue (1989) for the mean drift forces, was evaluated for the same 5 regular waves, with Tp ranging from 7 to 11 s. The results show that, regardless of the period, the contribution of the quadratic pressure to the mean drift loads is almost null at the pontoon's depth, meaning the horizontal drift loads for this type of hull are essentially dominated by the pressure variation on the vertical columns.

The main potential code used to perform the analysis was AQWA, but all results were cross-checked with WAMIT to ensure that the results were indeed representative of panel methods. With these radiation/diffraction tools, all the experimental tests were carefully reproduced, verified, and analyzed for the semi-submersible platform. Some large divergences in the mean drift forces, mean drift and slow-drift motions were found for the period of T = 10 s for the regular waves and T = 10 s and T = 10.51 s for bichromatic waves. A systematical and very detailed analysis and revision of the potential code was performed for all the performed cases and nothing unusual was found.

Aiming to shed light on the source of these strange differences that seemed to occur only in a narrow frequency range, further analysis was made, now using ANSYS Fluent. Due to the complexity of developing a CFD analysis, only the experiments with regular waves with the platform fixed were reproduced in Fluent, which provided five simulations cases in total. Again, the simulations were carefully developed, verified, and validated with the first-order model tests and mean drift forces in surge, besides the comparison of wave elevation with the four wave probes next to the inner columns.

The advantage of having validated CFD simulations is that one can obtain parameters that are not possible to be measured in experiments, such as the elevation of waves in a large number of points, and also the possibility of splitting forces into viscous and pressure parcels. For the five simulations performed in this work, 16 wave probes were placed around each column, in addition to the 4 probes between the center of the columns and the 4 probes of the experiments. The idea was to use these probes to compare the collected data to the values provided by AQWA and to enable an “external” computation of the mean drift force that depends on the integration of the wave elevations around the columns.

The first observation regarding the wave elevation share in each column is that they vary considerably depending on the wave period. Both the magnitudes and the signal undergo massive changes from one period to another. In addition, the only case where AQWA and CFD show small differences is that of T = 11 s, which presents the lowest slope condition. The wave elevations in this case were recovered by AQWA almost perfectly. Although the cases with T = 7, 8, 9, 10 s have presented some differences in the wave elevation, only for the case with T = 10 s the portion of the force that depends on elevation showed large deviations, which are in accordance with the values found for the mean drift forces. In other cases, variations in wave elevation values from one region to another practically compensated for the final forces values. Another very interesting point for the T = 10 s case is that this is the only case where large differences between AQWA and Fluent are also found in the wave elevation between the columns located along the wave direction.

This deviation in the wave field leads to the supposition that a near-trapping wave may be occurring at this period. By studying the case with the same wave height and period, but with a different heading is also an evidence of a possible near-trapped wave, since by only changing the apparent distance between the columns, the difference between the BEM code and the experiments and CFD reduces significantly.

Regarding how these force results interfere in the mean and slow-drift motions for bichromatic waves, the comparison with AQWA was performed and similarities were found. For the surge mean-drift the comparison is more direct as the result is not affected by uncertainties in the viscous damping predictions. However, for the slow-drift motions, the same pattern appears and the T = 10 s case is once again underestimated by the potential code.

What this study reveals is that there is indeed a difficulty of potential codes in predicting mean and slow-drift motions for the semi-submersible studied in a determined range of periods even at mild sea states which are within software limitations in regular and bichromatic waves. The problem was surrounded with a fundamental approach through the direct measurement of forces acting on the fixed model and the direct measurement of the mean and slow-drift motions acting on the free floating model. Having in hand FVM simulations, it was concluded that the source of the errors are in the wave field estimation by the BEM codes, which compromise the mean drift prediction for T = 10 s. In turn, these errors in the force values are dissipated/obstructed in the tests involving a more realistic sea energy distribution in the wave frequencies (irregular wave tests), probably due to the insufficient wave energy/time to excite the phenomena and allow it to reach its steady-state. Therefore, for real seas, BEM codes are predicting the mean and slow-drift amplitudes well for all the periods studied in the presented case.

6.1 Future Works

This work has isolated an issue on the potential codes on estimating slow-drift motions. This way there is a range of possibilities to study the source of divergence even further.

- To analyse the experimental tests at sway forces and motions as well;
- CFD simulations based on FVM are highly time-consuming in general, but the cases studied made the power demand even higher due to the large mesh size besides having

a regular wave as input. Then, in future, more CFD simulations could be performed in order to compare the results from 157.5^o and 135^o headings both in surge and sway motions;

- To perform a detailed numerical and experimental uncertainty analysis;
- To use the FVM tool to investigate the results in a systematic way with waves of second-order Stokes and with different wave steepness.
- To perform captive experiments with periods between 9 and 10 s in order to capture the highest mean drift force peak in surge and correlate the respective wavelength to the distance between the columns;
- To use this wavelength to find another heading and period which match the same configuration in order to try to achieve another near-trapped mode. Possibly, the divergence between the BEM and experimental are going to be less pronounced because the number of columns involved is going to be less;
- To use different semi-submersible platforms, sizes and shapes, and repeat the procedures trying to correlate the same wavelength, distance between columns and near-trapped modes;
- To investigate why the wave elevations outboard the blister are not well captured by BEM codes.

References

AIRY, G. B. *Tides and waves.* B. Fellowes, 1845.

ANSYS, A. Aqwa theory manual. *AQWA: Canonsburg, PA, USA*, 2013.

ARANHA, J. A formula for 'wave damping'in the drift of a floating body. *Journal of Fluid Mechanics*, Cambridge University Press, v. 275, p. 147–155, 1994.

ARANHA, J.; FERNANDES, A. On the second-order slow drift force spectrum. *Applied Ocean Research*, Elsevier, v. 17, n. 5, p. 311–313, 1995.

ARANHA, J. A. P.; PESCE, C. Effect of the second-order potential in the slow-drift oscillation of a floating structure in irregular waves. *Journal of ship research*, SNAME, v. 30, n. 02, p. 103–122, 1986.

ARANHA, J. A. P.; PESCE, C. P. Slow drift and trapping of waves on submerged bodies. In: SPRINGER. *Nonlinear Water Waves: IUTAM Symposium, Tokyo/Japan, August 25–28, 1987.*, 1988. p. 275–282.

BERTHELSEN, P. A.; BAARHOLM, R.; KOZDI, C. P.; STANSBERG, C. T.; HASSAN, A.; DOWNIE, M.; INCECIK, A. Viscous drift forces and responses on a semisubmersible platform in high waves. In: *International Conference on Offshore Mechanics and Arctic Engineering*, 2009. v. 43413, p. 469–478.

BUĆAN, B.; BUČA, M. P.; RUŽIĆ, S. Numerical modelling of the flow around the tanker hull at model scale. *Brodogradnja: Teorija i praksa brodogradnje i pomorske tehnike*, Fakultet strojarstva i brodogradnje, v. 59, n. 2, p. 117–122, 2008.

CALLAN, M.; LINTON, C.; EVANS, D. Trapped modes in two-dimensional waveguides. *Journal of Fluid Mechanics*, Cambridge University Press, v. 229, p. 51–64, 1991.

CARMO, L. H. S. d. *A slender-body approach for computing second-order wave forces in seakeeping simulations of floating offshore wind turbines.* Thesis (PhD) — Universidade de São Paulo, 2021.

CCM+, S. User manual for star ccm+. Sabalcore Florida, USA, 2018.

CLAUSS, G.; LEHMANN, E.; ÖSTERGAARD, C. *Offshore structures: volume I: conceptual design and hydromechanics.* Springer, 2014.

DEEP TREKKER. *The Many Models of Offshore Platforms.* Disponível em: <https://www.deeptrekker.com/resources/oil-energy-platforms>. Acessed in: 10

july. 2020. 2020.

EGAB, L. Computer-aided engineering findings on the physics of tire/road noise. In: *Automotive Tire Noise and Vibrations*. Elsevier, 2020. p. 217–243.

EVANS, D.; PORTER, R. Near-trapping of waves by circular arrays of vertical cylinders. *Applied Ocean Research*, Elsevier, v. 19, n. 2, p. 83–99, 1997.

FLUENT, A. ver. 13: theory guide. *Ansys Inc., USA*, 2011.

GOODFELLOW, H. D.; WANG, Y. *Industrial ventilation design guidebook: volume 2: engineering design and applications*. Academic press, 2021.

HANAOKA, T. On the reverse flow theorem concerning wave making theory. In: *Proceedings of the 9th Japan National Congress for Applied Mechanics, Paper III-9*, 1959.

HASKIND, M.; NEWMAN, J. *The exciting forces and wetting of ships in waves.*, 1962.

HAUTECLOCQUE, G. de; REZENDE, F.; WAALS, O.; CHEN, X.-B. Review of approximations to evaluate second-order low-frequency load. In: AMERICAN SOCIETY OF MECHANICAL ENGINEERS. *International Conference on Offshore Mechanics and Arctic Engineering.*, 2012. v. 44885, p. 363–371.

KAMATH, A.; BIHS, H.; CHELLA, M. A.; ARNTSEN, Ø. A. Cfd simulations to determine wave forces on a row of cylinders. *Procedia Engineering*, Elsevier, v. 116, p. 623–630, 2015.

KATOPODES, N. D. *Free-surface flow: computational methods*. Butterworth-Heinemann, 2018.

KEULEGAN, G. H.; CARPENTER, L. H. Forces on cylinders and plates in an oscillating fluid. *Journal of research of the National Bureau of Standards*, Department of Commerce, National Bureau of Standards, v. 60, n. 5, p. 423–440, 1958.

KHALILI, N. et al. *Computational Mechanics-New Frontiers for the New Millennium*. Elsevier, 2012.

KIM, M.-H.; YUE, D. K. The complete second-order diffraction solution for an axisymmetric body part 1. monochromatic incident waves. *Journal of Fluid Mechanics*, Cambridge University Press, v. 200, p. 235–264, 1989.

KIM, M.-H.; YUE, D. K. The complete second-order diffraction solution for an axisymmetric body part 2. bichromatic incident waves and body motions. *Journal of Fluid Mechanics*, Cambridge University Press, v. 211, p. 557–593, 1990.

LÁVIČKA, D.; MATAS, R. Computation of drag and lift coefficients for simple two-dimensional objects with reynolds number re= 420 000. In: EDP SCIENCES. *EPJ Web of Conferences.*, 2012. v. 25, p. 01047.

LEE, C. Theory manual. Citeseer, 1995.

LEE, C.-H.; NEWMAN, J. Computation of wave effects using the panel method. *WIT Transactions on State-of-the-art in Science and Engineering*, WIT Press, v. 18, 2005.

LEFFLER, W. L.; PATTAROZZI, R.; STERLING, G. *Deepwater petroleum exploration & production: a nontechnical guide.* PennWell Books, 2011.

LINTON, C.; EVANS, D. The interaction of waves with arrays of vertical circular cylinders. *Journal of fluid mechanics*, Cambridge University Press, v. 215, p. 549–569, 1990.

LIRA, W. M.; CAVALCANTI, P. R.; COELHO, L. C.; MARTHA, L. F. A modeling methodology for finite element mesh generation of multi-region models with parametric surfaces. *Computers & Graphics*, Elsevier, v. 26, n. 6, p. 907–918, 2002.

LOPEZ-PAVON, C.; WATAI, R. A.; RUGGERI, F.; SIMOS, A. N.; SOUTO-IGLESIAS, A. Influence of wave induced second-order forces in semisubmersible fowt mooring design. *Journal of Offshore Mechanics and Arctic Engineering*, American Society of Mechanical Engineers Digital Collection, v. 137, n. 3, 2015.

MACCAMY, R.; FUCHS, R. A. *Wave forces on piles: a diffraction theory.* US Beach Erosion Board, 1954.

MANIAR, H.; NEWMAN, J. Wave diffraction by a long array of cylinders. *Journal of fluid mechanics*, Cambridge University Press, v. 339, p. 309–330, 1997.

MANUAL, U. Ansys fluent 12.0. *Theory Guide*, 2009.

MATOS, V. L. F. *Movimentos Ressonantes Lentos no Plano Vertical em Plataformas Semi-Submersíveis.* Thesis (PhD) — Universidade Federal do Rio de Janeiro, 2009.

MATSUMOTO, F. T.; WATAI, R. A.; SIMOS, A. N.; FERREIRA, M. D. Wave run-up and air gap prediction for a large-volume semi-submersible platform. *Journal of offshore mechanics and Arctic engineering*, American Society of Mechanical Engineers Digital Collection, v. 135, n. 1, 2013.

MENTER, F. Zonal two equation kw turbulence models for aerodynamic flows. In: *23rd fluid dynamics, plasmadynamics, and lasers conference*, 1993. p. 2906.

MORISON, J.; JOHNSON, J.; SCHAAF, S. et al. The force exerted by surface waves on piles. *Journal of Petroleum Technology*, Society of Petroleum Engineers, v. 2, n. 05, p. 149–154, 1950.

NEWMAN, J. Second-order, slowly-varying forces on vessels in irregular waves. 1974.

NEWMAN, J. N. The exciting forces on fixed bodies in waves. *Journal of Ship Research*, SNAME, v. 6, n. 04, p. 10–17, 1962.

NEWMAN, J. N. Wave-drift damping of floating bodies. *Journal of Fluid Mechanics*, Cambridge University Press, v. 249, p. 241–259, 1993.

NISHIMOTO, K.; FUCATU, C. H.; MASETTI, I. Q. Dynasim—a time domain simulator of anchored fpso. *J. Offshore Mech. Arct. Eng.*, v. 124, n. 4, p. 203–211, 2002.

NOSSEN, J.; GRUE, J.; PALM, E. Wave forces on three-dimensional floating bodies with small forward speed. *Journal of Fluid Mechanics*, Cambridge University Press, v. 227, p. 135–160, 1991.

PESCE, C. P.; AMARAL, G. A.; FRANZINI, G. R. Mooring system stiffness: A general analytical formulation with an application to floating offshore wind turbines. In: AMERICAN SOCIETY OF MECHANICAL ENGINEERS. *International Conference on Offshore Mechanics and Arctic Engineering.*, 2018. v. 51975, p. V001T01A021.

PINKSTER, J. A. Low frequency second order wave exciting forces on floating structures. 1980.

RAPP, B. E. *Microfluidics: modeling, mechanics and mathematics.* Elsevier, 2022.

RODI, W.; FUEYO, N. *Engineering turbulence modelling and experiments 5.* Elsevier, 2002.

RUG. *ComFLOW.* Urlhttps://www.math.rug.nl/ veldman/comflow/comflow.html. may 2023.

RUNCHAL, A. K. Brian spalding: Cfd and reality–a personal recollection. *International Journal of Heat and Mass Transfer*, Elsevier, v. 52, n. 17-18, p. 4063–4073, 2009.

STOKES, G. *On the Theory of Oscillatory Waves. Transaction of the Cambridge Society 8. 441-455. Reprinted in Stokes, GG (1880). Mathematical and Physical Papers.* Cambridge University Press. 1847.

SUN, S.; ZHANG, T. *Reservoir simulations: Machine learning and modeling.* Gulf Professional Publishing, 2020.

VADHOLM, J. *Numerical Study on Wave Drift Loading on Slender Marine Structures.* Thesis (Master's) — NTNU, 2017.

WAMIT, I. Wamit user manual. *Chestnut Hill, USA*, 2006.

WANG, L.; ROBERTSON, A.; JONKMAN, J.; YU, Y.-H.; KOOP, A.; NADAL, A. B.; LI, H.; BACHYNSKI-POLIĆ, E.; PINGUET, R.; SHI, W. et al. Oc6 phase ib: Validation of the cfd predictions of difference-frequency wave excitation on a fowt semisubmersible. *Ocean Engineering*, Elsevier, v. 241, p. 110026, 2021.

WANG, L.; ROBERTSON, A.; JONKMAN, J.; YU, Y.-H. Oc6 phase i: Improvements to the openfast predictions of nonlinear, low-frequency responses of a floating offshore wind turbine platform. *Renewable Energy*, Elsevier, v. 187, p. 282–301, 2022.

WILCOX, D. C. et al. *Turbulence modeling for CFD.* DCW industries La Canada, CA, 1998.

YANG, L.; NESTEGÅRD, A.; FALKENBERG, E. Analysis of semi-submersible under combined high waves and current conditions compared with model tests. In: AMERICAN SOCIETY OF MECHANICAL ENGINEERS DIGITAL COLLECTION. *ASME 2018 37th International Conference on Ocean, Offshore and Arctic Engineering.*, 2018.

ZHANG, L.; SHI, W.; KARIMIRAD, M.; MICHAILIDES, C.; JIANG, Z. Second-order hydrodynamic effects on the response of three semisubmersible floating offshore wind turbines. *Ocean Engineering*, Elsevier, v. 207, p. 107371, 2020.

A Pre-tests

The pre-tests are performed in order to ensure that the ballasted model and mooring system have been correctly settled up. The main parameters which need to be verified are the vertical center of gravity (KG), metacentric height (GM) and all the natural periods of the model. Besides the model specification, the surge and sway stiffness of the mooring system also need to be checked up.

Although all of the pre-test have been performed only at 180^o, the semi-submersible model was tested at three wave headings. At the other headings, 157.5^o and 135^o, just the decay tests have been executed, since the repositioning of the mooring lines could change the global stiffness of the system by inaccuracies of human factor while changing the heading. Next, details about the pre-tests with the catenary mooring will be exemplified, but the same was done for the horizontal mooring.

A.1 Pull-out

Motivated by measuring the stiffness of the mooring system, pull-out tests were executed in surge and sway degrees of freedom.

The first step was to build a pulley arrangement where a load at the normal direction (aft to bow) of the model could be applied. For each weight, the model displacement was measured by the Qualisys and the force (Fe) was measured by a load cell, which was aligned to the pulley cable attached to the model. Figure A.1 illustrates the force application and the displacement caused by it.

Figure A.1: Schematic model of the pull-out test.

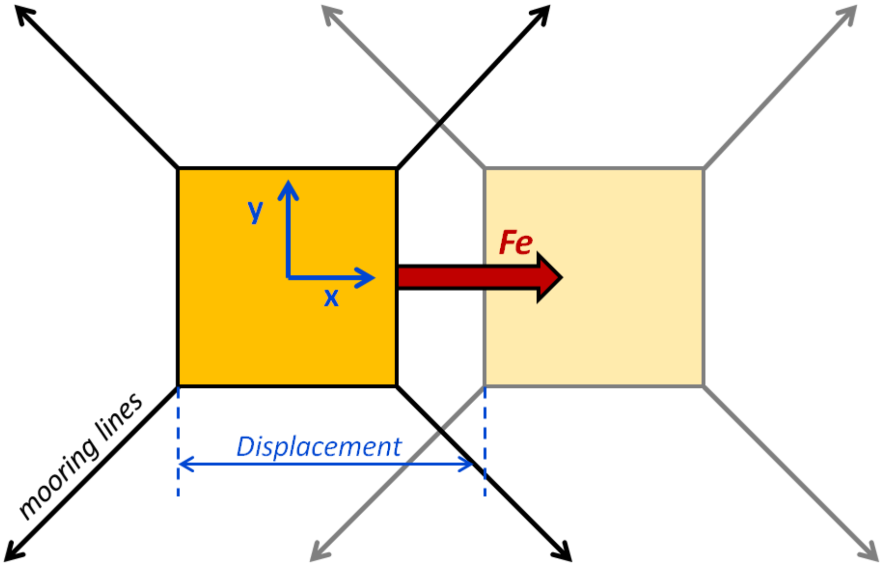

In total, 8 weights were loaded and offloaded twice at both degrees of freedom. Figure A.2 demonstrates the pull-out results full-scaled for surge. All the loading and offloading cases showed a good agreement. Basically, the stiffness of the system is given by the angular coefficient of the line that better fits the points. In this case, a mean between the lines of each loading and offloading case was computed. The results in Tab. A.1 demonstrate that the experimental set up is very similar to those which were numerically designed.

Figure A.2: Pull-out full-scaled results for surge.

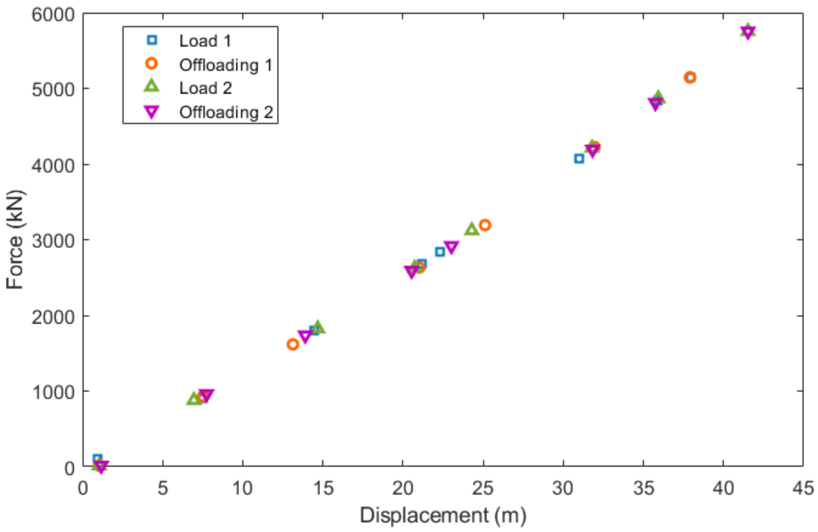

Table A.1: Mooring system stiffness comparison at full-scale.

Degree of freedom	Theoretical	Experimental
Surge	132.62	126.90
Sway	132.52	126.75

A.2 Static inclination

Static inclination tests provide the transverse and longitudinal metacentric heights of the model on water. The test procedure is essentially placing different weights on different places of the deck, bow and stern, starboard and portside, in order to create moments arms. Hence, the roll and pitch inclinations can be measured thanks to the Qualysis system. This test was being performed while the model was without any restriction feature and repeated when the model was moored, thusly, the lines interference could be evaluated.

Based on the weights, distances and inclinations, the restoring moment arm (GZ) is calculated by the sum of the moments, as well as the GM. For each degree of freedom, the GZ and GM curves were computed through four inclinations angles and which have provided an inclination of 7^o at maximum for each board. The results have showed linear static stability curves which were already expected, since the hull does not present large variations on the waterline area.

Table A.2 resumes the results obtained on the roll tests. The buoyancy height (KB) and the metacentric radius (BM) are obtained from the hulls geometry. Lastly, the KG is simply calculate by: KG = KM+KB-GM. The mooring system provides a modification on the GM value, and for consequence, on the KG value. Since the wave tests have been performed while the system was moored, in order to account to the moment induced by the mooring system, the KG value assumed was 25.29 meters, which is very close to the theoretical one.

Table A.2: Transverse static inclination tests main result on real scale.

	Theoretical	Model without mooring	Moored model
GM (m)	5.01	4.72	5.04
KG (m)	24.90	25.60	25.29
KB (m)	9.78	9.74	9.45
$\text{BM}_x(m)$	20.54	20.54	20.54

A.3 Decay

The decay tests have as objective to determine the natural periods of all degrees of freedom. Essentially, the test aims to manually impose an amplitude at each degree of freedom and capturing its motion up to the model stops. For the vertical motions, the test was executed three times each with the system free and moored, so the lines interference could be inferred. In the case of surge, sway and yaw only one test each was performed. The tests were repeated at each heading with the system moored for all degrees of freedom. Fig. A.3 exemplifies the decay tests for surge at the 157.5^o heading. On the envelope, ζ represents the damping if it was only linear along the all test. Fig. A.4 takes the maximum and minimum values of the cycles of Fig. A.3 for estimating the linear (ζ) and quadratic $B_2/(M + A)$ damping coefficients. These coefficients do not remain the same during all the test, providing that for larges amplitudes the quadratic coefficient tends to be higher than for the smaller ones. Figure A.4 provides the damping variation percentage in relation to the amplitude. For this thesis, the yellow line (all points) was used.

Figure A.3: Decay test for surge motion at 157.5^o heading.

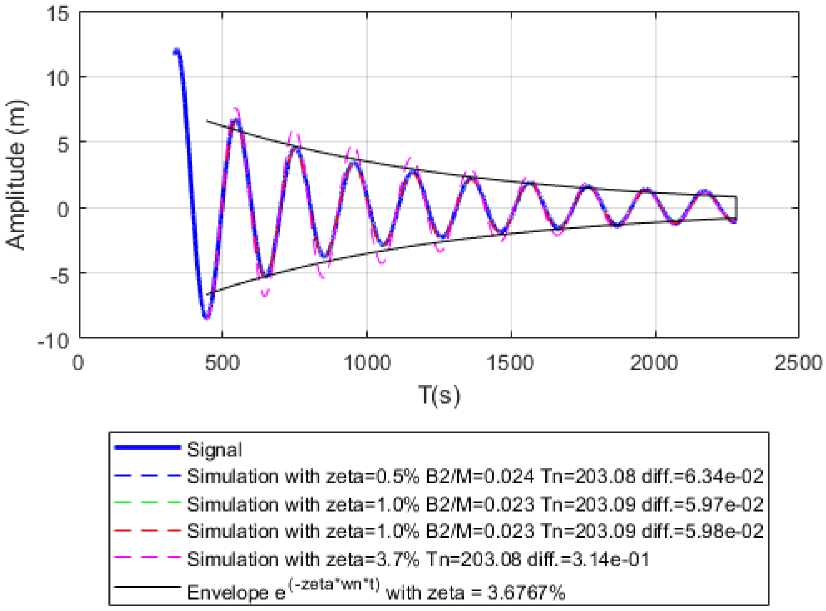

Figure A.4: Linear and quadratic damping variation for surge motion at 157.5^o heading.

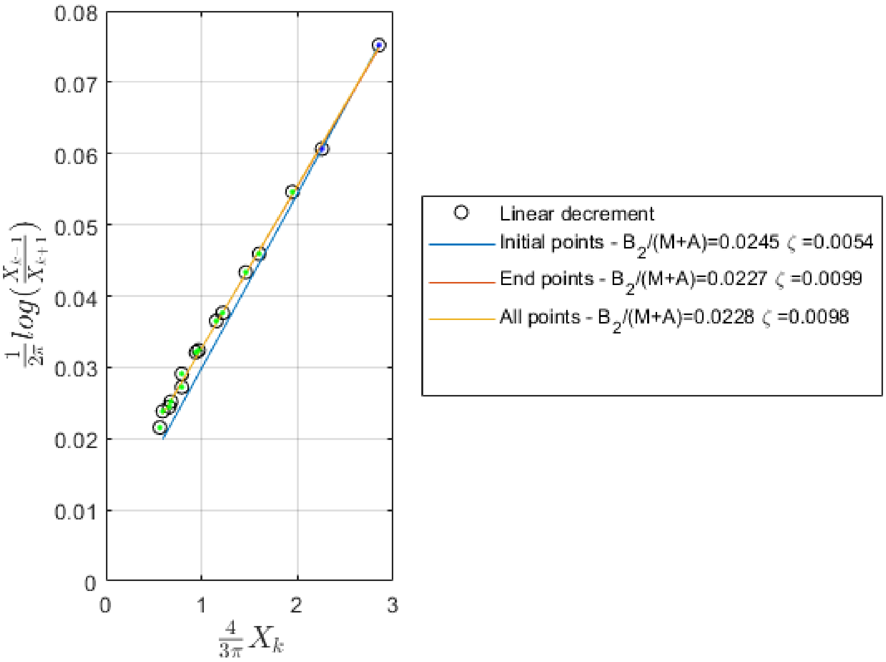

The main results are presented in Tab. A.3, A.4, A.5 and A.6. For heave, roll and pitch, the values introduced are the average of the three tests. As expected, the restriction imposed on the model interferes on the natural periods of roll and pitch motions. Also, it is important to notice that the natural periods have not changed considerably between one heading and other.

Table A.3: Decay tests results of the system without mooring.

	Envelope	
Degree of freedom	Tn (s)	b$_{exp}$(%)
Heave	23.41	1.28
Roll	40.57	1.63
Pitch	36.61	1.40

Table A.4: Decay tests results of the moored model at 180^o heading.

	Envelope	
Degree of freedom	Tn (s)	$b_{exp}(\%)$
Surge	205.56	2.6
Sway	224.75	2.87
Heave	23.31	1.32
Roll	37.8	1.85
Pitch	35.23	1.45

Table A.5: Decay tests results of the moored model at 157.5^o heading.

	Envelope	
Degree of freedom	Tn (s)	$b_{exp}(\%)$
Surge	203.8	3.68
Sway	218.43	3.03
Heave	23.32	1.46
Roll	37.75	1.59
Pitch	35.23	1.42
Yaw	121.28	2.287

Table A.6: Decay tests results of the moored model at 135^o heading.

	Envelope	
Degree of freedom	Tn (s)	$b_{exp}(\%)$
Surge	205.56	2.6
Sway	224.75	2.87
Heave	23.31	1.32
Roll	37.83	1.84
Pitch	35.23	1.45
Yaw	121.33	2.33